Montanuniversität Leoben

Dissertation

FATIGUE CRACK GROWTH OF NANOCRYSTALLINE AND ULTRAFINE-GRAINED METALS PROCESSED BY SEVERE PLASTIC DEFORMATION

Thomas Leitner

Leoben, January 2017

Erich Schmid Institute of Materials Science
Montanuniversität Leoben
Department Materials Physics
Jahnstrasse 12
8700 Leoben, Austria

Affidavit

I declare in lieu and oath, that I wrote this thesis and performed the associated research myself, using only literature cited in this volume.

Leoben, 10.01.2017

Danksagung

Vorweg möchte ich mich bei Prof. Reinhard Pippan für die ausgezeichnete Unterstützung bei der Erstellung meiner Dissertation bedanken. Reinhard nahm sich immer die Zeit, um mit mir über Unklarheiten und Probleme zu diskutieren und lieferte viele wertvolle Ideen. Außerdem möchte ich mich bei Reinhard dafür bedanken, dass ich die Möglichkeit hatte, auf zahlreichen internationalen Konferenzen neue Erfahrungen zu sammeln. Und nicht zuletzt, vielen Dank für deine Rolle als Schiführer am Arlberg – die Firnabfahrten werden mir immer in bester Erinnerung bleiben.

Großer Dank gebührt auch Dr. Anton Hohenwarter, der maßgeblich für das Gelingen der Arbeit verantwortlich ist. Toni stand mir bei den vielen Problemchen des Dissertanten Alltags immer als hilfsbereiter Kollege und vor allem auch als guter Freund zur Seite. Durch deine Hilfestellungen und die gemeinsamen Diskussionen konnte ich viel über Bruchmechanik lernen und neue Zusammenhänge erkennen (besonders bei erweiterten „Mitarbeiter Gesprächen“).

Bedanken möchte ich mich außerdem bei meinen Bürokollegen, die mich fachlich, aber vor allem auch moralisch immer unterstützt haben. Danke Karo, Peter, Zhou, Michael, Manuel und Stephan - es war immer eine lustige Zeit mit euch, egal ob im Büro oder zur späteren Stunde auf der Tanzfläche.

Weiters waren Franz und Robin in der Werkstatt, Silke in der Metallografie, sowie meine studentischen Mitarbeiter Riccarda, Clemens und Simon bei der Herstellung meiner Proben eine große Hilfe. Bei administrativen Angelegenheiten wurde ich stets von Sabine und Dani unterstützt – vielen Dank für euer Verständnis bei Problemen aller Art. Auch dem restlichen ESI Team gilt ein herzliches Dankeschön für die gute Zusammenarbeit und die vielen netten Stunden die wir gemeinsam verbringen konnten.

Abseits der Arbeit möchte ich mich bei allen meinen Freunden bedanken, die mich in meiner Freizeit am Berg, in der Luft und bei vielen anderen Aktivitäten begleitet haben.

Ganz besonders danke ich meinen Eltern, sowie meiner restlichen Familie, die es mir ermöglicht haben, diese Ausbildung zu absolvieren. Vielen Dank, dass ihr immer hinter mir steht und mich bei allen meinen Plänen unterstützt.

Zu guter Letzt möchte ich mich bei meiner Frau, Katharina, bedanken, die mir in der Zeit meiner Dissertation eine große Stütze war. Mit dir konnte ich über alle meine Bedenken reden, aber mich auch gemeinsam mit dir über Erfolge freuen. Unsere vielen schönen gemeinsamen Erlebnisse haben mir immer wieder neue Energie gegeben und machen diese Zeit unvergesslich.

Abstract

Ultrafine-grained (UFG) and nanocrystalline (NC) metals exhibit extraordinary mechanical properties, such as extraordinary high yield strengths and increased fatigue limits. However, in order to safely use these materials for engineering applications, the investigation of their fracture behavior under quasi-static and cyclic loading is essential. The present thesis focuses on the fatigue crack growth behavior of UFG and NC metals fabricated by severe plastic deformation (SPD) techniques. The aim of this work is to study the influence of SPD processing and the resulting grain refinement on crack propagation processes.

For the present thesis a broad variety of materials, ranging from pure metals (iron and nickel) to complex industrially used alloys (austenitic steel, pearlitic steel and a shape memory alloy), were deformed by high pressure torsion and equal channel angular pressing to obtain UFG and NC microstructures. Fatigue crack growth experiments were performed on samples of these metals in their undeformed and SPD processed state. Different specimen orientations in respect to the deformation process were tested for the investigation of the fatigue crack growth anisotropy. Additionally, extensive fracture surface analyses were carried out to get further information about the mechanisms of fatigue crack propagation.

It will be shown, that the deteriorated fatigue crack growth behavior of UFG and NC materials, which is often reported in literature, can be attributed to a reduction of crack closure contributions. Intergranular fracture, which is typical for the failure of SPD metals under cyclic loads, is found to have a lower crack growth resistance, compared to a transgranular crack growth. However, at high mean stresses, where crack closure contributions only play a minor role, grain refinement can increase the intrinsic fatigue crack growth resistance. This improvement is a result of the increased strength of the material, but is only observed when the fracture mode is not changed. Dislocation patterns on the fracture surfaces, as well as estimations of the fatigue crack growth rate from deformation based models indicate that fatigue crack propagation is governed by a blunting and re-sharpening process along the grain boundaries in the investigated UFG and NC materials. Furthermore, it will be proven that the anisotropic fatigue crack growth behavior of the SPD processed metals originates from the elongated grains of SPD processed metals. This effect can be positively exploited by using the material in an orientation, with the longer axis of the grains perpendicular to expected crack growth directions, as this results in an increased crack growth resistance.

Contents

1 Motivation and aim of the present work

In the midst of the 20th century grain refinement was found to be an effective strengthening mechanism in metals [1], which, in contrast to other strategies, does not markedly reduce their ductility. Grain boundary strengthening allows the fabrication of materials, which can endure high mechanical stresses but still show plastic deformation before final failure, rather than abrupt catastrophic fracture. As strength increases with the reduction of the grain size, the production of metals with grain sizes smaller than one micrometer seems to be a promising strategy to obtain ultra-high strength and ductile materials. Indeed, in the last few decades nanocrystalline (NC) and ultrafine-grained (UFG) metals became famous for their high yield strengths and increased fatigue endurance limit in stress controlled tests compared to their coarse-grained counterparts [2–8]. However, in order to safely use these materials for engineering parts, also ductility, fracture toughness and fatigue crack growth (FCG) resistance have to be retained. Due to their high ductility, conventional coarse-grained metals show plastic deformation prior to final failure. Furthermore, ductile metals have the ability to reduce stress concentrations at cracks and defects by plastic deformation and the blunting of the crack tip, which hinders components with defects from failing catastrophically. Therefore, in order to safely use NC and UFG metals, it must be guaranteed that these materials exhibit an appropriate ductility and damage tolerance under quasi-static and cyclic loading. In the last few years, the fracture behavior of NC and UFG under quasi-static loading has been studied, showing that the fracture toughness can be deteriorated by severe grain refinement [9–13]. Nevertheless, the product of strength and fracture toughness, which gives information about the damage tolerance, is comparable or even higher than that of microcrystalline (MC) metals [13]. NC and UFG materials are also attractive for applications as cyclically loaded components due to their increased fatigue limit [3,14–16]. However, although a damage tolerant behavior is essential to ensure safe operation of such components, only few studies have focused on the fatigue crack growth (FCG) behavior of NC and UFG metals so far. The majority of the studies report a deteriorated FCG behavior, even though the origin of the deterioration is not fully understood [14–23]. Therefore, the present thesis should help to shed light onto the mechanisms, which govern the FCG in NC and UFG metals, in order to understand and finally overcome the negative effects of severe grain refinement on the FCG behavior. In the following introductory section, the production and mechanical properties of NC and UFG metals will be briefly described and a review of the existing literature on the FCG behavior of this class of materials will be given. The main results will be listed and discussed in section 3 and 4, more details can be found in the publications attached in the annex.

2 Introduction

2.1 Grain refinement by severe plastic deformation

There are several different methods to achieve fine-grained microstructures in classical metallurgy, however, only few of them allow producing UFG metals with grains smaller than 1 μm, or NC materials, with grains smaller than 100 nm. Besides electrodeposition (ED) [24], mechanical alloying [25,26] and gas phase condensation [2], severe plastic deformation (SPD) methods grant the possibility to generate these highly refined materials [4]. SPD methods have in common, that large strains are applied under

high hydrostatic pressure, which prevents the material from failing. The most prominent examples of SPD techniques are high pressure torsion (HPT), equal channel angular pressing (ECAP) and accumulative roll bonding (ARB), however, many more methods have been further-developed in recent years [27]. The UFG and NC metals investigated in this work were mainly fabricated by HPT, due to its ability to reach enormous strains of up to several thousand percent. For the HPT process a disc-shaped specimen is placed between two anvils and loaded under compressive stress in the range of a few GPa, as depicted in Fig. 1(a). One anvil is fixed and the other one rotates in order to induce shear strain in the material [28]. The shear strain γ can be calculated by:

$$\gamma = \frac{2*\pi*r*n}{t} \tag{1}$$

with n being the number of revolutions, r the radius and t the thickness of the sample. This can also be expressed as the von Mises strain ε_{vM}, which allows a better comparison to longitudinal strains, such as typically measured in a tensile test.

$$\varepsilon_{vM} = \frac{\gamma}{\sqrt{3}} \tag{2}$$

Investigations in the context of this thesis were also done on a shape-memory alloy, which was deformed by ECAP. For the ECAP process a billet of material is pressed through a die by a plunger, as shown in Fig. 1(b). Since the shape of the billet is not changed, this deformation step can be repeated to increase the applied shear strain. Additionally, the strain path can be changed by rotating the sample for a certain angle after each deformation step [29], as will be described later. The von Mises strain of N passes of ECAP, with a channel angle φ can be calculated by Equ. 2:

$$\varepsilon_{vM} = \frac{2}{\sqrt{3}} * \mathrm{N} * \cot\left(\frac{\phi}{2}\right) \tag{3}$$

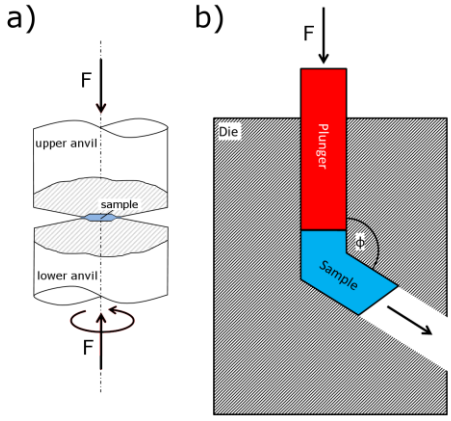

Fig. 1: Illustration of (a) the HPT process and (b) the ECAP process.

Regardless of the SPD method, the applied shear strain reduces the grain size, until equilibrium between grain fragmentation and restoration processes is reached. The grain size of the equilibrium microstructure depends primarily on the deformation temperature, the alloying level, the impurity of the material and the strain rate [30,31]. For alloyed metals, as for example austenitic steel, a mean grain size of less than 50 nm can be achieved, pure metals in general exhibit a larger grain size in the range of a few hundred nanometer. For many SPD techniques, the shearing of the material results in elongated grains,

with pancake- or cigar-like shapes, especially for HPT where the shearing direction is the same during the whole deformation process. An example of the microstructure of Ni after HPT deformation is taken from [32] and shown in Fig. 2. In ECAP the shear plane is also unchanged when the billet is not rotated between the deformation steps (route A). A rotation of the billet after each deformation step, e.g. by 90°, which is called route B_C, leads to more equiaxed grains, but grains are still slightly elongated parallel to the shear plane of the last ECAP pass. Regardless of the production route, UFG and NC microstructures can show remarkable mechanical properties, which will be discussed in the next section.

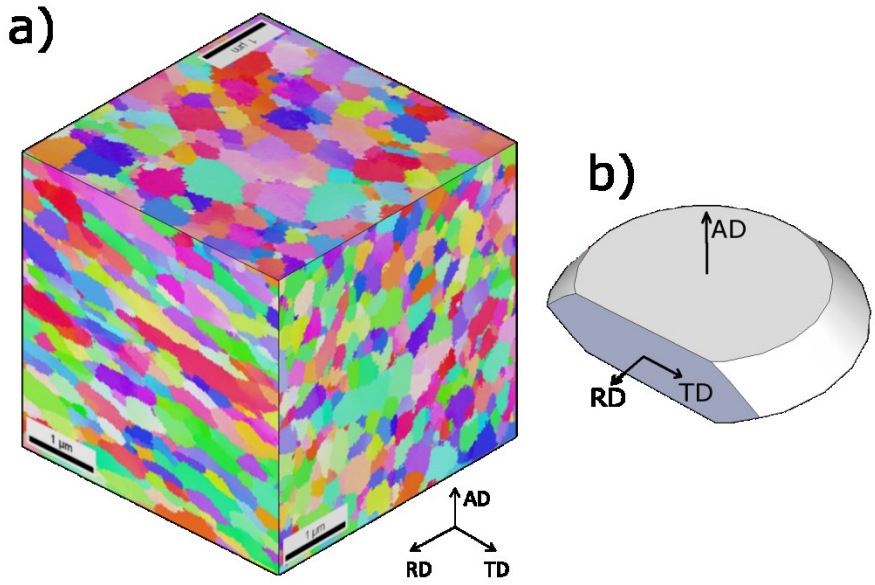

Fig. 2: Illustration of the microstructure of pure Ni, after 15 turns of HPT. (a) shows EBSD scans with different viewing directions in respect to the HPT process, taken from [32]. Grains are elongated in the shearing direction of the HPT process (tangential direction of the HPT disc, TD). In (b) the schematic of an HPT deformed disc, which was cut on one side, is presented, with the characteristic directions of the HPT process marked by arrows (axial direction AD, radial direction RD and tangential direction).

2.2 Mechanical properties of NC and UFG materials produced by SPD

The strength and ductility of NC and UFG materials has already been investigated by a large number of studies [6–8] and therefore only results, which are needed for the better understanding of fracture and fatigue crack growth properties will be presented in this section. Grain refinement by SPD methods is an effective way to strongly increase the strength of metals. Although UFG and NC metals show a trend to reduced ductility, strategies have been investigated to keep it at an acceptable level [6–8]. A peculiarity of SPD deformed metals is the frequent appearance of orientation dependent behavior in respect to several mechanical properties. For example, tensile tests on UFG Ni, produced by HPT revealed that besides an increased strength, the ultimate tensile strength (UTS) and the reduction in area of UFG Ni exhibit an orientation dependence [33]. It was concluded, that grain elongation and the shear texture are responsible for higher UTS and the larger reduction in area for samples loaded parallel to the shear plane of the HPT deformation.

In recent years, the damage tolerance of NC and UFG metals has gained attention, however, mainly for the case of quasi-static loading [10–13,34–38]. It was observed that in general the fracture toughness of severely plastically deformed materials is reduced, however, the damage tolerance expressed as the

product of fracture toughness and strength can be remarkably high. Furthermore, the fracture toughness was found to be strongly dependent on the grain shape and the orientation of the specimen. The resistance against crack growth is lower for cracks parallel to the shear plane, or in other words parallel to the longer axis of the elongated grains, than for cracks perpendicular to it.

Because of the improved fatigue limits of NC and UFG materials, they are potential candidates for the application in cyclically loaded components. However, in many components the existence of defects and cracks cannot be excluded, as they could originate from the production route or may be introduced during service. Thus, it is essential to investigate the fatigue crack growth behavior to assure a safe usage of these high strength materials.

2.2.1 Fatigue crack growth experiments

FCG experiments are performed on pre-cracked specimens loaded in mode I to determine the load amplitude, which is necessary for an existing crack to start to propagate. Furthermore, such experiments give information about the speed of the crack growth, once this load amplitude is exceeded. The stress intensity factor K describes the stress and strain field around the crack tip and is used to characterize the driving force for crack propagation. K is calculated from the applied load, the specimen geometry and the crack length, according to ASTM standard E647. For cyclic loads the stress intensity factor range ΔK can be determined from the maximum and minimum K by $\Delta K=K_{max}-K_{min}$. During the FCG test the crack length is measured, e.g. by the potential drop method, and the load cycles are counted. From this data the crack advance per cycle is determined, which is called FCG rate (da/dN). The FCG data is depicted in double-logarithmic diagrams, with ΔK on the abscissa and da/dN on the ordinate. Most materials show a FCG curve with distinct features: The crack starts to propagate when the applied ΔK is larger than the threshold stress intensity factor range ΔK_{th}. In stage I, also called the near-threshold regime, there is a strong increase in the FCG rate, which is followed by stage II, where the rate of the increase of da/dN becomes constant (linear relation in the double-logarithmic diagram). The dependence of the FCG rate on ΔK in stage II, which is also known as Paris regime, can be described by the Paris equation [39]:

$$\frac{da}{dN} = C * \Delta K^m \tag{4}$$

with C being a factor of proportionality and m the Paris exponent. In stage III, the increase of the FCG rate gets larger because the maximum K value approaches the fracture toughness of the material, which finally leads to the failure of the sample.

The full description of the FCG behavior of a material, however, is even more complex, as the FCG rate is not only dependent on ΔK but also influenced by the mean stress of the cyclic load. This means, that a given material can exhibit different FCG curves, depending on the loading condition. Besides ΔK as a measure for the amplitude, the load or stress ratio $R=F_{min}/F_{max}=\sigma_{min}/\sigma_{max}$ is used to characterize the mean stress of the loading. Experiments for this work were performed at load ratios of R=0.1, i.e. cyclic loading in tension with small mean stress, and at R=0.7, i.e. cyclic loading in tension with higher mean stress. Cyclic loading with a higher mean stress is in general more critical, as materials exhibit lower threshold values and higher FCG rates. Responsible for this change in the FCG behavior are crack closure and shielding mechanisms, which reduce the load at the crack tip [40–42]. Upon unloading, the crack faces can get in contact when the closure stress intensity factor K_{cl} is reached and the crack tip gets

further unloaded, even before the tensile load was reduced to the minimum load of the load cycle (depicted in Fig. 3). Thereby the stress intensity factor range acting at the crack tip is reduced to $\Delta K_{eff}=K_{max}-K_{cl}$, which leads to a smaller crack advance per cycle and a lower FCG rate. In ductile metals the pre-mature contact of the crack faces can for example originate from a plastic wedge (plasticity induced crack closure, PICC), from oxide debris close to the crack tip (oxide induced crack closure, OICC) or from asperities on the fracture surface (roughness induced crack closure, RICC). At a higher mean stress, which also means higher minimum and maximum stress of the cyclic load, the contributions of OICC and RICC diminish, as the opening of the crack gets larger than the oxide debris and the asperities of fracture surface, even at minimum load. With the reduction of crack closure contributions, ΔK_{th} is reduced and the FCG rate is increased, which means a lower FCG resistance.

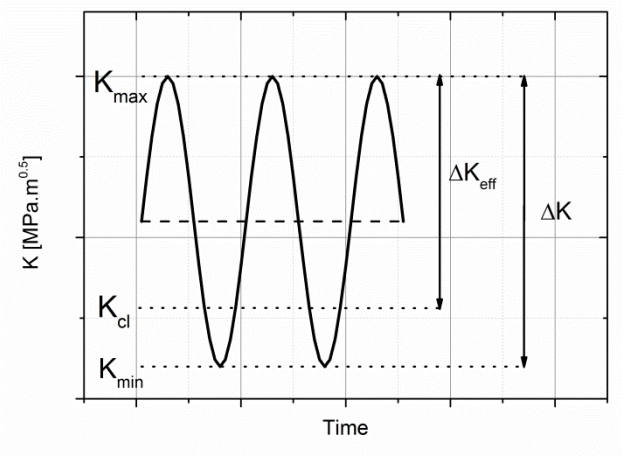

Fig. 3: Schematic of the cyclic load at a crack tip. The globally applied load results in a ΔK, which is given by $K_{max} - K_{min}$. Crack closure leads to premature contact of the crack faces upon unloading when ΔK is reduced to the closure level K_{cl}. Thus, the crack driving force at the crack tip is reduced and the crack tip is loaded only by the reduced ΔK_{eff}.

Because of crack closure it is more appropriate to characterize the FCG threshold by two quantities, the effective threshold stress intensity factor range, $\Delta K_{th,eff}$, and the long crack threshold stress intensity factor range, ΔK_{th}. With the commonly used load shedding technique only ΔK_{th} can be determined, which, however, is not necessarily conservative, as crack propagation could already occur at lower ΔK. The load rising method [43] allows the measurement of $\Delta K_{th,eff}$, which can be seen as the absolute minimum loading necessary for FCG. The procedure of the load rising method is depicted in Fig. 4: The FCG experiment is started with an open pre-crack and thus no crack closure mechanisms are active at the beginning. No crack growth takes place as long as ΔK is smaller than the effective threshold stress intensity factor range $\Delta K_{th,eff}$ (marked by $\Delta K < \Delta K_{th,eff}$ in Fig. 4(a)). When ΔK is increased to $\Delta K_{th,eff}$, first crack propagation occurs. However, during this first crack advance of a specific length, the different crack closure mechanisms build up, which reduce the load at the crack tip. The result is a retardation of the crack growth or even its stop. Subsequently, the globally applied ΔK has to be increased, in order to get further crack propagation. This can happen several times (marked by $\Delta K_{th,eff} < \Delta K < \Delta K_{th}$ in Fig. 4(a)), until finally the ΔK reaches the long crack threshold stress intensity factor range ΔK_{th} and the crack advances until final failure ($\Delta K > \Delta K_{th}$ in Fig. 4(a)). The crack advance, Δa, between $\Delta K_{th,eff}$ and ΔK_{th} can be plotted over ΔK, which is called the cyclic crack resistance curve (R-curve) of a material and is shown in Fig. 4(b). ΔK values larger than ΔK_{th} and the corresponding FCG rates, da/dN, are represented in FCG curves, with an example in Fig. 4(c).

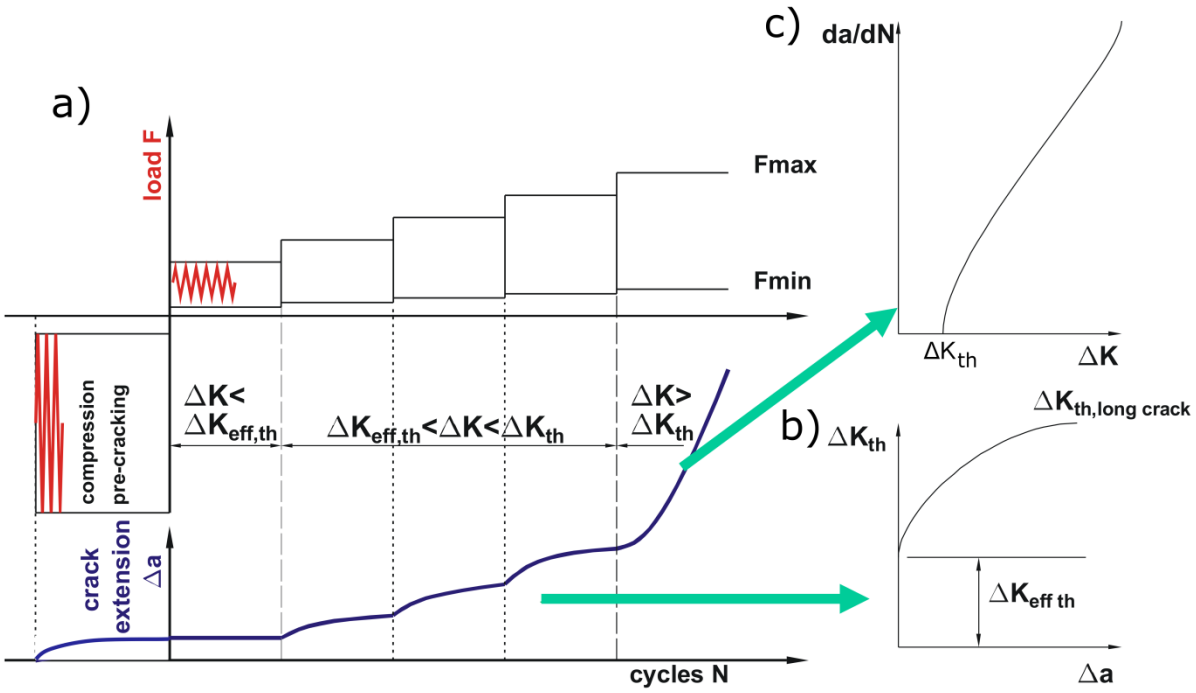

Fig. 4: Schematic diagrams of the load rising procedure for the determination of threshold values ($\Delta K_{th,eff}$ and ΔK_{th}), R-curves (b) and FCG curves (c). In (a) the load F and the crack extension a is plotted over the number of the applied load cycles N. In (b) an example of a cyclic R-curve is shown. In (c) an exemplary FCG curve is depicted. Diagrams redrawn from [43].

It is still difficult to predict the FCG properties of a material based on its microstructure or on other mechanical properties. In order to understand the microstructural influences on the threshold, the discrete nature of plasticity has to be taken into account. The first crack advance occurs, when a dislocation is emitted from the crack tip upon loading and able to return to the crack tip during unloading [44]. Therefore $\Delta K_{th,eff}$ is dependent on the resistance of the lattice against the emission of dislocations from the crack tip and their return [45]. In microcrystalline metals $\Delta K_{th,eff}$ can be related to the Young's modulus E and the length of the Burgers vector b:

$$\Delta K_{th,eff} \propto E * \sqrt{b} \tag{5}$$

It is more difficult, however, to estimate the long crack threshold ΔK_{th}, since it is strongly affected by crack closure mechanisms and therefore influenced by more material parameters, such as strength, fracture mode, grain size or susceptibility to oxidation. Nevertheless, it can be concluded that a higher Young's modulus and larger contributions from crack closure lead to a higher ΔK_{th}.

The FCG rate in the Paris regime can only be estimated, if there is information about the microscopic FCG mechanisms. The two most prominent models describe FCG either as being mainly governed by plastic deformation or by damage accumulation. In the first case, plastic deformation leads to a crack advance by the blunting and re-sharpening of the crack tip. Thus, a proportionality of the FCG rate to the cyclic crack tip opening displacement ($\Delta CTOD$) and hence a proportionality of (da/dN) to ΔK^2 is predicted [46–49] by:

$$\left(\frac{da}{dN}\right)_{pl.\ deformation} = c * \Delta CTOD = c * d_n * \frac{\Delta K^2}{2*\sigma_y*E} \quad (6)$$

where c is a dimensionless factor and depends on the geometry of the crack tip, σ_y is the yield strength, E the Young's modulus and d_n a factor dependent on the cyclic hardening behavior of the material. This results in an expected exponent m of 2 in the Paris equation, which is equivalent to the slope of the FCG curve in the Pairs regime.

Damage accumulation based models of FCG, in contrast, would yield an exponent of 4 [50]. In this model the occurrence of damage ahead of the crack tip is assumed, which can generate for example microcracks or voids. Coalescence of these flaws with the main crack finally leads to crack advance. Cracks can also grow when cyclic plastic deformation accumulates vacancies, which reduces the de-cohesion energy and results in a local fracture after the density of vacancies has reached a critical value.

The FCG experiments on UFG and NC metals of the present thesis should help to refine the knowledge about the basic mechanisms governing the FCG growth of metals. Furthermore, they should help to assess the damage tolerance of this new group of materials for applications under cyclic loading. Preceding studies on this topic will be briefly reviewed in the next section.

2.3 Literature review

Several studies on the fatigue and FCG behavior of UFG and NC metals have been published in the last 15 years. Hanlon et al. [14] investigated the fatigue behavior of nickel produced by ED, which was subsequently heat treated to get specimens with grain sizes from NC to MC. With decreasing grain size an increase in the resistance against crack initiation was found, connected with a lower FCG resistance and faster FCG especially in the near-threshold regime. The same tendencies were observed for an Al-Mg alloy in UFG and MC state [14]. In a further study on the same materials (and additionally Ti) it was shown that the effect of the load ratio on ΔK_{th} and the FCG rate diminishes with decreasing grain size [15]. From FCG experiments on MC metals it is obvious that a higher load ratio (R=0.7 or 0.3, instead of R=0.1) goes along with a lower ΔK_{th} and a higher FCG rate. For UFG Ni this behavior also clearly exists, for NC Ni however, FCG curves at different load ratios lie closer together and almost coincide at higher ΔK. This change is explained by a reduction of roughness induced crack closure (RICC) at low mean stresses (low load ratios) as a result of a less tortuous crack path of UFG Ni compared to coarser-grained microstructures. Lower FCG rates of MC microstructures could also be the result of lower effective stress intensity factors for regularly deflected cracks. However, by curve fitting the latter contribution was found to be small compared to RICC [15]. The same model was appropriate to predict the FCG rates in the near-threshold regime of Ti. It is important to mention that the Ni samples had a thickness of only 100 - 150 µm and thus plane stress conditions are likely to prevail even at low ΔK values.

In [18] Collini reviewed his work and other publications on the FCG resistance of UFG copper. He performed FCG tests on ECAPed Cu with 99.90% purity (8 passes B_C, average grain size 300 nm) and found lower FCG rates compared to other studies on UFG copper with higher purities and also compared to MC Cu (15 µm). The increased resistance against FCG is attributed to an enhanced stability of the microstructure because of the presence of impurities and precipitates. In UFG material more grains lie within the plastic zone, which results in a more homogeneous deformation. Interaction of the

crack with grain boundaries and precipitates can additionally retard FCG due to crack deflection [51]. A typical load ratio effect is reported for the near-threshold regime of the UFG Cu samples. A higher ΔK_{th} and a lower FCG rate can be observed for R=0.1 compared to higher R-ratios. FCG data measured at R-ratios higher than 0.3 show only small differences. A comparison of the CTOD and crack path roughness reveals that RICC can only be active in the near-threshold regime, whereas PICC could be active also at higher ΔK. However, in the Paris regime FCG curves of all R-ratios coincide, indicating a negligible contribution of PICC. At high ΔK FCG appears to be slightly faster at R=0.1. Fracture surface analyses showed that more bifurcations, crack branching and multi-cracking occur with higher applied load amplitudes and higher mean stresses, which is known to increase FCG resistance. This could explain the lower FCG rate for higher R-ratios at high ΔK.

Padilla and Boyce [19] reviewed the fatigue behavior of NC and UFG metals and also commented on FCG. They noticed that no clear trends can be seen when the works of different groups are compared. They consider the different processing routes (and thus different level of impurities), varying testing techniques and differences in sample thickness to be the reason. In general the resistance against FCG is reduced with decreasing grain size. Especially the load ratio effect diminishes, indicating a reduced contribution of crack closure. It is argued that RICC is expected to disappear because the crack path roughness is reduced and PICC vanishes because of limited dislocation mediated plasticity. Less crack closure can also explain reduced ΔK_{th} values at low load ratios, which are frequently observed for NC and UFG metals. Fracture surface analyses yield quite different results, even if experiments are done on the same metal, e.g. nickel. Generally speaking, at low ΔK smaller crack path tortuosity and more intergranular fracture are observed. At higher loads some studies found striations or dimpled structure and ductile dimpled fracture when K_{max} approaches the fracture toughness. For NC metals simulations suggest that voids and microcracks on grain boundaries play an important role in the FCG process, formed e.g. by grain boundary sliding [52,53]. Furthermore simulations revealed that at triple points intergranular cracks advance preferably along grain boundaries with small angles to the overall crack growth direction, as it requires the lowest energy [54]. Less blunting of a crack in NC metals is predicted by simulations, as less dislocations can be emitted from the crack tip due to enhanced suppression of dislocation emission by pile-ups in the small grains [55].

Vinogradov et al. [37] investigated the fracture and fatigue resistance behavior of a UFG CuCrZr alloy. They observed that the UFG Cu alloy shows the same stages of FCG as conventional coarse-grained materials, i.e. slow crack advance in the near-threshold region, followed by stable crack growth in the Paris regime and finally unstable crack growth at high ΔK. The transition from near-threshold behavior to stable crack growth was also in focus in this work. Usually this transition occurs when the size of the cyclic plastic zone (CPZ) becomes comparable to the grain size of a material. This is not the case for the investigated UFG Cu, where the CPZ spans several grains even at the threshold. They conclude that therefore non-equilibrium grain boundaries have to play an important role for the accommodation and transfer of plastic slip. The UFG Cu was produced by ECAP and CT samples with different orientations in relation to the extrusion direction were tested. In contrast to tensile experiments, in FCG tests no differences were found for the differently orientated samples, with cracks introduced in extrusion and tangential direction.

Hübner et al. [21] observed only a small dependence of FCG rates on the R-ratio for UFG Cu, Ti and Al-1.5MgScZr. Higher R-ratios resulted in slightly lower threshold, however, in the Paris regime there was hardly any difference.

In the review paper [16] Vinogradov points out that for UFG Cu a lower threshold and a higher FCG rate in the near-threshold regime has been found compared to MC Cu. At higher ΔK, however, the fatigue crack propagation is faster in the MC specimens. The higher FCG rate in the near-threshold regime is explained by the straighter crack path of UFG Cu. Vinogradov also comments on the FCG mechanisms, which seems to occur in a ductile manner, as even striations can be seen on the fracture surfaces of UFG Cu. Also the proportionality of the FCG rate to $(\Delta K)^2$ indicates that crack advance is controlled by local plasticity. However, this would also predict an inverse dependence of the FCG rate on the yield strength, which was not observed in experiments. When FCG occurs by void formation, crack coalescence and re-nucleation, damage accumulation models are appropriate and predict the FCG rate to be proportional to $(\Delta K)^4$. Paris exponents m between 2 and 4 suppose that both mechanisms are active at the same time.

FCG data of UFG bcc metals is scarce, with the work of Kim et al. [22] as one example. They performed FCG experiments on an ECAPed low carbon steel with a ferritic microstructure in the UFG state and a grain size of 500 nm, after an annealing treatment at 753 K for 72 h. A lower threshold and higher FCG rate was measured for UFG steel samples compared to MC specimens (30 μm), however, differences were smaller than in studies of fcc metals, especially at higher ΔK. Like already discussed for fcc metals, the *R*-ratio effect was also hardly visible, which means that there was little contribution of crack closure. As they observed quasi-cleavage, they assumed that PICC can be neglected. The small influence of RICC is explained by the much smoother crack path of UFG specimens compared to coarser-grained steel samples. The flat fracture surface of UFG steel is attributed to the relation of the cyclic plastic zone (CPZ) size to the grain size. In UFG metal the CPZ is usually larger than the grain size and thus planar slip bands can form in several grains, resulting in a straight crack growth. Furthermore a CPZ larger than the grain size hinders reverse slip of dislocations and thus leads to more accumulation of damage. However, the higher yield stress of the UFG microstructure results in a lower ΔCTOD and hence in a smaller crack advance per cycle. Kim et. al argue that this behavior compensates the tendency for faster crack growth due to increased damage accumulation and less crack closure, so that in the end there is a small difference between the FCG behavior of UFG and MC samples.

Niendorf et al. [23] conducted FCG experiments on UFG interstitial-free (IF) steel, produced by different ECAP routes. In accordance to studies on other materials mentioned above, they also observed a decrease in ΔK_{th} and an increase of the FCG rate in the near-threshold regime with decreasing grain size. In the Paris regime these differences vanish and FCG rates are comparable for MC and UFG samples, regardless of their production route. UFG samples with elongated microstructures (e.g. produced by 2 A passes) show more scatter in the near-threshold regime than more equiaxed structures (e.g. produced by 8 B_C passes). The FCG curves of 8 B_C samples show hardly any orientation dependence, as it was also observed for ECAPed Cu [37]. It is interesting to note that differences exist in the global crack path of samples from different production routes and with different orientations. In general cracks seem to favor growth directions parallel to the shear plane of the last or penultimate ECAP pass, even if the microstructure is fairly equiaxed. Cracks in specimens from 16E and 8 B_C change their crack growth direction to about 10° to 30°. In samples with pre-cracks introduced in extrusion

direction this new crack growth direction coincides with the direction of the last ECAP shear plane, in samples with cracks in tangential direction it can be linked to the penultimate ECAP shear plane. It can further be seen that cracks tend to follow the elongated structures (which also exist in 8 B_C material to a certain extent) along the grain boundaries. Stress concentrations due to elongated grains are seen as the reason for the deviations. As only weak texture was found, it is assumed that it plays a minor role in deviating FCG cracks.

To conclude, the contemporary literature contains many aspects of the FCG behavior of UFG and NC materials. Most of them have in common, that a tendency to lower ΔK_{th} values and to higher FCG rates is observed for the very fine-grained metals. However, due to the application of different measurement methods and the use of non-standard samples, results are difficult to compare. Unfortunately, the individual investigations are mostly limited to one metal and therefore it is hardly possible to find similarities and trends valid for larger groups of materials. Furthermore, the FCG tests are often performed at one load ratio only, which makes it difficult to separate the extrinsic effect of crack closure from the intrinsic FCG resistance. For the present thesis, a large variety of materials, ranging from pure to complex engineering metals with coarse-grained to nanocrystalline microstructures, are tested at two load ratios, using the same testing method. This allows to overcome the afore-mentioned problems and to reveal trends of the FCG behavior of UFG and NC materials.

3 Results

In order to get a better understanding for the effect of SPD on the FCG behavior, experiments were performed on a broad range of materials in their microcrystalline and severely plastically deformed UFG or NC state. As examples for pure metals, ARMCO iron with a body-centered cubic crystal structure and high purity nickel with a face-centered cubic crystal structure were taken. Additionally, industrial alloys were tested: an austenitic steel type 316L produced by "Böhler Edelstahl GmbH" (further denoted as A220), two pearlitic steels produced by "voestalpine Schienen GmbH" type R260 and R350, as well as a superelastic 50.2 % Ni – 49.8 % Ti alloy, further denoted as NiTi. An overview on the production routes, the mechanical properties and the results of the FCG tests of all tested material states is given in Table 1. In order to assess the orientation dependence of FCG in UFG and NC metals, samples with differently oriented cracks in respect to the deformation route were produced. Orientations are denoted according to E399 [38], with the first letter indicating the direction of the crack surface normal and the second letter indicating the crack growth direction. The directions are related to the SPD process, with three distinct directions for HPT: axial direction (A), radial direction (R) and tangential direction (T), see Fig. 5(a). For the ECAP process two directions can be distinguished: extrusion direction (E) and radial direction (R), see Fig. 5(b). Tests were performed at low mean stresses (R=0.1) and high mean stresses (R=0.7), in order to account for the influence of crack closure mechanisms.

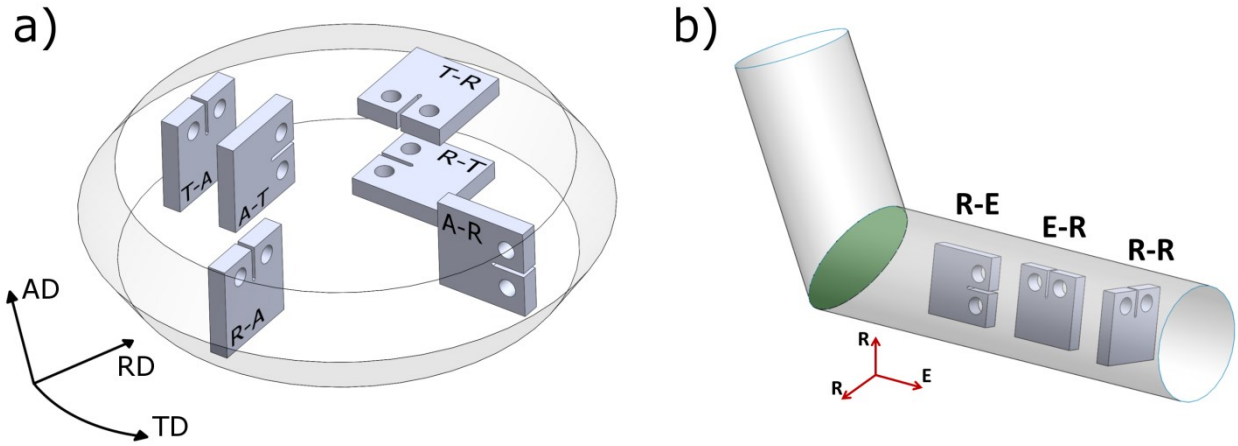

Fig. 5: Sample orientations in (a) HPT and (b) ECAP deformed material. In HPT deformed material it can be distinguished between axial direction AD, radial direction RD and tangential direction TD. In ECAPed materials it can be differentiated between radial direction R and extrusion direction E. The orientation of CT samples in respect to the deformation process is denoted by two letters, corresponding to the direction of the crack plane normal and the crack growth direction.

In the following sections, the main findings on the FCG behavior of the afore-mentioned materials will be discussed individually and finally compared. Especially the following aspects will be in focus:

- The fracture mode during FCG (trans- or intergranular fracture)
- Orientation dependence of the FCG behavior
- Influence of grain refinement on ΔK_{th}
- Influence of grain refinement on the FCG rate in the Paris regime
- Cyclic R-curve behavior

Table 1: Overview of the production routes, the microstructural properties and selected FCG results of the tested materials.

		ARMCO Fe		A220		R260		R350	Ni		NiTi	
	Production Method	HPT	HPT	AR	HPT	HPT	HPT	HPT	AR	HPT	ED	AR	ECAP B_C
	Heat Treatment	650°C 1h	-	900°C 30min	-	550°C 30min	-	-	-	-	-	-	450°C
	ε_{VM} [-]	14-100	14-100	-	14-100	14-100	1.2	1.2	-	14-100	-	-	6.5
	Young's modulus [GPa]	210	210	210	210	210	210	210	205	205	205	68	68
	Mean Hardness [HV0.5]	105	410	160	502	597	380	445	120	280	470	240	300
	Grain size	15 µm	500x400x 150 nm	75 µm	50 nm	50 nm	200 nm	-	50 µm	750x450x 250 nm	30 nm	100 µm	100 nm - 5 µm
	Mean grain size	15 µm	310 nm	75 µm	50 nm	50 nm	200 nm	-	50 µm	410 nm	30 nm	100 µm	1 µm
	Fracture mode	transg.	interg.	transg.	interg.	interg.	transg.	transg.	transg.-interg.	interg.	interg.	transg.	transg.
	R-curve	yes	no	yes	no	yes	yes	yes	yes	no	no	yes	yes
	m [-]	3	3	2 - 3	2 - 3	2 - 3	2 - 3	2	2	2	2	3	3
	Difference da/dN_{A-T} / da/dN_{T-R} [-]	-	10	-	1	2	2	4	-	4	-	-	1
R=0.1	$\Delta K_{th,eff}$ [MPa.m$^{0.5}$]	2.7	3.7 - 4.0	2.0	2.0 -3.2	2.4 - 2.6	2.6 - 3.6	3.0	3.0 - 4.0	1.8 - 2.4	2.0	1.1	1.0
	ΔK_{th} [MPa.m$^{0.5}$]	3.8 - 4.0	3.7 - 4.0	2.7	2.0 -3.2	3.1 - 3.2	3.0 - 4.0	3.9	4.3 - 4.4	3.3 - 4.63	1.8 - 2.4	2.0	1.6	1.3 - 2.4
R=0.7	$\Delta K_{th,eff}$ [MPa.m$^{0.5}$]	2.9	3.1 - 3.3	2.0	2.2	2.4 - 2.6	3.0			2.6	1.7 - 2.2	2.1	0.9	0.8 - 1.0
	ΔK_{th} [MPa.m$^{0.5}$]	2.9	3.1 - 3.3	2.7	2.2	2.4 - 2.6	3.2			2.8	1.7 - 2.2	2.1	0.9	0.8 - 1.0
R=0.1 min	da/dN at 10 MPa.m$^{0.5}$ [m/cycle]	7.00E-09	1.00E-08	5.00E-09	3.50E-08	2.00E-08	1.50E-08	3.00E-08	7.00E-09	3.00E-08	1.00E-08	2.50E-08	5.00E-08	8.00E-08
R=0.1 max	da/dN at 10 MPa.m$^{0.5}$ [m/cycle]		1.00E-07		3.30E-08	2.30E-08	2.50E-08		2.50E-08		4.00E-08			
R=0.7 min	da/dN at 10 MPa.m$^{0.5}$ [m/cycle]	7.00E-09	1.00E-08	1.00E-08	4.50E-08	2.80E-08	1.50E-08			3.50E-08	1.00E-08	2.50E-08	7.00E-08	7.00E-07
R=0.7 max	da/dN at 10 MPa.m$^{0.5}$ [m/cycle]		1.00E-07		6.70E-08	4.60E-08	1.00E-07				1.00E-07			

3.1 ARMCO iron

ARMCO Fe with several different grain sizes was chosen as a model material for pure bcc metals to study the effect of grain refinement on the FCG behavior. Samples with grain sizes ranging from 3 to 15 µm were tested as examples for the MC state. In order to obtain UFG Fe, HPT deformation was applied to MC ARMCO Fe, which led to an UFG microstructure consisting of elongated grains with the average dimensions of 500x400x150 nm³ with the longest grain length parallel to the shear direction of the HPT process. The following discussion is based on results from FCG tests on UFG Fe, which are described in more detail in publication C.

Fracture surface analyses after the FCG tests revealed, that the grain refinement was accompanied by a change in the fracture mode from transgranular fracture in MC Fe to intergranular fracture in UFG Fe. Regular slip steps on the fracture surface of UFG Fe indicate that this change in the fracture mode is not a result of grain boundary embrittlement and local static fracture, and FCG is still controlled by a blunting and re-sharpening process. This indicates that in UFG materials the blunting process and crack growth takes place along the grain boundaries, rather than within the grains, as it is the case for coarse-grained metals. When blunting and re-sharpening is assumed to be the dominating FCG mechanism, the FCG rates in the Paris regime can be estimated from Equ. 3, due to the proportionality between $\Delta CTOD$ and the FCG rate. Since the measured FCG rates of UFG Fe are lower or in the range of this analytical model, it can be excluded that local brittle fracture has a significant contribution to FCG, as this would increase FCG rates above the estimations for deformation controlled FCG. Although these observations are in favor of FCG by blunting and re-sharpening it is still not fully clear why the Paris exponent m of MC and UFG Fe is about 3 instead of 2, as predicted by deformation based FCG models. An increased exponent could be the result of various effects:

- Even at the highest tested ΔK values the material is still in the near-threshold regime with a higher slope of the FCG curve.
- Contributions from damage accumulation and local static fracture accelerate the FCG process, which increases the Paris exponent m.
- Reduced fracture toughness could lead to a direct transition from near-threshold regime to stage 3 FCG, with a very limited Paris regime.

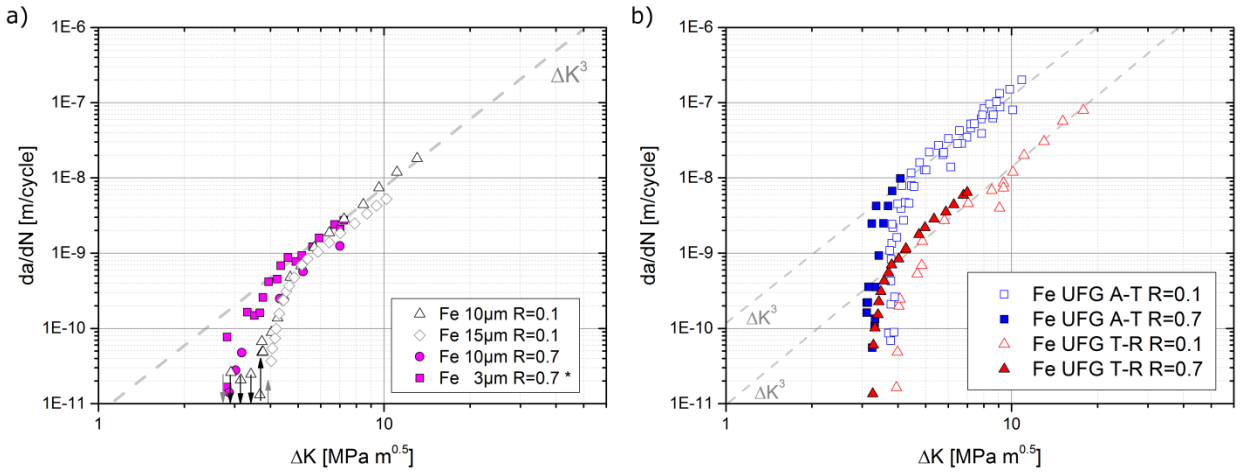

Fig. 6: FCG diagrams of (a) MC ARMCO Fe and (b) UFG ARMCO Fe with two different orientations tested at R=0.1 and R=0.7. In (a) data from [56] is included and marked by *. Gray dashed lines are shown as guide lines for the proportionality of (da/dN) to ΔK^3.

No marked influence of the grain size reduction on the threshold stress intensity factor range ΔK_{th} was found, as it can be seen in the FCG curves in Fig. 6(a) and (b). Especially at high R-ratios, where crack closure contributions are minimized, both MC and UFG Fe showed similar ΔK_{th} values of approximately 3 MPa.m$^{0.5}$. Also the long-crack threshold values ΔK_{th} at lower R-ratios are comparable for MC and UFG Fe, with values of about 4 MPa.m$^{0.5}$. The occurrence of a cyclic R-curve, however, was only observed for MC Fe at R=0.1. In UFG Fe, even at R=0.1, no crack growth was detected before ΔK_{th}. This could be explained either by the absence of a cyclic R-curve behavior or by very small crack extensions, which are smaller than the detection limit of the potential drop method, which is in the range of one micron.

In UFG Fe no pronounced anisotropy of ΔK_{th} between the two sample orientations A-T and T-R was found. This is reasonable, as dislocations emitted from the crack tip experience the same forces, due to the same Young's moduli and the same characteristic distances from obstacles in the form of grain boundaries, regardless of the orientation. In the Paris regime, however, significant differences exist, with a 10 times higher FCG rate for cracks with A-T orientation compared to T-R oriented cracks. This difference seems to be a result of the crack orientation in respect to grain shape of the severely plastically deformed Fe. Fracture surface analyses show that grain boundaries are the preferred crack path in UFG Fe under cyclic loading, regardless of the crack orientation. In the case of A-T samples, where the designated crack growth direction is parallel to the longer axis of the elongated grains, the cracks can follow long grain boundaries without large deviations. This is in contrast to T-R samples, where cracks are deviated more frequently, as their growth direction is perpendicular to the grain elongation direction (see Fig. 10 in publication B). The extensive regular crack deflection and branching in T-R samples, which also results in a more tortuous crack path and a rougher fracture surface, can be seen as geometrical shielding, as it reduces the local load at the crack tip and therefore the FCG rate. The reduction of the FCG rate as a geometrical effect of the more tortuous crack path was estimated in publication C. However, the differences in the measured FCG rates are larger than expected from the calculations based on the analytical model for regular crack path deviations and thus it cannot fully explain the FCG anisotropy. The orientation of the crack can also influence the crack tip opening angle and therefore the factor c in Equ. 6. Thereby, the crack advance per cycle and hence the FCG rate would be changed. The effect of the crack tip opening angle on the FCG rate is further explained in publication C, and illustrated in Fig. C-8.

Comparing the FCG rates in the Paris regime of MC Fe to UFG Fe shows that the FCG rate is lower in MC Fe. Therefore it can be concluded, that the intergranular fracture during FCG, as it occurs in UFG Fe, is disadvantageous. It seems, however, that the negative effect of intergranular fracture can be mitigated by an increased FCG resistance for cracks oriented perpendicular to the long axis of the elongated grains, as it is the case in T-R samples. Furthermore, an increase in strength should also lead to a lower FCG rate, as it results in smaller $\Delta CTOD$ and therefore, reduces the crack advance per cycle. Thereby the FCG rates of MC Fe and UFG Fe with T-R orientation are similar, although other mechanical properties, such as strength, are significantly improved.

3.2 Pure Nickel

The FCG behavior of MC Ni with a grain size of about 50 μm was compared to that of UFG Ni and NC Ni to investigate the grain size dependence of the fatigue crack propagation of face-centered cubic metals. An UFG microstructure with a mean grain size of 750x450x250 nm³ was achieved by HPT deformation of coarse-grained high purity nickel at room temperature, see Fig. 2. NC Ni with a grain size of about 30 nm was produced by electrodeposition [36,57–59]. Many similarities to the FCG in bcc ARMCO Fe exist, including the change from transgranular fracture in the case of MC Ni in the near-threshold regime, to intergranular fracture for UFG and NC Ni. On the fracture surfaces of all material states slip steps are visible, indicating that the FCG is again the result of a blunting and re-sharpening process, as it was also argued for ARMCO Fe. In contrast to Fe, all FCG curves of nickel samples showed a Paris exponent m of about 2, which additionally supports the assumption of a deformation dominated FCG.

The near-threshold behavior of Ni seems to be deteriorated by the grain size reduction, with lower threshold values for UFG and NC Ni specimens than for MC Ni samples, as it can be seen in the FCG diagrams in Fig. 7 and from data in Table 1. First crack extensions in MC Ni samples were detected at $\Delta K_{th,eff}$ values of 2.6 MPa.m$^{0.5}$ and 3.0 MPa.m$^{0.5}$ at load ratios of R=0.7 and R=0.1, respectively. In UFG and NC Ni specimens, however, first crack propagation already occurred at ΔK values of 1.7 to 2.4 MPa.m$^{0.5}$. This could be a result of a statistically variation of the distance between the crack tip of the pre-crack and the next grain boundary in UFG and NC Ni. Thereby more pronounced dislocation pile-ups could occur at the grain boundaries of UFG and NC metals upon loading, resulting in higher repulsive forces on dislocations upon unloading. Therefore, the return of dislocations to the crack tip occurs at smaller ΔK values in UFG and NC materials, which means a decrease of $\Delta K_{th,eff}$. More details can be found in publication B.

The long-crack threshold values ΔK_{th} of UFG and NC Ni with 1.7 to 3.0 MPa.m$^{0.5}$ are also lower than for MC Ni (3.3 to 4.6 MPa.m$^{0.5}$). Additionally, cyclic R-curve behavior was observed for MC Ni, but not for UFG and NC Ni. The vanishing R-curve behavior and the lower ΔK_{th} values of UFG and NC Ni compared to MC Ni lead to the conclusion, that the contributions from crack closure are significantly reduced for very fine-grained microstructures. This is an effect of small mode II displacements of the crack faces in UFG and NC material, which reduces roughness induced crack closure, as well as due to grain coarsening in the vicinity of the crack tip and the resulting reduction of plasticity induced crack closure. A more detailed explanation is given in publication B. Furthermore, MC Ni exhibits higher ΔK_{th} values, since the cyclic plastic zone is significantly smaller than the grain size and hence transgranular fracture is promoted, instead of the possibility to follow the weak crack path along grain boundaries as in UFG and NC Ni.

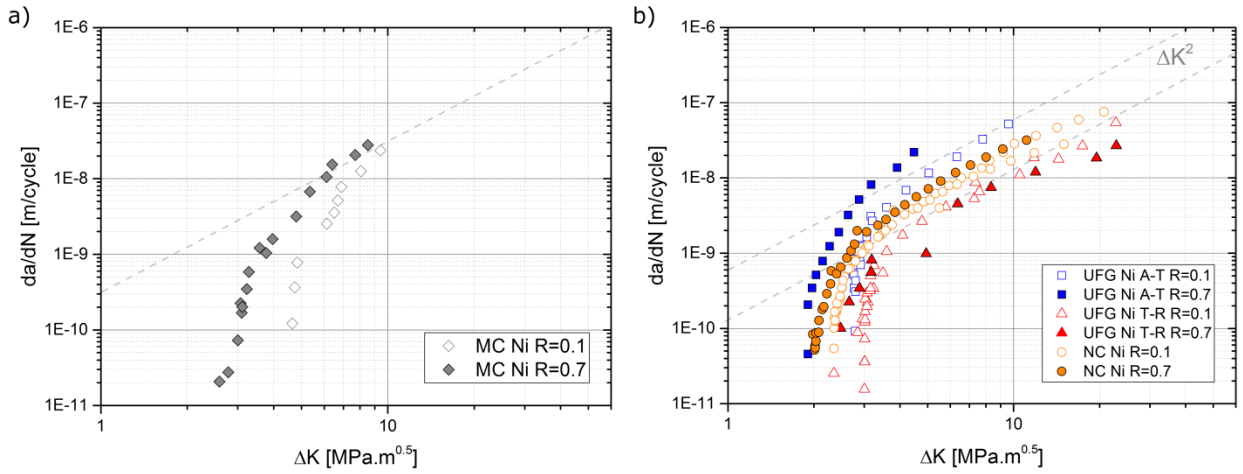

Fig. 7: FCG of (a) MC Ni and (b) UFG Ni with two different orientations and NC Ni tested at R=0.1 and R=0.7. Gray dashed lines are shown as guide lines for the proportionality to of (da/dN) to ΔK^2.

The FCG anisotropy of UFG Ni produced by HPT is less pronounced than in UFG Fe, however, FCG of A-T oriented cracks in the Paris regime is still by a factor of 4 faster than in T-R samples (see Fig. 7(b)). The FCG curve of NC Ni lies in between the FCG curves of UFG Ni A-T and T-R samples. Similar to UFG Fe, the differences in the FCG rates can be linked to the crack orientation in relation to the grain elongation direction. FCG perpendicular to the long axis of the grains leads to higher FCG resistance (T-R samples), than parallel to it. Further explanations have already been given in section 3.1 and are further discussed in publication B.

Finally it should be noted, that for UFG Ni with A-T orientation a two times higher FCG rate was observed compared to NC Ni, although the crack path tortuosities are comparable. The difference can be explained by the higher strength of the NC Ni, which leads to smaller cyclic crack tip opening displacements and thus to a lower FCG rate.

3.3 Austenitic steel A220

HPT processing of the austenitic steel type A220 leads to a nanocrystalline microstructure with a mean grain size of about 50 nm [60]. FCG experiments were performed on this SPD material and the results compared to the FCG properties of MC A220 and to results from literature on coarse-grained (CG) A220. As also observed for ARMCO Fe and Ni, severe grain refinement resulted in a transition from transgranular fracture in MC A220 samples to intergranular fracture in NC A220. This indicates that grain boundaries are the preferred crack path under cyclic loading.

The FCG properties of the tested MC A220 with a grain size of about 75 µm are compared in Fig. 8(a) to results from literature on the same material, however, with a coarser-grained microstructure (grain size ~ 1 mm) [61]. It can be seen, that the FCG curves and threshold values are quite similar for high load ratios (R=0.7), but differ strongly for R=0.1. From this difference it can be concluded, that the contribution of crack closure mechanisms, which are pronounced in CG A220 and result in different ΔK_{th} values for R=0.1 and R=0.7, are significantly reduced for the finer-grained microstructure of MC A220. Although the ΔK_{th} of MC A220 are similar for R=0.1 and R=0.7, slightly higher FCG rates are measured in the Paris regime for R=0.7.

A further reduction of the grain size leads to even less pronounced crack closure contributions, as can be seen by the coincidence of R=0.1 and R=0.7 FCG curves of NC A220 samples in Fig. 8(b).

A comparison of the FCG curves of MC A220 with the HPT deformed NC A220 reveals that the grain refinement hardly affects the near-threshold FCG behavior, despite an increase in hardness by a factor larger than 3 and a reduction of the grain size by three orders of magnitude. The threshold values of MC and NC A220 are comparable, with 2.0 – 2.7 MPa.m$^{0.5}$ for MC A220 and 2.0 – 3.2 MPa.m$^{0.5}$ for NC A220, see Table 1. In the Paris regime faster FCG was observed for NC A220, with four times higher FCG at R=0.7 compared to MC A220. The difference is even larger at R=0.1, as beneficial crack closure contributions are active to a small extent in MC A220, but further reduced in NC A220.

Hardly any FCG anisotropy was found for the differently oriented samples of NC A220. The FCG curves coincide and differences lie within the scatter of the measurement. This seems to be the result of the significantly smaller and less elongated grains, compared to HPT deformed Ni and ARMCO Fe. The reduced grain size results in smaller deflections of the crack in the case of the T-R orientation and the effect of geometrical shielding diminishes.

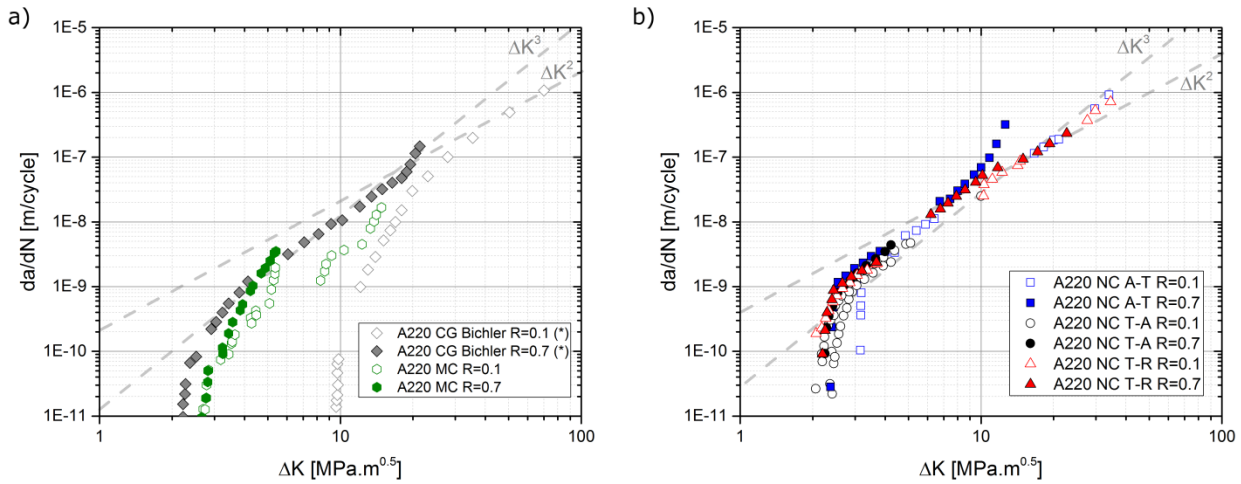

Fig. 8: FCG diagrams of (a) MC A220 and (b) NC A220. Fig. (a) includes FCG data from coarse-grained A220 redrawn from [62]. Gray dashed lines are shown as guide lines for the proportionality of (da/dN) to ΔK^2 and ΔK^3.

Exposing NC A220 to a temperature of 550°C for 30 minutes, leads to an increase in hardness from 502 HV to 597 HV due to dislocation annihilation and relaxation processes, without changing the grain size of the microstructure [60]. Therefore, comparing the FCG properties of this heat treated NC A220 (further denominated as NC A220 HT) to the as-deformed NC A220 can help to separate the effect of the increase in strength from the effect of a change in grain size. The FCG curves of as-deformed and heat treated samples are shown in Fig. 9(a) for orientation A-T and Fig. 9(b) for orientation T-R. The R=0.7 curves are fitted by dashed lines and the heat treated counterparts by dash-dotted lines. Thereby it can be seen that the increase in strength results in a reduction of the FCG rate by a factor of about 0.7. When a blunting and re-sharpening process is assumed to be the dominating FCG mechanism, the FCG rate can be estimated by Equ. 6. This leads to the following estimation of the change of the FCG rate as a result of a change in hardness:

$$\left(\frac{da}{dN}\right)_{HT} \cong \frac{\sigma_y^{AD}}{\sigma_y^{HT}} * \left(\frac{da}{dN}\right)_{AD} \cong \frac{H^{AD}}{H^{HT}} * \left(\frac{da}{dN}\right)_{AD} \cong 0.84 * \left(\frac{da}{dN}\right)_{AD} \quad (7)$$

with σ_y being the yield strength, H the hardness and the superscripts AD and HT for the as-deformed and heat-treated state, respectively. The estimation yields a difference of a factor 0.84, which is close to the difference actually measured from the FCG diagrams and thus further supports the assumption that FCG of NC A220 is mainly governed by plastic deformation. This leads to the conclusion that an increase in strength results in a reduced FCG rate, regardless if it originates from grain refinement or other strengthening mechanisms. However, this is only valid as long as the fracture mode remains unchanged and only for situations where crack closure mechanisms do not play an important role (e.g. at high mean stresses).

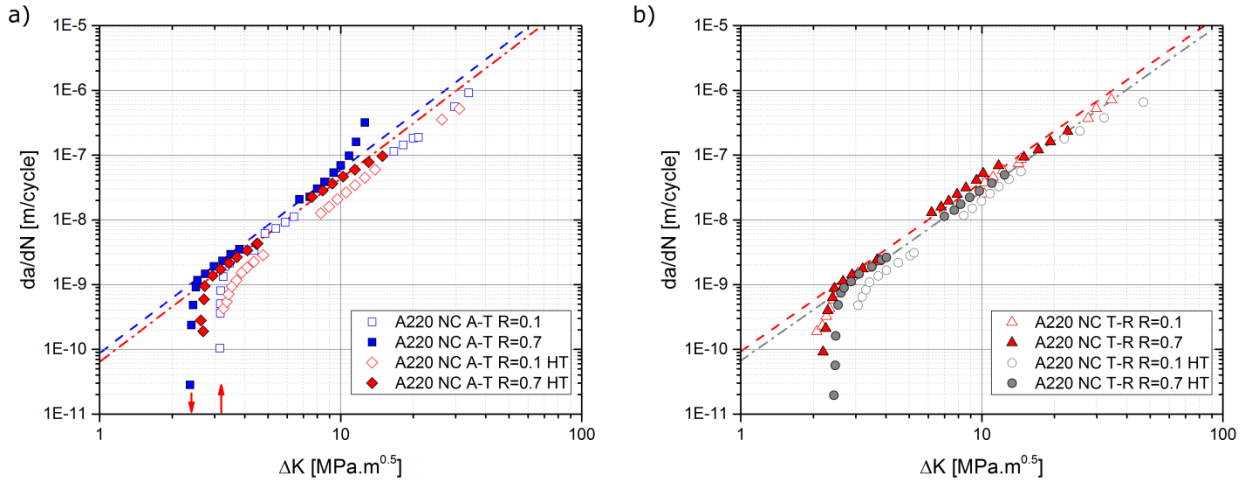

Fig. 9: FCG of as-deformed and heat treated (HT) NC A220 samples with (a) orientation A-T and (b) orientation T-R. Dashed lines are fit lines for the as-deformed NC A220; dash-dotted lines are fit lines for the heat treated NC A220.

3.4 Pearlitic steel

Discs of the pearlitic railway steels R260 and R350 with a diameter of 30 mm were deformed by HPT for ¼ and ½ turn. Thereby the applied shear strain is too small to generate saturated microstructures, however, the focus here was on microstructural states being found on the top-surface of railways under rolling-contact fatigue conditions [63,64]. From Fig. 10(a) and (b) it can be seen that the lamellae show a tendency to align parallel to the shear plane of the HPT process. The applied strain, however, was not high enough to cause a fully aligned microstructure and thus regions with lamellae oriented in other directions are still visible (e.g. in the center of Fig. 10(b)). In general, the material exhibits a lamellar spacing of a few hundred nanometer (Fig. 10(c)), which, however, can appears larger in the microsections when lamellae are cut under a flat angle. Between the cementite lamellae the ferritic phase is ultrafine-grained, as shown in Fig. 10(d).

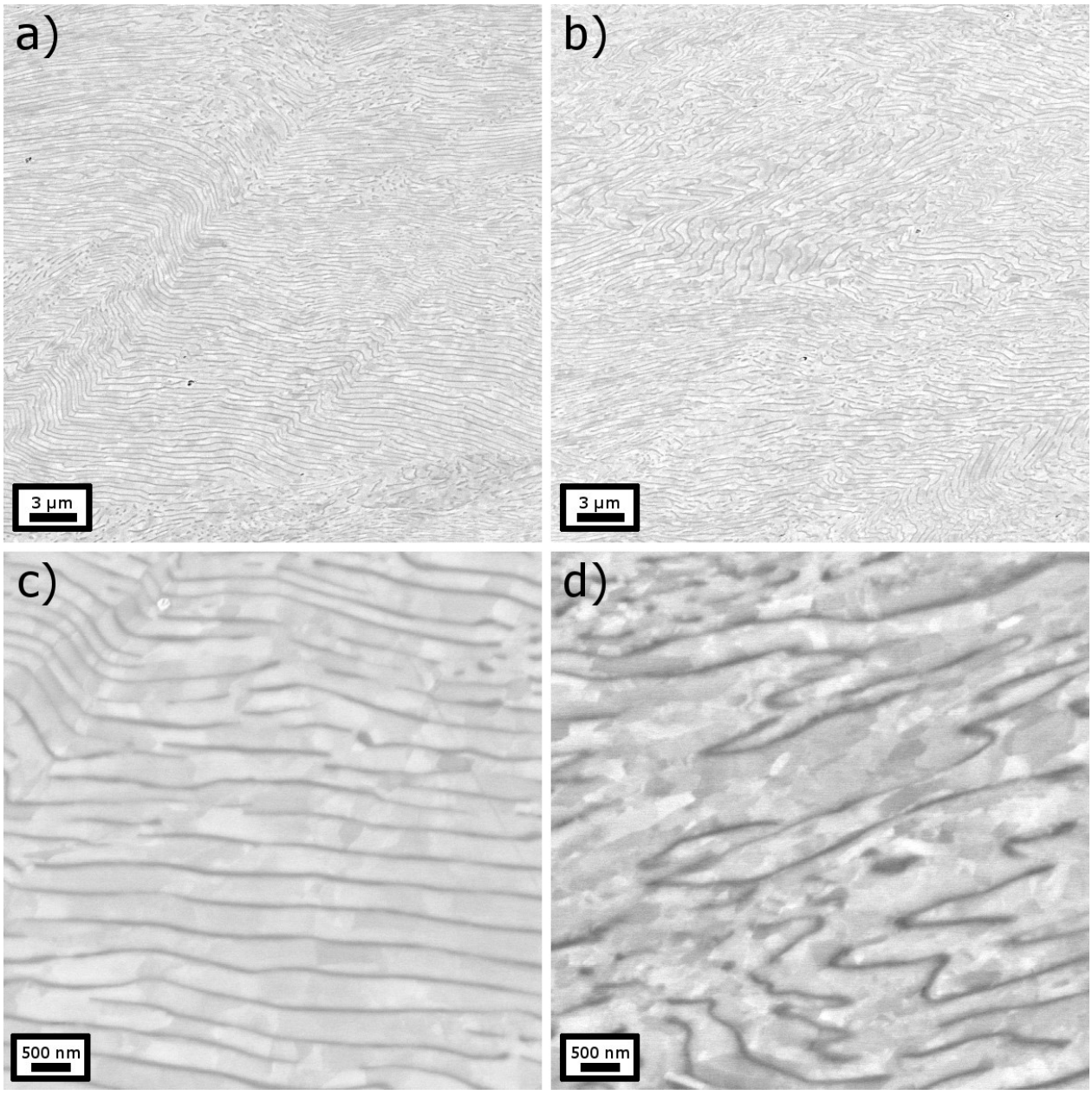

Fig. 10: SEM back-scatter electron images of an R260 sample, deformed by HPT with a total strain of ε_{VM}=1.2, viewed in radial direction. (a) and (b) show overview images of the HPT deformed material. The material in general exhibits lamellar spacings in the range of a few hundred nanometers (see figure (c)). However, when lamellae are cut under a flat angle they can appear to have larger spacings, as for example in the center of (b) and in (d). In figure (d) it can be seen, that the ferritic phase between the cementite lamellae consists of ultrafine grains.

For R260, samples with four different orientations in respect to the HPT process were prepared (A-T, T-R, T-A and T-R) from regions with an ε_{VM} of about 1.2 and tested at R=0.1 and R=0.7. Furthermore one A-T sample was taken from a position with a higher strain of about 2.3. For R350, A-T and T-R specimens with an ε_{VM} of about 1.2 were produced and tested at R=0.1. The FCG curves of the samples are shown in Fig. 11. It can be seen, that effective threshold values are only slightly affected by the sample orientation, with $\Delta K_{th,eff}$ values in the range of 2.6 to 3.6 MPa.m$^{0.5}$ and ΔK_{th} values between 3.0 to 4.4 MPa.m$^{0.5}$ for all orientations of R260 and R350. The R260 R=0.1 T-A sample exhibited the highest thresholds and in general slower FCG

compared to the other orientations (see Fig. 11(b)). Larger differences exist in the Paris regime, where the FCG rates of A-T samples were found to be up to a factor of 6 higher than for the orientation with the slowest FCG (T-A). The FCG rate of A-T specimens is about 2 times higher than for T-R in R260, and about 4 times higher in R350. Hence, a pronounced FCG anisotropy exists for these pearlitic steels, even when the imposed strain from the SPD processing is quite low. This can be linked to the tendency of the lamellae to align parallel to the shear plane of the HPT process, which is clearly visible in Fig. 10(a) and (b). Therefore, cracks in axial direction (T-A) encounter more interfaces and are deflected more frequently. In contrast, cracks parallel to the shear plane (A-T) are in many regions also parallel to the aligned ferrite-cementite interfaces and can thus follow these weak crack paths, getting deflected less often than in other orientations.

Only little difference exists between two A-T samples from regions with a nominal ε_{VM} of about 1.2 and 2.3, as presented in Fig. 11(c). However, also the mean hardness of these two samples varies only slightly, with 387 HV for ε_{VM}=1.2 and 417 HV for ε_{VM}=2.3. The small difference could be a result of an inaccuracy during the extraction of the samples from the HPT disc. Thus, the ε_{VM}=2.3 sample could have been closer to the center of the disc than planned and, therefore, actually a smaller strain was introduced than the nominal ε_{VM}=2.3.

In Fig. 11(d) the FCG curves of R350 specimens with ε_{VM}=1.2 are presented and can be compared to the dashed and dash-dotted fit lines of the corresponding R260 samples. It is obvious that R350 samples show lower FCG rates in the Paris regime compared to R260, which can be explained by the higher strength and hardness of this alloy (445 HV for R350, 380 HV for R260). As mentioned earlier, the higher strength reduces the $\Delta CTOD$ and results in lower FCG rates (see Equ. 6). This assumption is valid if the FCG is governed by blunting and re-sharpening, which seems to be likely for ductile steels, such as R260 and R350.

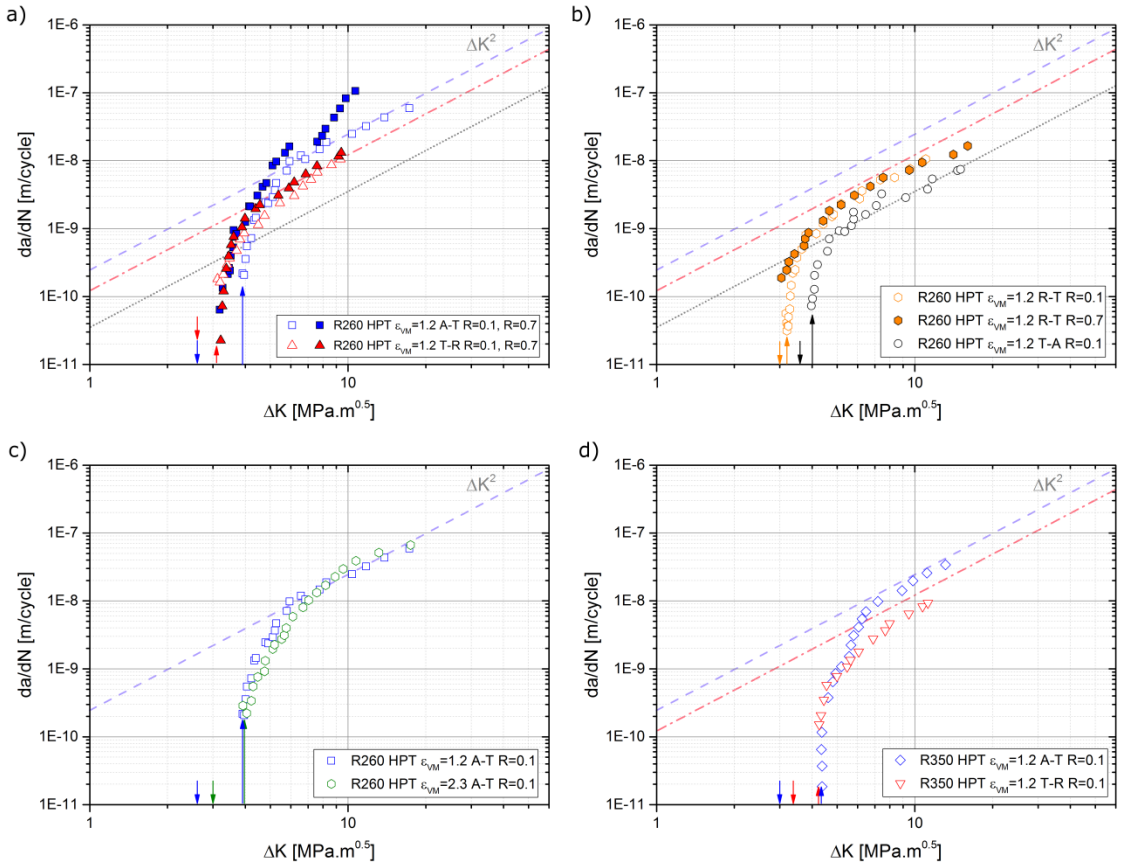

Fig. 11: FCG diagrams of HPT deformed R260 and R350. In (a) the FCG curves of R260 A-T and T-R samples, in (b) the FCG curves of R260 R-T and T-A samples are compared. In (a), (b) and (d) the introduced shear strain ε_{VM} of the samples was about 1.2, in (c) the effect of different imposed shear strains is shown with additional data from a R260 sample with ε_{VM}=2.3. (d) shows the FCG curves of R350 for A-T and T-R samples. Dashed, dash-dotted and dotted lines are fit lines for HPT deformed R260 in A-T, T-R and T-A orientation, respectively.

A comparison of FCG data from literature on R260 is given in Fig. 12. Coarse-grained R260 exhibits a ΔK_{th} value larger than 10 MPa.m$^{0.5}$, which is more than a factor of 2 higher than that of HPT deformed material. This seems to be a consequence of larger and more randomly aligned pearlite colonies [65]. However, it has also to be mentioned that load-shedding technique was used in study [65] to obtain the FCG curves, which is known to have a tendency to yield higher ΔK_{th} values. For a better comparison the fit lines of HPT deformed R260 are included in the diagram (dashed line for A-T samples, dash-dotted for T-R and dotted for T-A). In the Paris regime the FCG rate of un-deformed R260 is within the range HPT deformed R260, however, the slope of the curve appears steeper and the Paris exponent m is higher. FCG data already exists for ECAPed R260 with ε_{VM}=0.67 and ε_{VM}=2.00, for two different orientations (both R-R, however, 90° rotated around the extrusion axis) tested at R=0.5 [66]. The ΔK_{th} values of the ECAPed samples are quite similar to those of the HPT deformed samples from the present study (see marked range underneath the abscissa) and variations are small for the different orientations. Also in the Paris regime differences are small for the two orientations of ε_{VM}=0.67 specimens and therefore only the curve of the sample orientation A is redrawn in Fig. 12. This FCG curve is within the range of A-T and T-R samples of HPT deformed R260 with ε_{VM}=1.2. For ECAP deformation up to an ε_{VM} of 2.00 the orientation dependence of the FCG resistance is remarkably high, with an almost two orders of magnitude higher FCG rate for orientation B compared to A. The FCG curve of ECAPed sample A is similar to that of the HPT deformed T-A sample, and FCG curve of

ECAPed sample B is comparable that of the HPT A-T sample tested at R=0.7. This indicates that regardless of the technique, a similar FCG anisotropy arises from severe plastic deformation of materials, provided that elongated and aligned structures are generated.

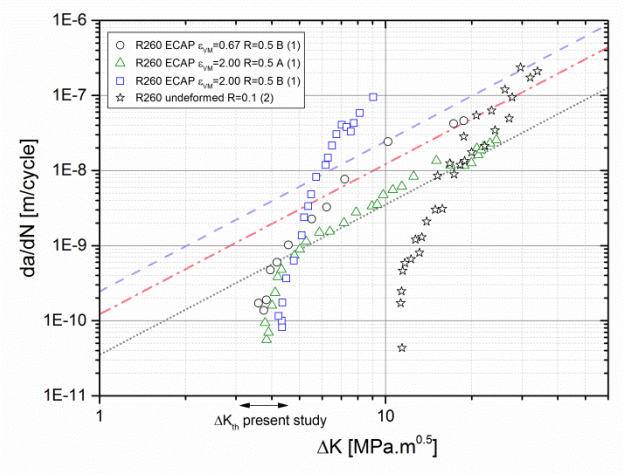

Fig. 12: Redrawn FCG curves of the pearlitic steel R260 with data from literature. Data from un-deformed R260 was taken from [65]. Data of ECAPed R260, which was deformed for 1 pass and 3 passes, is taken from [66]. The range of the ΔK_{th} values of the present study is marked under the abscissa. Fit lines of FCG curves of R260 samples of the present study are included (dashed line for A-T samples, dash-dotted for T-R and dotted for T-A).

In Fig. 13 the FCG curves of A-T and T-R samples of HPT deformed ferritic ARMCO Fe and HPT deformed R260 samples with ε_{VM}=0.67 are compared. Threshold values are similar for both materials and show the same dependency on the load ratio. Also regarding the FCG rate in the Paris regime little difference was observed for T-R specimens. For A-T specimens ARMCO Fe shows an even faster FCG rate than R260. However, it has to be kept in mind, that much larger strains were introduced in ARMCO Fe samples, than in R260 specimens and thus, grains are even more elongated and aligned than in R260.

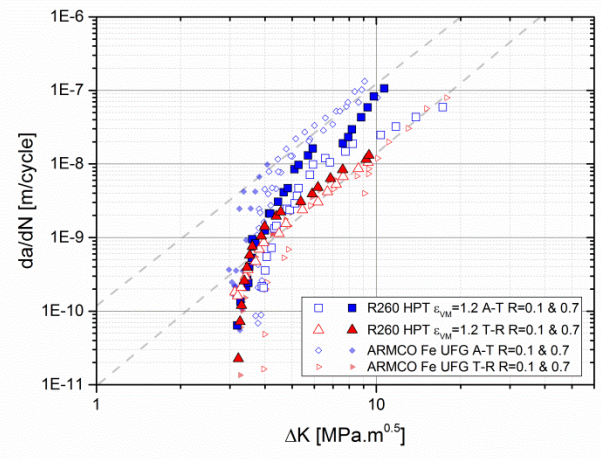

Fig. 13: Comparison of the FCG curves of ARMCO Fe with R260. Gray dashed lines are shown as guide lines for the proportionality to of (da/dN) to ΔK^3 .

3.5 Superelastic NiTi

Superelastic NiTi was chosen as an example for a material with a more complex mechanical behavior and direct industrial relevance. This material is widely used for medical applications, due to its ability to endure large cyclic strains by superelastic phase transformation [67–71]. A promising strategy to further optimize the mechanical properties of NiTi is grain refinement by SPD processing [72–77]. For the present work NiTi was deformed by ECAP at 450°C for 8 passes, using route B_C[1]. Thereby a significant grain refinement was achieved, with a mean grain size of the as-received (AR) state of about 100 µm and about 1 µm for the ECAPed material. It has to be noted, that the microstructure of the ECAPed NiTi is inhomogeneous, consisting of regions with grains as small as 100 nm and coarser-grained regions with grains up to 5 µm. The grain refinement resulted in an increase in hardness from 240 HV in the as-received state to 300 HV for the ECAPed NiTi. A more detailed description of the microstructure and the mechanical properties obtained from tensile tests and fracture toughness experiments can be found in publication D. In the following the discussion is limited to the FCG behavior of AR and ECAPed NiTi.

The FCG curves of AR NiTi in Fig. 14(a) show that for R=0.7 ΔK_{th} and $\Delta K_{th,eff}$ coincide at about 0.9 MPa.m$^{0.5}$, which is also close to the $\Delta K_{th,eff}$ at R=0.1 (1.1 MPa.m$^{0.5}$) and can be seen as the intrinsic FCG threshold. Due to contributions from crack closure AR NiTi exhibits cyclic R-curve behavior and thus at low mean stresses (R=0.1) $\Delta K_{th,eff}$ is lower than ΔK_{th} (1.6 MPa.m$^{0.5}$). In the Paris region the pronounced effect of crack closure is visible by a more than a magnitude higher FCG rate for samples tested at R=0.7 compared to R=0.1. Regarding the near-threshold region only small differences exist between AR and ECAPed NiTi.

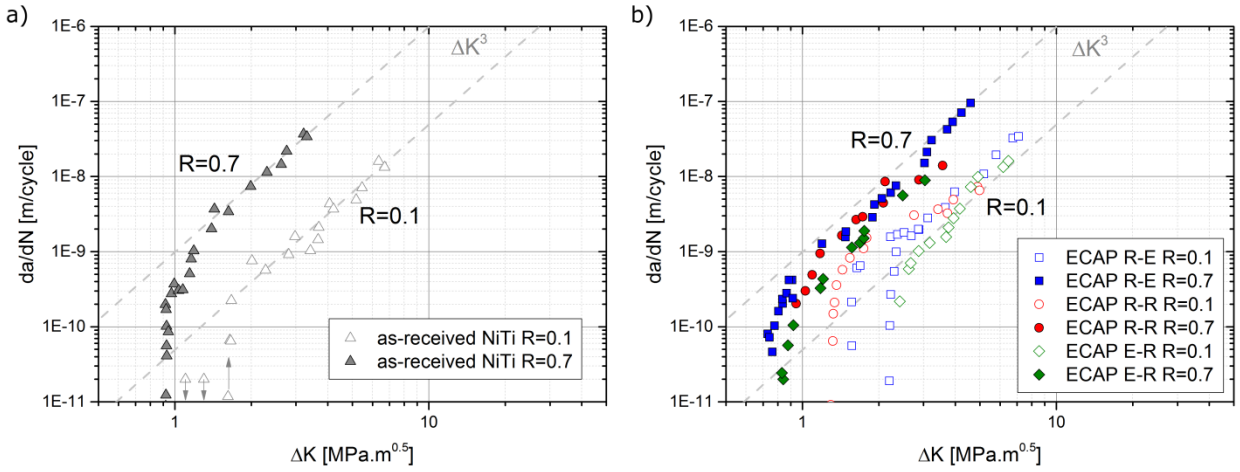

Fig. 14: FCG diagram of (a) as-received and (b) ECAPed NiTi. Fit lines for the Paris region of the as-received NiTi are shown as gray dashed lines in (a) and are also included in the FCG diagram of ECAPed NiTi (b) for comparison.

Although ECAP processing of NiTi resulted in a severe grain refinement, the fracture mode during FCG of ECAPed NiTi remained transgranular as it was also observed in AR NiTi. Furthermore, the FCG curves of AR and ECAPed NiTi in Fig. 14(a) and (b) show that only small differences between the two material states exist. For AR and ECAPed NiTi, ΔK_{th} and $\Delta K_{th,eff}$ values coincide at about 0.8 to 1 MPa.m$^{0.5}$ at R=0.7, which is also close to the range of $\Delta K_{th,eff}$ values at R=0.1 (1.0 to 1.1 MPa.m$^{0.5}$) and can be seen as the intrinsic FCG threshold. Due to contributions from crack closure NiTi exhibits cyclic R-curve behavior in its AR and

[1] For ECAP route B_C the billet is rotated 90° after each cycle.

ECAPed state and thus at low mean stresses (R=0.1) $\Delta K_{th,eff}$ is significantly lower than ΔK_{th} (1.6 MPa.m$^{0.5}$ for AR NiTi and 1.3 to 2.4 MPa.m$^{0.5}$ for ECAPed NiTi). In the Paris region the pronounced effect of crack closure is visible by a higher FCG rate for samples tested at R=0.7 compared to R=0.1. The difference is larger than one order of magnitude for AR NiTi and slightly reduced for ECAPed NiTi. Compared to AR NiTi, the finer-grained ECAPed NiTi shows lower FCG rates at R=0.7 but higher rates at R=0.1. Significant scatter is observed for ECAPed NiTi, which is likely to be an effect of the microstructural inhomogeneity of the material. For ECAPed NiTi three sample orientations were tested; however, differences in their FCG curves lie within the scatter. Thus, it can be concluded that there is no pronounced FCG anisotropy in ECAPed NiTi. From the above mentioned observations the following aspects can be summarized:

- Despite ECAP deformation, the average grain size is still too large to provoke a transition from transgranular to intergranular fracture.
- Although the grain size varies remarkably for AR and ECAPed NiTi, hardly any difference exists in their $\Delta K_{th,eff}$ values. This indicates that the stress intensity factor range necessary for the first crack extension is an intrinsic material property and not significantly influenced by the microstructure.
- At high mean stresses (R=0.7) ECAP processing leads to a reduction of the FCG rate, as the fracture mode is not changed but the strength of the material is increased. When FCG is assumed to be controlled by plastic deformation, this leads to a smaller $\Delta CTOD$ and therefore to slower fatigue crack propagation, as it has already been discussed in the previous sections. This assumption seems to be appropriate for NiTi and can explain the differences in the FCG rates.
- At lower mean stresses (R=0.1) significant roughness and plasticity induced crack closure is active in the AR NiTi. Due to the grain refinement crack closure contributions are reduced for ECAPed NiTi and thus a tendency to higher FCG rates is observed for ECAPed samples compared to AR NiTi.
- No clear FCG anisotropy was observed for ECAPed NiTi, as a result of more equiaxed grains. Grains are less elongated than in UFG metals produced by HPT, since the shear plane of ECAP route B_C changes for each pass and the introduced shear strain after 8 passes is still small compared to HPT processed materials mentioned before.

3.6 Fracture surface analyses

Fig. 15 shows exemplary SEM images of the fracture surfaces of all tested materials. As mentioned in the discussion of the individual materials, strong grain refinement often results in the change from transgranular to intergranular fracture. Transgranular fracture is visible on the fracture surfaces of MC ARMCO Fe, MC A220 and MC NiTi, and is characterized by small ledges and other asperities. For MC Ni also areas with intergranular fracture can be observed, where the contours of the grains are clearly visible (see high magnification image of MC Ni). The fracture surfaces of UFG ARMCO Fe, UFG Ni and NC A220 exhibit almost exclusively intergranular fracture, and thus the contours of the small grains of these microstructures can be seen in the high magnification images. In contrast, the facture surfaces of R260 and NiTi are dominated by transgranular fracture also in their SPD state.

Fig. 15: Exemplary SEM images of the fracture surfaces of the tested MC, UFG and NC materials. Each row shows images of different materials or material states. Images in one column are shown at the same magnification.

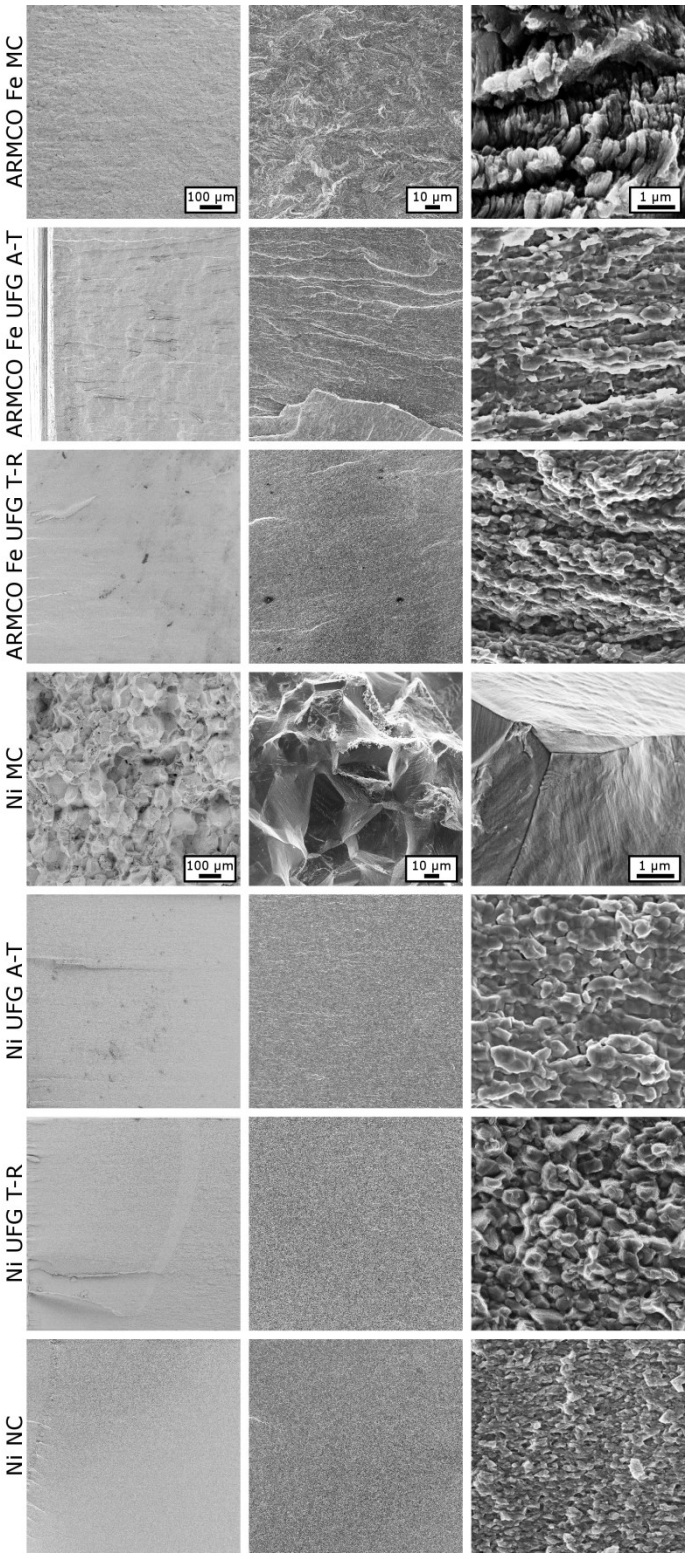

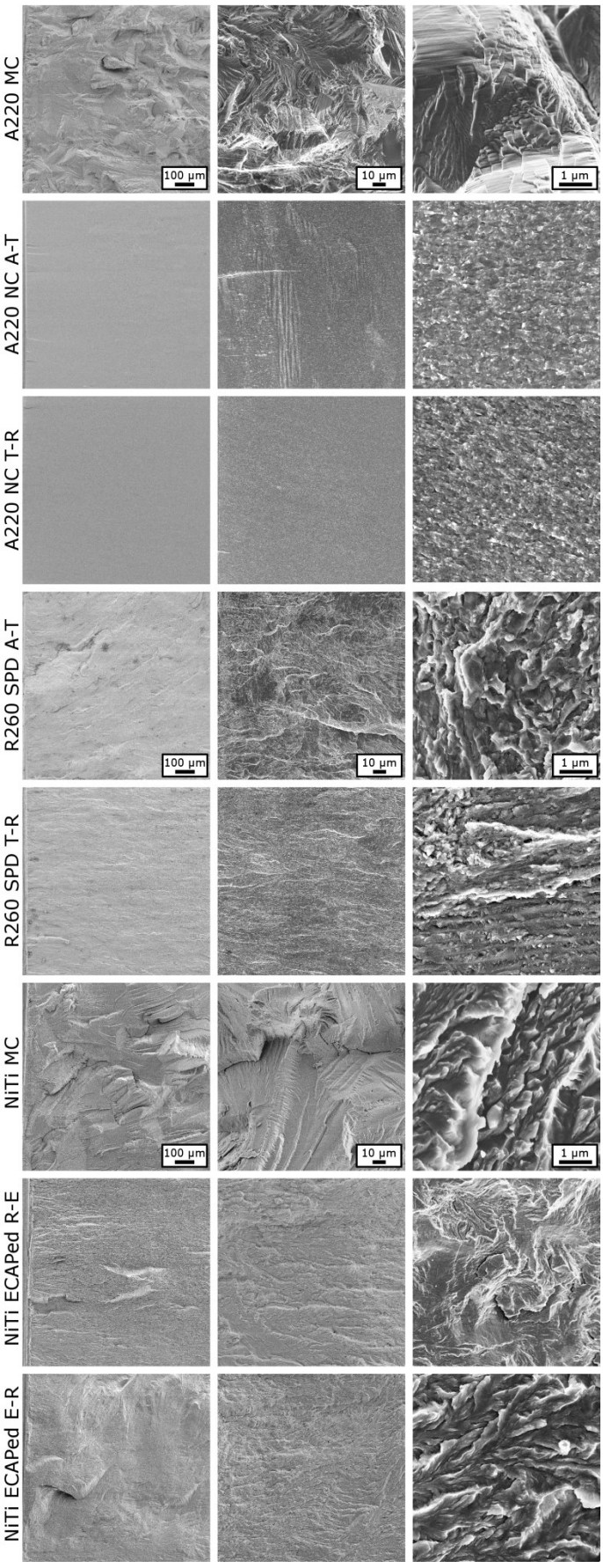
A220 MC
A220 NC A-T
A220 NC T-R
R260 SPD A-T
R260 SPD T-R
NiTi MC
NiTi ECAPed R-E
NiTi ECAPed E-R
100 µm
10 µm
1 µm

3.7 Comparison FCG diagrams

In the following, the FCG diagrams of all tested materials are shown together for an easier comparison. More details can be found in the results sections of the individual materials.

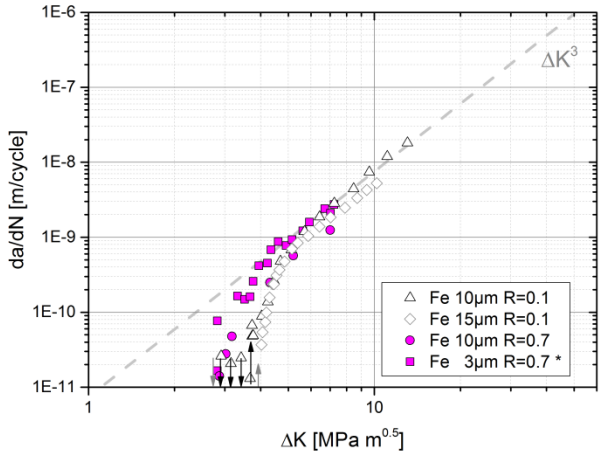

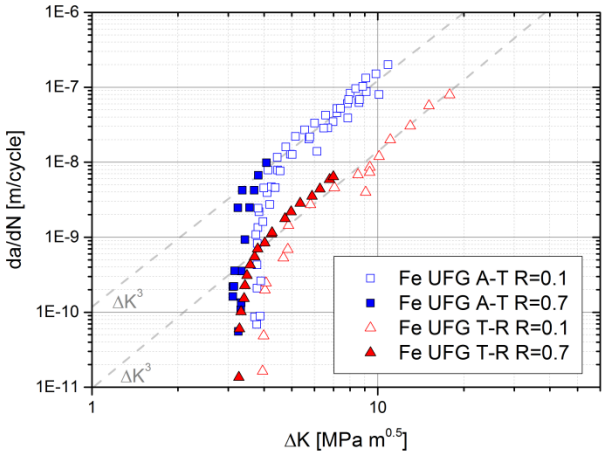

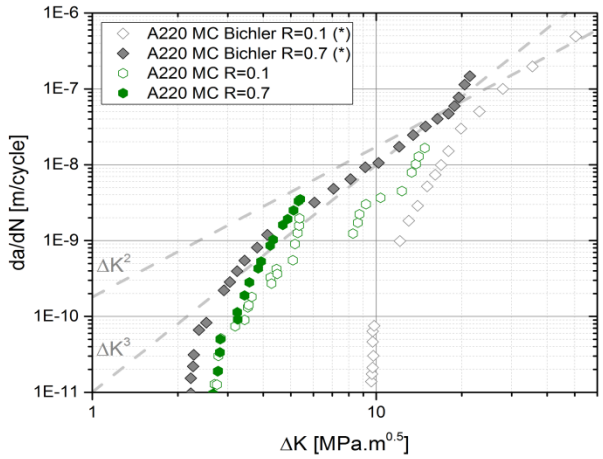

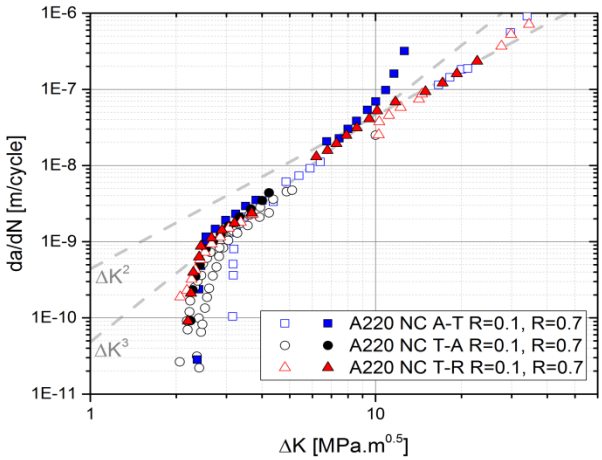

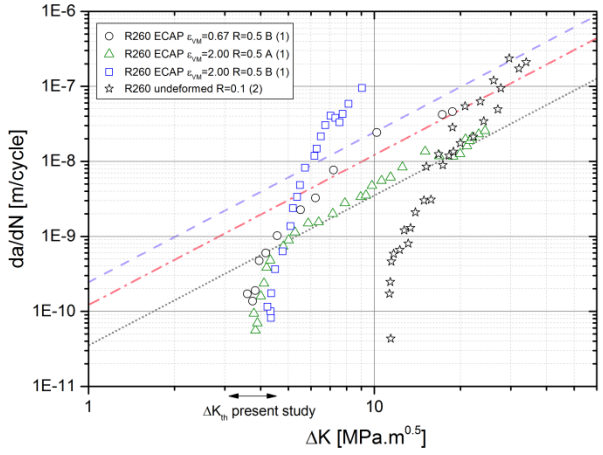

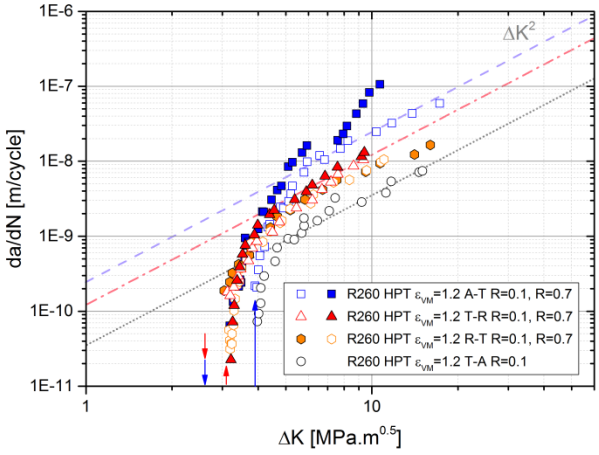

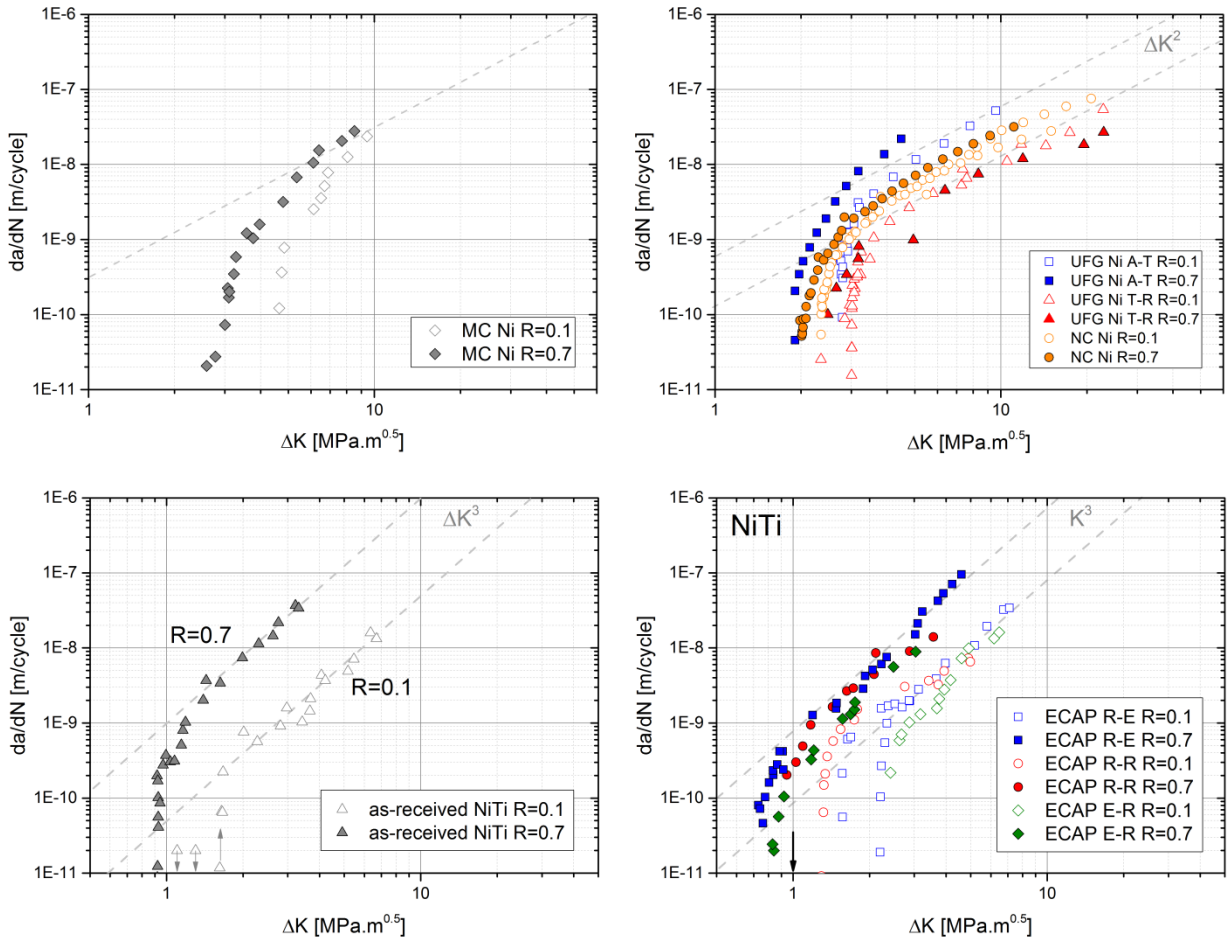

Fig. 16: Overview of the FCG diagrams of all tested materials. The FCG curves are discussed in more detail in the individual results sections.

4 Discussion

In the following sections, the results of the different materials are compared and the effect of grain refinement on the FCG properties is discussed. The results of the individual materials and microstructures are described in more detail in sections 3.1 to 3.5.

4.1 Effective and long crack threshold stress intensity factor range

As mentioned in the introduction, it is important to differentiate between the effective threshold stress intensity factor range $\Delta K_{th,eff}$ and the long crack threshold stress intensity factor range ΔK_{th}. $\Delta K_{th,eff}$ is an intrinsic material property and depends for microcrystalline metals mainly on the Young's modulus, E, and the length of the burgers vector, b, as described by Equ. 5. In Fig. 17(a) the investigated MC materials are plotted by their product of the Young's modulus and the square root of the burgers vector against the determined $\Delta K_{th,eff}$. The linear relationship confirms that $\Delta K_{th,eff}$ of MC metals is mainly influenced by lattice parameters; the microstructure plays only a minor role.

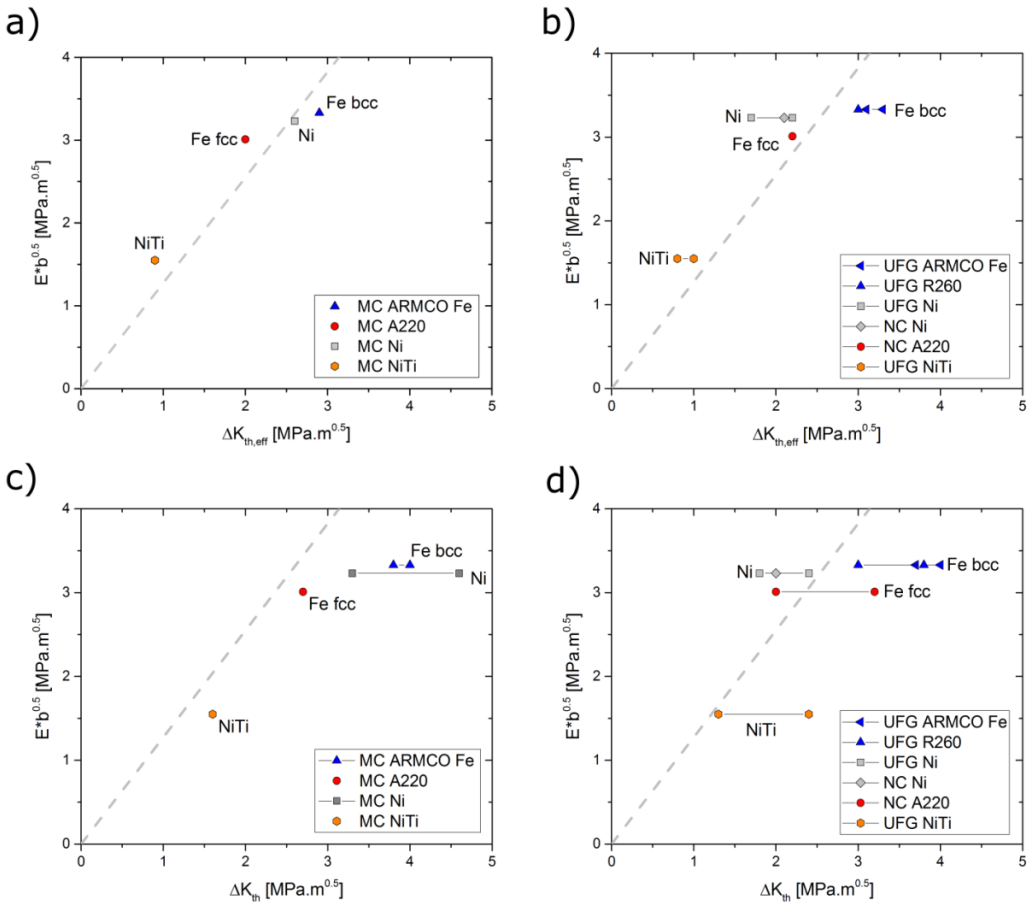

Fig. 17: Comparison of the threshold stress intensity factor ranges of the investigated MC, UFG and NC metals. In diagrams (a) and (b) the effective threshold stress intensity factor ranges $\Delta K_{th,eff}$ are compared, in (c) and (d) the long-crack threshold stress intensity factor ranges ΔK_{th} measured at R=0.1 are shown. The materials are listed by the product of their Young's modulus E and the square root of length of their Burgers vector b.

For SPD metals, however, larger deviations from the linear behavior are observed (Fig. 17(b)). This can be explained when the size of the cyclic plastic zone, r_{CPZ}, is compared to the grain size, as shown in Table 2. For MC metals, the cyclic plastic zone (CPZ) is significantly smaller than the grain size (ratio of (grain size)/(r_{CPZ}) significantly larger than 1 in Table 2) and thus, dislocations which are emitted from the crack tip move in general in a continuum (single crystal). In contrast to that, the grain size of UFG and NC metals is in the range of the CPZ size (ratio of (grain size)/(r_{CPZ}) smaller or close to 1 in Table 2) and therefore dislocations interact with grain boundaries after they are emitted from the crack tip. Hence, the $\Delta K_{th,eff}$ of very fine-grained materials is not only influenced by continuum mechanics parameters but also by the grain size and the grain boundary type.

Table 2: Comparison of the relations between the CPZ size and the grain size for all tested materials at $\Delta K_{th,eff}$ and ΔK=10 MPa.m$^{0.5}$. The strength was estimated from hardness measurements with the Tabor rule ($\sigma_y \approx 3 * H * 1\ MPa/HV$) [78]. The CPZ sizes, r_{CPZ}, were calculated for plane strain conditions according to [79].

		ARMCO Fe		A220			R260		R350	Ni			NiTi	
Production Method		HPT	HPT	AR	HPT	HPT	HPT	HPT	HPT	AR	HPT	ED	AR	ECAP B_C
ε_{VM}	[-]	14-100	14-100	-	14-100	14-100	1.2	2.3	1.2	-	14-100	-	-	6.5
Heat Treatment		650°C 1h	-	900°C 30min	-	550°C 30min	-	-	-	-	-	-	-	450°C
Mean Hardness	[HV0.5]	105	410	160	502	597	380	420	445	120	280	470	240	300
Mean grain size	[nm]	15000	310	75000	50	50	200	200	200	50000	410	30	100000	1000
r_{CPZ} @ $\Delta K_{th,eff}$	[nm]	1949	168	461	47	48	138	150	134	1384	109	53	41	21
GS / r_{CPZ} @ $\Delta K_{th,eff}$	[-]	**7.70**	**1.84**	**162.86**	**1.07**	**1.05**	**1.45**	**1.33**	**1.49**	**36.14**	**3.77**	**0.56**	**2412.74**	**47.71**
r_{CPZ} @ ΔK=10MPa.m$^{0.5}$	[nm]	26733	1753	11513	1170	827	2041	1671	1488	20467	3759	1334	5117	3275
GS / r_{CPZ} @ $\Delta K_{th,eff}$	[-]	**0.56**	**0.18**	**6.51**	**0.04**	**0.06**	**0.10**	**0.12**	**0.13**	**2.44**	**0.11**	**0.02**	**19.54**	**0.31**

In the diagrams of Fig. 17(c) and (d) the long crack threshold stress intensity factor ranges ΔK_{th} measured for R=0.1 are plotted for MC and SPD metals. It is obvious from the large deviations from the guideline that the afore-mentioned approach is not appropriate to estimate long crack ΔK_{th} values, since they are strongly influenced by crack closure. A tendency to lower ΔK_{th} values was observed for UFG and NC materials, which seems to be a consequence of reduced crack closure contributions; this will be discussed in section 4.3.

4.2 FCG rate at high mean stresses

FCG experiments at R=0.7 can be used to assess the intrinsic FCG resistance, since a high mean stress of the cyclic load often results in a nearly complete reduction of crack closure contributions for MC and finer-grained metals (UFG and NC). As already described in the results sections, there exist many indications that FCG of the investigated materials is mainly governed by plastic deformation. Thus, the FCG rate is predicted to be inversely proportional to the strength of the material (see Equ. 6). As the strength of a material increases with grain refinement, the FCG rate is supposed to decrease. However, if the stage II FCG rates of microcrystalline ARMCO Fe, A220 and Ni are compared with their UFG and NC counterparts, a tendency to higher FCG rates for UFG and NC materials is found. It has to be mentioned, that the grain refinement of these materials is not only accompanied by an increase in strength, but also by a change in the fracture mode during FCG, from transgranular fracture in the MC state to intergranular fracture in the SPD state. It seems that the FCG resistance for crack growth along grain boundaries is lower and therefore FCG rates are increased by the large change in grain size, although the increase in strength counteracts this trend. In fact, when the fracture mode remains unchanged by the SPD processing, as for example in the case of NiTi, the reduced grain size and increased strength leads to a decrease in the FCG rate, which can be well explained by the FCG model based on blunting and re-sharpening (see Equ. 6). The comparison of as-deformed NC A220 with heat treated NC A220 further confirms that an increase in strength is responsible for the reduced FCG rate. The heat treatment of NC A220 did not lead to a change in grain size but resulted in an increased

strength and provoked a reduced FCG rate. The simultaneous decrease in defect density had no detrimental effect either. The same trend was found for the FCG of the HPT deformed pearlitic steels R260 and R350, where higher FCG rates were observed for R260, which has a lower strength than R350. This indicates that a higher strength leads to a higher intrinsic FCG resistance, regardless of the type of the strengthening mechanism, as long as there is no transition in the fracture mode.

However, also the hardening behavior of a material influences the FCG rate. Cyclic hardening reduces the $\Delta CTOD$ and therefore decreases the crack advance per cycle (and thus the FCG rate), which is taken into account by the factor d_n in Equ. 6. The coefficient d_n depends on the hardening behavior and lies in the range of about 0.1 for strongly hardening materials to 0.68 for non-hardening materials [80]. Thus, materials which exhibit significant cyclic hardening, such as many MC metals, are expected to show a tendency to lower FCG rates, compared to less hardening materials, as for example SPD deformed UFG and NC metals. This can be a reason for increased FCG rates of SPD processed metals, compared to un-deformed MC materials, which is frequently observed in experiments.

4.3 Crack closure contributions

In order to understand the effect of grain refinement on the FCG behavior under loading conditions with lower mean stress, crack closure contributions have to be considered. It is commonly reported that UFG and NC materials exhibit less pronounced crack closure than their coarser-grained counterparts. This reduction of crack closure contributions due to severe grain refinement is also observed in the experiments of the present thesis. Especially for UFG Fe, UFG Ni and NC austenitic steel A220 the ΔK_{th} value is close to $\Delta K_{th,eff}$ and the FCG rates in the Paris regime are quite similar for R=0.1 and R=0.7. This leads to the conclusion, that crack closure mechanisms, such as RICC, OICC and PICC, which typically reduce the FCG rates in ductile metals (see section 2.2.1), are less active in these very fine-grained metals. The diminishment of crack closure with grain refinement is extensively discussed in the publications B and C in the annex. RICC crack closure is reduced due to the more homogeneous plastic deformation in NC and UFG metals, which in turn decreases the mode II displacement of the crack faces. Therefore, there is less mismatch between the two halves of the sample and hence, pre-mature contact of the crack faces is reduced. Furthermore, the fracture surfaces of UFG and NC samples are much smoother than the MC samples with smaller asperities, which means fewer contact points especially at larger crack tip opening displacements. Contributions of OICC are expected to be small, as no oxide debris was found on the fracture surfaces of all studied materials. Reduced contribution from PICC can be explained by the instability of the microstructure. Grain coarsening around the crack tip leads to a larger size of the cyclic plastic zone and therefore to a reduction of the stored dislocations in the wake of the crack. As stored dislocations from the monotonic deformation are responsible for the plastic wedge and thus for PICC, their reduction results in a weakening of PICC. More details can be found in publications B. To summarize, diminishing crack closure contributions in UFG and NC metals seem to be the reason, that ΔK_{th} values are reduced and approach $\Delta K_{th,eff}$. Furthermore, the very fine-grained materials exhibit a trend to higher FCG rates at low means stresses, compared to MC metals, due to the reduction of RICC and PICC.

4.4 Orientation dependence of the FCG resistance

The FCG resistance of UFG and NC materials produced by SPD can be significantly influenced by the orientation of the crack in respect to the foregoing deformation process. In general, there is a trend to lower FCG resistance for cracks growing parallel to the shear plane of the SPD process (A-T orientation in HPT

deformed samples), than parallel to it (T-R orientation). This is observed e.g. in HPT processed UFG ARMCO Fe, UFG R260 and UFG Ni. In some materials crystallographic texture is found to be the reason for anisotropic mechanical properties. This, however, is unlikely for the present SPD processed materials, since only a weak shear textures evolve, as reported in literature for interstitial free steel [23,81,82] and observed from X-ray diffraction experiments on Fe. It seems more reasonable that the FCG anisotropy of SPD processed metals is a result of the grain geometry. Many SPD methods, such as HPT and ECAP, lead to a microstructure consisting of grains elongated parallel to the shear direction of the deformation process. As cracks were found to grow along grain boundaries, it makes a difference if the crack is oriented parallel to the shear plane and hence parallel to the elongation direction of the grains (A-T samples) or perpendicular to it (T-R samples). Cracks parallel to the elongation direction can follow elongated grain boundaries, without large deviations from the straight crack path. This is in contrast to the situation for cracks perpendicular to longer axis of the elongated grains, where the cracks are deflected more frequently and to larger angles from its straight path. A schematic of this behavior is given in Fig. C-10 of publication C. The result is a more tortuous crack path and rougher fracture surface for T-R samples, compared to A-T specimens. Furthermore, the frequent crack deflections act as a geometric shielding mechanism and reduce the local crack driving force. Thus, FCG rates are lower for cracks perpendicular to the grain elongation direction, than parallel to it. The orientation of the crack seems to also influence the crack tip opening angle and the crack tip blunting angle, which results in an orientation dependent overall FCG rate.

In contrast to UFG ARMCO Fe and UFG Ni, NC A220 showed almost no anisotropic FCG behavior, although the same strain was applied by HPT. Therefore, it can be concluded that the applied strain is not crucial for the appearance of anisotropic FCG behavior. In addition, HPT processing does not necessarily lead to orientation dependent mechanical properties. For example, it is known that HPT deformed metals provide only weak orientational differences in yield strength. In the case of A220, grains are also slightly elongated; however, their elongation is weaker and they are a magnitude smaller than in UFG Fe and Ni. Therefore, deflections of the crack in the case of T-R specimens are also smaller and the effect of the geometric shielding diminishes.

In conclusion, it was found that the anisotropy of the FCG rate in SPD processed materials is predominantly a result of the grain geometry. Repeated deflections of the cracks, which occur more frequently for cracks perpendicular to the longer axis of the grains, can effectively increase the FCG resistance. However, this advantageous effect seems to diminish for NC materials, as the deflections get smaller due to the further reduced grain sizes and less pronounced grain elongation.

5 Conclusions

In the present thesis the fatigue crack growth of severely plastically deformed metals was comprehensively studied and compared to microcrystalline materials. It was found that the effective threshold stress intensity factor range $\Delta K_{th,eff}$ is only slightly affected by the grain size reduction of the SPD processing. However, the threshold of the long crack stress intensity factor range ΔK_{th} as well as the FCG resistance at low mean stresses is generally lower for UFG and NC materials, compared to their coarser-grained counterparts. This is a result of reduced contributions from plasticity and roughness induced crack closure due to microstructural instability, a more homogeneous deformation and less crack path tortuosity of the very fine-grained metals. Nevertheless, the intrinsic FCG resistance, which is important in conditions where crack closure plays a minor role (high mean stresses), was found to be increased by the grain refinement as a result of the increase in

strength. This can be well explained by a FCG model based on plastic deformation, which further confirms the assumption that the FCG of SPD processed metals is dominated by a blunting and re-sharpening mechanism. However, when the grain refinement is accompanied by a change in the fracture mode from transgranular to intergranular fracture, grain boundaries act as weak crack paths and counteract the beneficial effect of the increase in strength. Also the reduced cyclic hardening of SPD processed UFG and NC materials can lead to higher FCG rates. Furthermore, UFG and NC materials show an orientation dependent FCG behavior, when the deformation process yields elongated grains. Cracks oriented parallel to the longer axis of the grains were found to grow up to a magnitude faster than cracks perpendicular to the elongation direction. From this behavior it can be concluded that the frequent deflections of the perpendicular cracks act as a geometrical shielding mechanism and enhance the FCG resistance. However, this tendency diminishes for even finer-grained metals (e.g. NC A220), as deflections get smaller due to the small grain size and the more equiaxed grains.

In this work the fundamental relationships between microstructure and the resulting FCG behavior were elaborated. With the newly gained knowledge it is possible to distinguish between extrinsic and intrinsic effects of grain refinement on the FCG. The deterioration of the FCG behavior with grain refinement, which is often reported in literature, was found to be associated with the reduction of crack closure contributions and the change from transgranular to intergranular fracture. However, the general increase in strength induced by SPD processing is beneficial and results in an increase of the intrinsic FCG resistance. Furthermore, elongated grains, which often result from SPD processing, lead to geometric shielding and thus, to a reduced FCG rate for cracks perpendicular to the elongation direction. These results help to find strategies to improve the FCG resistance of UFG and NC metals, which, otherwise, can be a severe limitation for their application as engineering materials. Suggestions for future work and recommendations to improve the FCG behavior are shortly summarized in the following:

- It is recommended to use the load rising method for the determination of the threshold stress intensity factor range. This testing procedure yields conservative effective ΔK_{th} values, independent of the contributions of crack closure, which is not necessarily the case for the load shedding method.
- Grain refinement by SPD can lead to an increase in the intrinsic FCG resistance due to the increased strength, as long as the fracture mode is not changed from transgranular to intergranular. Therefore it can be favorably for the FCG behavior to keep the grain size above the transition grain size.
- The stabilization of the microstructure could help to avoid the reduction of the beneficial contribution of plasticity induced crack closure.
- A weaker grain elongation may lead to more balanced and less orientation dependent mechanical properties, including the FCG behavior.
- However, the FCG anisotropy can also be intentionally exploited by using SPD materials in an orientation, which is advantageous for the designated application. For that, the elongated grains should be aligned perpendicular to the plane of typically evolving cracks.

6 References

[1] E.O. Hall, The deformation and ageing of mild steel: III Discussion of results, Proc. Phys. Soc. Sect. B. 64 (1951) 747.

[2] H. Gleiter, Nanocrystalline materials, Prog. Mater. Sci. 33 (1989) 223–315.

[3] K.S. Kumar, H. Van Swygenhoven, S. Suresh, Mechanical behavior of nanocrystalline metals and alloys, Acta Mater. 51 (2003) 5743–5774.

[4] R.Z. Valiev, R.K. Islamgaliev, I.V. Alexandrov, Bulk nanostructured materials from severe plastic deformation, Prog. Mater. Sci. 45 (2000) 103–189.

[5] A. Zhilyaev, T. Langdon, Using high-pressure torsion for metal processing: Fundamentals and applications, Prog. Mater. Sci. 53 (2008) 893–979.

[6] C. Koch, Optimization of strength and ductility in nanocrystalline and ultrafine grained metals, Scr. Mater. 49 (2003) 657–662.

[7] Y. Wang, M. Chen, F. Zhou, E. Ma, High tensile ductility in a nanostructured metal, Nature. 419 (2002) 912–915.

[8] I. Sabirov, Y. Estrin, M.R. Barnett, I. Timokhina, P.D. Hodgson, Tensile deformation of an ultrafine-grained aluminium alloy: Micro shear banding and grain boundary sliding, Acta Mater. 56 (2008) 2223–2230.

[9] M. Faleschini, H. Kreuzer, D. Kiener, R. Pippan, Fracture toughness investigations of tungsten alloys and SPD tungsten alloys, J. Nucl. Mater. 367–370 (2007) 800–805.

[10] A. Hohenwarter, R. Pippan, Fracture toughness evaluation of ultrafine-grained nickel, Scr. Mater. 64 (2011) 982–985.

[11] A. Hohenwarter, R. Pippan, Anisotropic fracture behavior of ultrafine-grained iron, Mater. Sci. Eng. A. 527 (2010) 2649–2656.

[12] A. Hohenwarter, R. Pippan, Fracture of ECAP-deformed iron and the role of extrinsic toughening mechanisms, Acta Mater. 61 (2013) 2973–2983.

[13] A. Hohenwarter, R. Pippan, Fracture and fracture toughness of nanopolycrystalline metals produced by severe plastic deformation, Philos. Trans. A. Math. Phys. Eng. Sci. 373 (2015) 20140366-.

[14] T. Hanlon, Y.-N. Kwon, S. Suresh, Grain size effects on the fatigue response of nanocrystalline metals, Scr. Mater. 49 (2003) 675–680.

[15] T. Hanlon, E. Tabachnikova, S. Suresh, Fatigue behavior of nanocrystalline metals and alloys, Int. J. Fatigue. 27 (2005) 1147–1158.

[16] A. Vinogradov, Fatigue limit and crack growth in ultra-fine grain metals produced by severe plastic deformation, J. Mater. Sci. 42 (2006) 1797–1808.

[17] L. Collini, Fatigue crack growth resistance of ECAPed ultrafine-grained copper, Eng. Fract. Mech. 77 (2010) 1001–1011.

[18] L. Collini, Copper Alloys - Early Applications and Current Performance - Enhancing Processes, InTech, 2012.

[19] H.A. Padilla, B.L. Boyce, A Review of Fatigue Behavior in Nanocrystalline Metals, Exp. Mech. 50 (2009) 5–23.

[20] A. Vinogradov, T. Kawaguchi, Y. Kaneko, S. Hashimoto, Fatigue Crack Growth and Related Microstructure Evolution in Ultrafine Grain Copper Processed by ECAP, Mater. Trans. 53 (2012) 101–108.

[21] P. Hübner, R. Kiessling, H. Biermann, A. Vinogradov, Fracture behaviour of ultrafine-grained materials under static and cyclic loading, Int. J. Mater. Res. 97 (2006) 1566–1570.

[22] H.-K. Kim, M.-I. Choi, C.-S. Chung, D.H. Shin, Fatigue properties of ultrafine grained low carbon steel produced by equal channel angular pressing, Mater. Sci. Eng. A. 340 (2003) 243–250.

[23] T. Niendorf, F. Rubitschek, H.J. Maier, D. Canadinc, I. Karaman, On the fatigue crack growth–microstructure relationship in ultrafine-grained interstitial-free steel, J. Mater. Sci. 45 (2010) 4813–4821.

[24] U. Erb, A.M. El-Sherik, G. Palumbo, K.T. Aust, Synthesis, structure and properties of electroplated nanocrystalline materials, Nanostructured Mater. 2 (1993) 383–390.

[25] C. Suryanarayana, C.C. Koch, Nanocrystalline materials - Current research and future directions, Hyperfine Interact. 130 (2000) 5–44.
[26] C. Suryanarayana, Mechanical alloying and milling, Prog. Mater. Sci. 46 (2001) 1–184.
[27] Y. Estrin, A. Vinogradov, Extreme grain refinement by severe plastic deformation: A wealth of challenging science, Acta Mater. 61 (2013) 782–817.
[28] A. Hohenwarter, A. Bachmaier, B. Gludovatz, S. Scheriau, R. Pippan, Technical parameters affecting grain refinement by high pressure torsion, Int. J. Mater. Res. 100 (2009) 1653–1661.
[29] M. Furukawa, Y. Iwahashi, Z. Horita, M. Nemoto, T.G. Langdon, The shearing characteristics associated with equal-channel angular pressing, Mater. Sci. Eng. A. 257 (1998) 328–332.
[30] R. Pippan, S. Scheriau, A. Taylor, M. Hafok, A. Hohenwarter, A. Bachmaier, Saturation of Fragmentation During Severe Plastic Deformation, Annu. Rev. Mater. Res. 40 (2010) 319–343.
[31] K. Lu, N. Hansen, Structural refinement and deformation mechanisms in nanostructured metals, Scr. Mater. 60 (2009) 1033–1038.
[32] T. Leitner, A. Hohenwarter, R. Pippan, Revisiting fatigue crack growth in various grain size regimes of Ni, Mater. Sci. Eng. A. 646 (2015) 294–305.
[33] G.B. Rathmayr, A. Hohenwarter, R. Pippan, Influence of grain shape and orientation on the mechanical properties of high pressure torsion deformed nickel, Mater. Sci. Eng. A. 560 (2013) 224–231.
[34] A. Hohenwarter, R. Pippan, A comprehensive study on the damage tolerance of ultrafine-grained copper, Mater. Sci. Eng. A. 540 (2012) 89–96.
[35] A. Hohenwarter, A. Taylor, R. Stock, R. Pippan, Effect of Large Shear Deformations on the Fracture Behavior of a Fully Pearlitic Steel, Metall. Mater. Trans. A. 42 (2010) 1609–1618.
[36] Y. Yang, B. Imasogie, G.J. Fan, P.K. Liaw, W.O. Soboyejo, Fatigue and Fracture of a Bulk Nanocrystalline NiFe Alloy, Metall. Mater. Trans. A. 39 (2008) 1145–1156.
[37] A. Vinogradov, K. Kitagawa, V.I. Kopylov, Fracture and Fatigue Resistance of Ultrafine Grain CuCrZr Alloy Produced ECAP, Mater. Sci. Forum. 503–504 (2006) 811–816.
[38] ASTM-E399-12e3, ASTM E399-12e3, Standard Test Method for Linear-Elastic Plane-Strain Fracture Toughness KIc of Metallic Materials, ASTM Int. (2012).
[39] P. Paris, F. Erdogan, A Critical Analysis of Crack Propagation Laws, J. Basic Eng. 85 (1963) 528–533.
[40] F.O. Riemelmoser, R. Pippan, Crack Closure: A concept of fatigue crack growth under examination, Fatigue Fract. Eng. Mater. Struct. 20 (1997) 1529–1540.
[41] R.O. Ritchie, Mechanisms of fatigue crack propagation in metals, ceramics and composites: Role of crack tip shielding, Mater. Sci. Eng. A. 103 (1988) 15–28.
[42] S. Suresh, Micromechanisms of fatigue crack growth retardation following overloads, Eng. Fract. Mech. 18 (1983) 577–593.
[43] R. Pippan, L. Plöchl, F. Klanner, H. Stüwe, The Use of Fatigue Specimens Precracked in Compression for Measuring Threshold Values and Crack Growth, J. Test. Eval. 22 (1994) 98.
[44] R. Pippan, Dislocation emission and fatigue crack growth threshold, Acta Metall. Mater. 39 (1991) 255–262.
[45] F.O. Riemelmoser, R. Pippan, H.P. Stüwe, A comparison of a discrete dislocation model and a continuous description of cyclic crack tip plasticity, Int. J. Fract. 85 (1997) 157–168.
[46] C. Laird, The Influence of Metallurgical Structure on the Mechanisms of Fatigue Crack Propagation, Fatigue Crack Propagation, ASTM STP 415. (1967) 131.
[47] C. Laird, G.C. Smith, Crack propagation in high stress fatigue, Philos. Mag. 7 (1962) 847–857.
[48] P. Neumann, Coarse slip model of fatigue, Acta Metall. 17 (1969) 1219–1225.
[49] R.M.N. Pelloux, Crack extension by alternating shear, Eng. Fract. Mech. 1 (1970) 697–704.
[50] J. Rice, The mechanics of crack tip deformation and extension by fatigue, Fatigue Crack Propagation, ASTM, ASTM STP. (1967) 415.
[51] C. Holzapfel, W. Schäf, M. Marx, H. Vehoff, F. Mücklich, Interaction of cracks with precipitates and grain boundaries: Understanding crack growth mechanisms through focused ion beam tomography, Scr. Mater. 56 (2007) 697–700.
[52] I.A. Ovid'ko, A.G. Sheinerman, E.C. Aifantis, Stress-driven migration of grain boundaries and fracture processes in nanocrystalline ceramics and metals, Acta Mater. 56 (2008) 2718–2727.

[53] K.S. Kumar, S. Suresh, M.F. Chisholm, J.A. Horton, P. Wang, Deformation of electrodeposited nanocrystalline nickel, Acta Mater. 51 (2003) 387–405.
[54] M.Y. Gutkin, I.A. Ovid'ko, Nanocracks at grain boundaries in nanocrystalline materials, Philos. Mag. Lett. 84 (2004) 655–663.
[55] I.A. Ovid'ko, A.G. Sheinerman, Grain size effect on crack blunting in nanocrystalline materials, Scr. Mater. 60 (2009) 627–630.
[56] R. Pippan, Threshold and effective threshold of fatigue crack propagation in ARMCO iron I: The influence of grain size and cold working, Mater. Sci. Eng. A. 138 (1991) 1–13.
[57] Y. Yang, N. Yao, B. Imasogie, W.O. Soboyejo, Nanoscale and submicron fatigue crack growth in nickel microbeams, Acta Mater. 55 (2007) 4305–4315.
[58] B. Yang, H. Vehoff, A. Hohenwarter, M. Hafok, R. Pippan, Strain effects on the coarsening and softening of electrodeposited nanocrystalline Ni subjected to high pressure torsion, Scr. Mater. 58 (2008) 790–793.
[59] B. Yang, H. Vehoff, R. Pippan, Overview of the Grain Size Effects on the Mechanical and Deformation Behaviour of Electrodeposited Nanocrystalline Nickel − From Nanoindentation to High Pressure Torsion, Mater. Sci. Forum. 633–634 (2010) 85–98.
[60] O. Renk, A. Hohenwarter, K. Eder, K.S. Kormout, J.M. Cairney, R. Pippan, Increasing the strength of nanocrystalline steels by annealing: Is segregation necessary?, Scr. Mater. 95 (2015) 27–30.
[61] C. Bichler, R. Pippan, Effect of single overloads in ductile metals: A reconsideration, Eng. Fract. Mech. 74 (2007) 1344–1359.
[62] R. Pippan, C. Zelger, E. Gach, C. Bichler, H. Weinhandl, On the mechanism of fatigue crack propagation in ductile metallic materials, Fatigue Fract. Eng. Mater. Struct. 34 (2011) 1–16.
[63] C. Kammerhofer, A. Hohenwarter, R. Pippan, A novel laboratory test rig for probing the sensitivity of rail steels to RCF and wear – first experimental results, Wear. 316 (2014) 101–108.
[64] C. Kammerhofer, A. Hohenwarter, S. Scheriau, H.P. Brantner, R. Pippan, Influence of morphology and structural size on the fracture behavior of a nanostructured pearlitic steel, Mater. Sci. Eng. A. 585 (2013) 190–196.
[65] S. Maya-Johnson, A.J. Ramirez, A. Toro, Fatigue crack growth rate of two pearlitic rail steels, Eng. Fract. Mech. 138 (2015) 63–72.
[66] F. Wetscher, R. Stock, R. Pippan, Changes in the mechanical properties of a pearlitic steel due to large shear deformation, Mater. Sci. Eng. A. 445–446 (2007) 237–243.
[67] G. Eggeler, E. Hornbogen, A. Yawny, A. Heckmann, M. Wagner, Structural and functional fatigue of NiTi shape memory alloys, Mater. Sci. Eng. A. 378 (2004) 24–33.
[68] K.. Melton, O. Mercier, Fatigue of NITI thermoelastic martensites, Acta Metall. 27 (1979) 137–144.
[69] T. Duerig, A. Pelton, D. Stöckel, An overview of nitinol medical applications, Mater. Sci. Eng. A. 273 (1999) 149–160.
[70] E. Schafer, Root canal instruments for manual use: a review, Dent. Traumatol. 13 (1997) 51–64.
[71] S.A. Shabalovskaya, On the nature of the biocompatibility and on medical applications of NiTi shape memory and superelastic alloys, Biomed. Mater. Eng. 6 (1996) 267–289.
[72] R. Valiev, Nanostructuring of metals by severe plastic deformation for advanced properties., Nat. Mater. 3 (2004) 511–6.
[73] B. Kockar, I. Karaman, J.I. Kim, Y.I. Chumlyakov, J. Sharp, C.-J. (Mike) Yu, Thermomechanical cyclic response of an ultrafine-grained NiTi shape memory alloy, Acta Mater. 56 (2008) 3630–3646.
[74] R. Valiev, D. Gunderov, E. Prokofiev, V. Pushin, Y. Zhu, Nanostructuring of TiNi Alloy by SPD Processing for Advanced Properties, Mater. Trans. 49 (2008) 97–101.
[75] D. Gunderov, A. Lukyanov, E. Prokofiev, A. Churakova, V. Pushin, S. Prokoshkin, et al., Microstructure and Mechanical Properties of the SPD-Processed TiNi Alloys, in: Mater. Sci. Forum, 2013: pp. 486–490.
[76] H. Shahmir, M. Nili-Ahmadabadi, Y. Huang, J. Myun Jung, H. Seop Kim, T.G. Langdon, Shape memory effect in nanocrystalline NiTi alloy processed by high-pressure torsion, Mater. Sci. Eng. A. 626 (2015) 203–206.

[77] Y.X. Tong, F. Chen, B. Guo, B. Tian, L. Li, Y.F. Zheng, et al., Superelasticity and its stability of an ultrafine-grained Ti49.2Ni50.8 shape memory alloy processed by equal channel angular pressing, Mater. Sci. Eng. A. 587 (2013) 61–64.
[78] D. Tabor, A Simple Theory of Static and Dynamic Hardness, Proc. R. Soc. A Math. Phys. Eng. Sci. 192 (1948) 247–274.
[79] G.R. Irwin, Plastic zone near a crack and fracture toughness, Proc. Seventh Sagamore Ordnance Mater. Res. Conf. (1960) IV-63.
[80] C.F. Shih, Relationships between the J-integral and the crack opening displacement for stationary and extending cracks, J. Mech. Phys. Solids. 29 (1981) 305–326.
[81] M. Hafok, R. Pippan, High-pressure torsion applied to nickel single crystals, Philos. Mag. 88 (2008) 1857–1877.
[82] B.J. Bonarski, E. Schafler, B. Mingler, W. Skrotzki, B. Mikulowski, M.J. Zehetbauer, Texture evolution of Mg during high-pressure torsion, J. Mater. Sci. 43 (2008) 7513.

7 List of appended papers

Paper A
Thomas Leitner, Anton Hohenwarter, Reinhard Pippan
Fatigue crack growth behavior of ultrafine-grained nickel produced by high pressure torsion
Procedia Materials Science (2014/3) 1044-1049

Paper B
Thomas Leitner, Anton Hohenwarter, Reinhard Pippan
Revisiting fatigue crack growth in various grain size regimes of Ni
Materials Science and Engineering: A (2015/646) 294–305

Paper C
Thomas Leitner, Anton Hohenwarter, Walter Ochensberger, Reinhard Pippan
Fatigue crack growth anisotropy in ultrafine-grained iron
Acta Materialia, (2017/126) 154–165

Paper D
Thomas Leitner, Ilchat Sabirov, Reinhard Pippan, Anton Hohenwarter
The effect of severe grain refinement on the damage tolerance of a superelastic NiTi shape memory alloy
Submitted for publication

Remarks:
In the appended papers, all experiments, the data analyses and the compositions of the publications were performed by myself, Thomas Leitner, with the following exceptions:

- In **paper C**, Dr. Walter Ochensberger performed simulations in order to obtain information about the driving force of cracks, which deviate from a straight crack path.
- Dr. Ilchat Sabirov provided the material and data of tensile tests on ECAPed NiTi for **paper D**.
- **In paper D**, Alexander Leitner and Dr. Verena Maier-Kiener performed nanoindentation tests on un-deformed and ECAPed NiTi and determined the Young's modulus of the materials.
- My supervisors, Dr. Anton Hohenwarter and Prof. Dr. Reinhard Pippan, gave the basic ideas for the publications and contributed to all papers with valuable input and helpful discussions.

A Fatigue crack growth behavior of ultrafine-grained nickel produced by high pressure torsion

Thomas Leitner [1], Anton Hohenwarter [1], Reinhard Pippan [2]

[1] Department of Materials Physics, Montanuniversität Leoben, Leoben, Austria

[2] Erich Schmid Institute of Materials Science, Austrian Academy of Sciences, Leoben, Austria

Abstract

In this work the fatigue crack growth behavior of ultrafine-grained high purity nickel, produced by high pressure torsion, was studied. Fatigue crack growth curves of samples with different orientations were measured at two stress ratios. It was found that cracks propagating in two specific directions of the HPT disc show differences up to a factor of four in their fatigue crack growth rate and also deviations in their ΔK_{th} values. By the analysis of stereophotogrammetric images of the fracture surfaces, crack branching and crack deflection were found to be active crack tip shielding mechanisms. Only a small influence of the stress ratio has been observed.

A.1 Introduction

Information about the fatigue crack growth behavior of a material is essential for engineering applications. When a crack already exists in a component, introduced e.g. by the manufacturing process, it is important to know under which loading conditions a crack will start to grow and at which rate it will propagate.

Whereas fatigue crack propagation has been determined for a vast majority of engineering materials over the last decades, the fatigue behavior is still not extensively studied for the newly introduced material classes of nanocrystalline (nc) and ultrafine-grained (ufg) materials. These materials are of great interest as they show improved mechanical and physical properties compared to their coarse grain counterparts [1]. However, a majority of works reports inferior fatigue crack growth behavior (e.g. [2]), with only few exceptions (e.g. [3]). This could be a drawback for the promising class of nanostructured and ultrafine-grained materials, as they would show a reduced damage tolerance under cyclic loading.

In severely plastically deformed (SPD) material produced by high pressure torsion (HPT), which is one of the mayor SPD techniques, a characteristic grain shape and orientation exists, with elongated grains inclined about 10° to the shear direction which is the tangential direction in HPT samples [4, 5]. Experiments on HPT deformed materials have shown an unusual large effect of the testing direction on their mechanical properties, such as tensile strength, ductility and fracture toughness [4, 6, 7]. Therefore it is of natural interest to expand such studies onto the FCG of differently orientated cracks, in order to see if they show different behavior and if there are orientations that have a larger resistance to crack propagation.

A.2 Material and methods

Nickel with a purity of 99.99% was deformed by HPT at room temperature with a pressure of 3.7 GPa for 15 revolutions. Thereby discs with a diameter of 30 mm and a height of 7.5 mm were produced. A saturation hardness of about 280 HV 0.5 was measured, which, according to Rathmayr et al. [8], correlates very well to a grain size of 450nm, determined with EBSD. Samples were only taken from regions with a shear strain γ from 40 to 200 where it can be assumed that a saturation microstructure was reached. Compact tension (CT) samples were prepared with four different orientations, also shown schematically in Fig. A-1:

- Crack in axial direction = AD
- Crack in radial direction = RD
- Crack in tangential direction, cracking plane parallel to shear plane = TD
- Crack in tangential direction, cracking plane perpendicular to shear plane = TD-B

The sizes of the CT specimens were chosen according to the standard E647 [9], with W=5.4mm, B=1.0mm to 1.3mm and a_n=0.9mm to 1.4mm, equal for all orientations. Notches were produced with a diamond wire saw and extended and sharpened to a radius of 5 to 30 μm by razor blade grinding. Finally a fatigue crack was introduced with a resonance testing machine (Rumul Russenberger + Müller, Switzerland) under cyclic compressive load. The compression load was kept as low as possible to generate an open crack of 20 – 50 μm length, measured from the root of the notch to minimize the tensile residual stresses in front of the pre-crack [10].

In order to measure the crack length during the FCG experiments the potential drop technique (PDT) was used. Therefore wires were attached to the specimens by point welding for electrical current input and potential drop measurement at the crack. The position of the attachment of the wires was the same for all specimens. Wires for the current input were attached at the height of the end of the pre-crack and wires for the potential measurement were welded 0.45 to 0.65mm symmetrically from the center, as can be seen in Fig. A-2.

To calculate the crack length from the potential drop at the crack a calibration function was determined. This was done in two ways: Firstly by simulating the potential of a specimen with the same dimensions and the same electrical current input for various crack lengths with the simulation software FEMM [11]. Secondly by the usage of the analogue method, where an aluminum foil with 10 times enlarged dimensions of the CT specimens was slit by a razor blade and the changes of the potential drop were measured. Both methods showed the same results and a fit of the data was used to calculate the crack length.

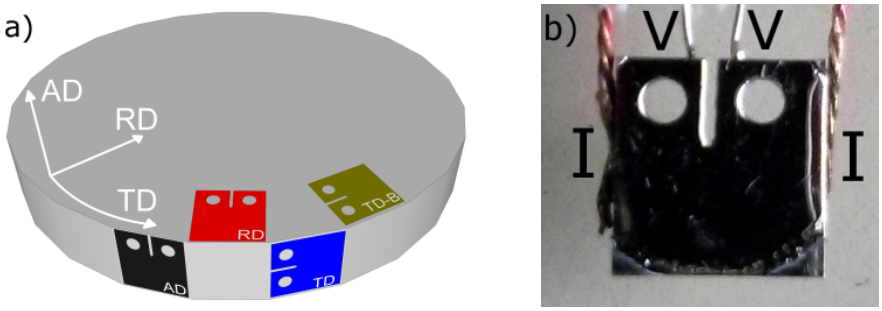

Fig. A-1: (a) Schematic of the different orientations of the investigated specimens; (b) Image of a CT specimen, showing the positions of the attached wires. Wires marked with I are for current input, wires marked with V are for potential measurement.

The FCG experiments were carried out on a MTS Tytron 250 microforce testing system with a 250 N load cell and a sinusoidal force with a frequency of 40 Hz. Specimens were tested at stress ratios of R=0.1 and R=0.7. To find the threshold of stress intensity range ΔK_{th} FCG experiments were started with low stress intensity ranges of about ΔK=1.5 MPa $m^{0.5}$. If after 200,000 loading cycles the measured crack propagation was less than 10µm (i.e. a FCG rate less than $5*10^{-11}$ m/cycle), it was assumed that the crack did not propagate and the load was increased by a ΔK of 0.2 MPa $m^{0.5}$. This was repeated until a crack growth rate higher than $5*10^{-11}$ m/cycle was detected and the crack finally propagated until the failure of the specimen. In order to get FCG data at higher ΔK also, the testing of some samples was started at ΔK of 4 to 9 MPa $m^{0.5}$ and continued until failure.

After the FCG experiments the FCG curves were calculated and crack paths of the samples compared. Furthermore the fracture surfaces were studied in the scanning electron microscope (SEM) "LEO Gemini 1525" with field emission cathode. For the creation of stereophotogrammetric images to reconstruct the surface topography, SEM images of exactly the same positions were taken at tilting angles of 0° and 3° [12] and combined and analysed with the software MeX of Alicona Imaging Corporation.

A.3 Results

A.3.1 Crack Paths

After the FCG experiments the crack paths in the different orientations were studied. An overview of to crack paths in the differently orientated specimens is given in Fig. A-2. It is obvious that there are preferred crack growth orientations. Cracks in AD specimens do not propagate in the axial direction predetermined by the notch, but grow in a plane approximately 25° inclined to the shear plane of the HPT process. Cracks in TD specimens only deviate slightly from the predetermined direction and grow in a plane approximately 15° inclined to the shear plane. In RD samples cracks gradually change their paths to the tangential direction and are finally perpendicular to the introduced pre-crack. For TD-B samples the predetermined crack path is already in tangential direction and therefore the crack path only shows a slight curvature.

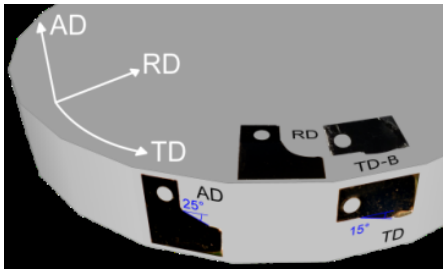

Fig. A-2: Illustration of the crack path in the differently orientated samples and their position in a HPT disc.

A.3.2 Fatigue crack growth diagrams

In Fig. A-3 FCG curves are shown. There are remarkable differences caused by the orientation of the samples in the ΔK_{th} values and especially the FCG rates of the tested samples. With ΔK_{th}=2.0 MPa $m^{0.5}$ TD specimens showed the lowest threshold values, followed by TD-B specimens with ΔK_{th}=2.4 to 2.6 MPa $m^{0.5}$ and AD with ΔK_{th}=2.6 to 2.9 MPa $m^{0.5}$. For RD specimens the highest threshold values of ΔK_{th}=2.7 to 2.9 MPa $m^{0.5}$ were measured.

Even more obvious are the differences concerning the FCG rates, especially between RD and TD samples. In the steady state region of TD samples, cracks were found to propagate about 4 times faster than in RD samples. AD and TD-B samples showed the same FCG rates as TD specimens, with only small deviations.

Comparing FCG curves measured at different stress ratios it is interesting to note that the curves are essentially the same, both considering ΔK_{th} and the FCG rates.

The steady-state or Paris region of all measured FCG curves can be fitted very well with ΔK^2 as depicted with dash-dotted lines in the diagrams.

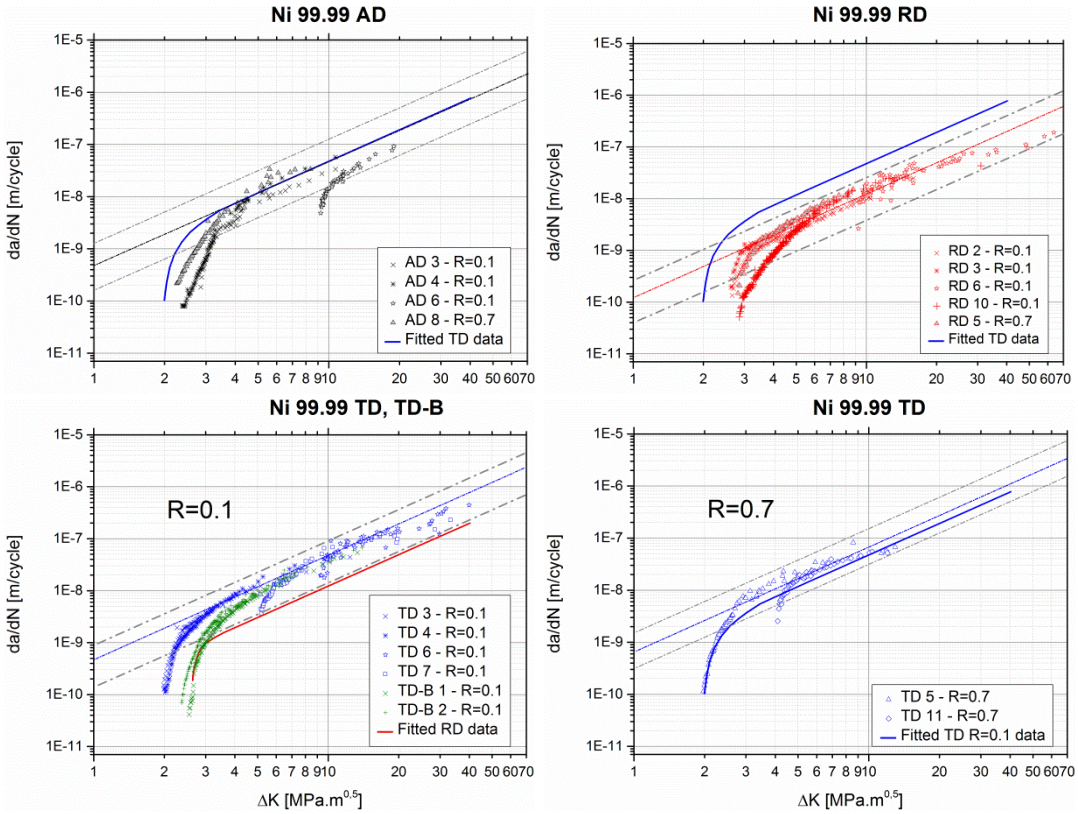

Fig. A-3: Effect of sample orientation and stress ratio on FCG curves. (a), (b) FCG curves for AD and RD specimens, respectively. Always one dataset is from tests at a stress ratio of 0.7 (shaded triangles, e.g. AD 8, RD 5), the rest of the experiments was performed at a stress ratio of R=0.1. Two to three R=0.1 experiments were carried out in order to find the threshold of stress intensity range ΔK_{th} and therefore start at low ΔK values (e.g. AD 3, RD 2). Additional tests were performed in order to get information about FCG behavior at larger ΔK and therefore were started at higher ΔK (e.g. AD 6 and RD 6). (c) FCG curves of TD and TD-B samples tested at R=0.1. (d) FCG curves of TD samples tested at R=0.7. For a better comparison fitted FCG curves of the respective other orientations were added in all diagrams (blue and red solid lines). Dash-dotted lines are proportional to ΔK^2.

A.3.3 Fracture surface analysis

Fracture surfaces of the specimens were analyzed in the SEM. In all specimens intergranular fracture is observed and the form of the grains can clearly be seen. However, depending on the orientation of the cracking plane the samples show quite different fracture surface morphologies. In order to get more information about the roughness, three dimensional stereophotogrammetric images were created, shown in Fig. A-4. In these images the height of the fracture surface was measured along certain paths, depicted by black arrows in Fig. A-4. These height profiles are presented in Fig. A-5.

As illustrated in Fig. A-4(a), fracture surfaces of RD samples appear very rough, with big elevated regions and deep depressions. Compared to the other orientations the grains look equiaxed. In contrast, TD fracture surfaces in general appear much smoother than the others (Fig. A-4(b)), which can also be seen in its height profile, blue curve in Fig. A-5(a). Looking at the fractorgraph of a TD-B sample in Fig. A-4(c) and the height profile 1 in Fig. A-5(b), there are also large differences in height visible. However, in the fracture surface of this sample there are paths that are smoother, where the crack was only sometimes somewhat deflected, as

shown in the height profile 2 in Fig. A-5(b). Furthermore, it can be seen that grains are elongated and about 20° inclined to the crack propagation direction.

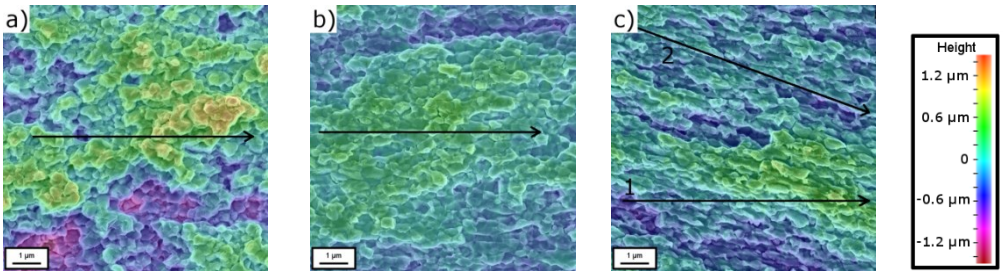

Fig. A-4: Fractographs of (a) RD, (b) TD and (c) TD-B samples after 1500µm crack propagation. Colors show the height of the surface determined by a stereophotogrammetric technique. Paths of height measurements of the fracture surface shown in Fig. A-5 are marked by black arrows. Crack propagated from left to right.

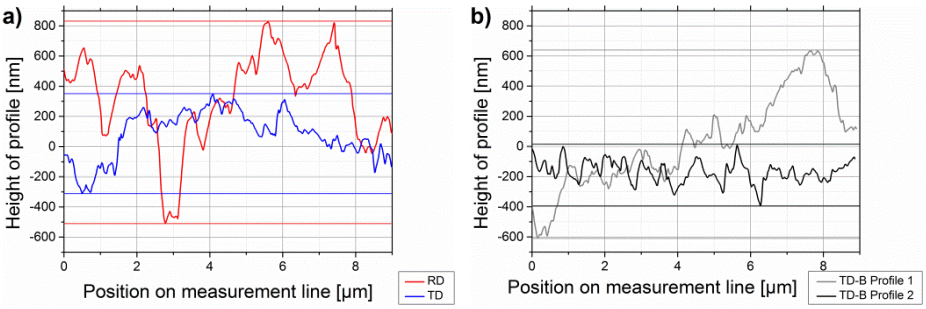

Fig. A-5: Height of the profiles marked by black arrows in Figs. 4(a)-(c). (a) Profiles of RD and TD. (b) Profiles of the two different paths marked in Fig. A-4(c).

A.4 Discussion

For HPT deformed nickel it was found that in the Paris region of FCG curves shows FCG rates proportional to ΔK^2, which indicates that fracture is controlled by plastic deformation of the crack tip. However, by looking at the fracture surface it can be observed that all samples show intergranular fracture.

Surprisingly large differences between the differently orientated samples were found, especially concerning their FCG rates. Specimens with cracks propagating in tangential direction on cracking planes parallel or perpendicular to the shear plane of the HPT discs (TD and TD-B specimens) show a four times larger FCG rate than samples with cracks propagating in radial direction (RD specimens). Cracks propagating in radial or axial direction seem to experience a much higher resistance, which, in case of RD samples leads to a higher ΔK_{th} and a lower FCG rate in the Paris region. Furthermore the crack deviates from its predetermined path to directions with less resistance, either gradually like for RD samples or by kinking already at the start of the crack propagation, as it was observed for AD samples. Reasons for the different resistances against crack growth can be found by analyzing the fracture surfaces. When a crack grew in radial direction the fracture surface appears much rougher than for cracks in tangential directions. The rough fracture surfaces indicate that the crack was strongly deflected during its propagation, which causes geometrical shielding and more crack branching. These mechanisms seem to reduce the load at the crack tip and reduce the FCG rate [13]. Grains in HPT microstructures are elongated due to the shear process, with the major axis lying about 10° inclined to the shear plane of the HPT process [4, 5]. Cracks growing in the tangential direction of the HPT disc can follow the elongated grain boundaries and are therefore less deflected, which results in smoother

fracture surfaces. A crack propagating in radial or axial direction encounters more grain boundaries and is more likely to get deflected and to branch. Hence these directions exhibit a higher resistance against crack growth.

For the tested samples the stress ratio showed only a small influence on the FCG curves. This indicates that crack closure mechanisms are not pronounced. It seems that only plasticity induced crack closure is present.

A.5 Conclusion

In this work it was observed that samples from HPT deformed nickel show significant differences in their fatigue crack growth behavior, depending on the orientation of the crack. However, all samples have in common that they show intergranular fracture. Samples with a crack in the tangential direction of the HPT disc show higher ΔK_{th} values and a four times higher fatigue crack growth rate than specimens with a crack propagating in radial direction. This higher resistance against crack growth is caused by the orientation of the elongated grains of the HPT microstructure. When a crack encounters more grain boundaries, as it is the case for cracks propagating in radial direction, the crack is more likely to branch and deflect. Therefore the load at the crack tip is reduced and the crack propagates at lower fatigue crack growth rates.

Since there was only a small influence of the stress ratio observed, it can be assumed that roughness or oxide induced crack closure mechanisms are not active.

A.6 References

[1] R. Valiev, R. Islamgaliev, I. Alexandrov, 2000. Bulk nanostructured materials from severe plastic deformation, Prog. Mater. Sci. 45, 103 – 189.

[2] K. Kumar, H. Van Swygenhoven, S. Suresh, 2003. Mechanical behavior of nanocrystalline metals and alloys, Acta Mater. 51 5743-5774.

[3] M. Sangid, G. Pataky, H. Sehitoglu, R. Rateick, T. Niendorf, H. Maier, 2011, Superior fatigue crack growth resistance, irreversibility and fatigue crack growth-microstructure relationship of nanocrystalline alloys, Acta Mater. 59, 7340-7355.

[4] A. Hohenwarter, R. Pippan, 2011. Fracture toughness evaluation of ultrafine-grained nickel, Scripa Materilia 64, 982-985.

[5] R. Pippan, S. Scheriau, A. Taylor, M. Hafok, A. Hohenwarter, A. Bachmaier, 2010. Saturation of fragmentation during severe plastic deformation, Annu. Rev. Mater. Res. 40, 319-343.

[6] G. Rathmayr, A. Hohenwarter, R. Pippan, 2013. Influence of grain shape and orientation on the mechanical properties of high pressure torsion deformed nickel, Mater. Sci. Eng. 560, 224 – 231.

[7] A. Hohenwarter, R. Pippan, 2010. Anisotropic fracture behavior of ultrafine-grained iron, Mater. Sci. Eng. A527, 2649-2656

[8] G. Rathmayr, R. Pippan, 2011. Influence of impurities and deformation temperature on the saturation microstructure and ductility of HPT-deformed nickel, Acta Mater. 59, 7228-7240.

[9] American Society for testing and materials, 2001. E647-00, Standard test method for measurement of fatigue crack growth rates, Annual book of ASTM Standards.

[10] B. Tabernig, R. Pippan, 2002. Determination of the length dependence of the threshold for fatigue crack propagation, Engineering Fracture Mechanics 69, 899-907.

[11] D. C. Meeker, Finite Element Method Magnetics, Version 4.2. http://www.femm.info.

[12] J. Stampfl, S. Scherer, M. Gruber, O. Kolednik, 1996. Reconstruction of surface topographies by scanning electron microscopy for application in fracture research, Applied Physics A: Mat. Sci. Proc. 63, 341-346.
[13] R. Ritchie, 1988. Mechanisms of Fatigue Crack Propagation in Metals, Ceramics and Composites: Role of Crack Tip Shielding, Mat. Sci. Eng. A103, 15-28.

B Revisiting fatigue crack growth in various grain size regimes of Ni

Thomas Leitner [1], Anton Hohenwarter [1], Reinhard Pippan [2]

[1] Department of Materials Physics, Montanuniversität Leoben, Leoben, Austria

[2] Erich Schmid Institute of Materials Science, Austrian Academy of Sciences, Leoben, Austria

Abstract

The fatigue crack growth characteristics of high purity nickel with grain sizes ranging from the micro- down to the nanocrystalline regime were examined. Fatigue crack growth measurements for different load-ratios combined with extensive fracture surface analyses revealed that dislocation motion is the dominating damage mechanism in the near-threshold region up to the Paris regime, irrespective of the grain size. Grain boundaries serve as preferential crack paths in the entire investigated grain size range, depending only on the loading conditions. The controlling factor is mainly the size of the cyclic plastic zone in comparison to the grain size. As a further peculiarity crack closure disappears for microstructures with a grain size below one micron. Along with the grain size variation the influence of the grain aspect ratio was in focus, which can cause a strong orientation dependence of the fatigue crack growth behavior. Elongated microstructures aligned perpendicular to the crack growth direction can considerably improve the overall resistance against fatigue crack growth.

B.1 Introduction

Ultrafine-grained (ufg) metals, with grain sizes between 1 μm and 100 nm and nanocrystalline (nc) metals, with grain sizes smaller than 100 nm, have extensively been studied during the last years. Nc and ufg materials can be produced by several processes, including severe plastic deformation (SPD), electrodeposition (ED), mechanical alloying and gas-phase condensation. It was shown that every production route entails specific microstructural features. Differences exist between materials produced by different techniques e.g. regarding the level of impurities or the type of grain boundaries, with a higher purity and a dominance of high angle grain boundaries typical for SPD materials [1]. Thus, for a valid comparison of materials from different production routes it must be ensured that the effect of variations of microstructural features other than the grain size is negligible for the measured mechanical properties. However, regardless of the production technique, nc and ufg metals show impressive strength and good wear resistance compared to their coarser grained counterparts, as it was shown in numerous overviews [1, 2, 3]. There exist certain drawbacks, like a reported loss of ductility and instability of the microstructure, however, this has already been profoundly studied and strategies were found to mitigate and overcome these disadvantages [4, 5, 6]. For the use of nc and ufg materials in engineering applications, also fracture toughness was investigated, which is a pre-requisite for a damage-tolerant design [6, 7, 8]. For instance, it was found that the fracture toughness of ufg Ni produced by severe plastic deformation (SPD) shows a remarkable combination of high fracture toughness and strength [8]. Especially in materials produced with SPD techniques anisotropy in mechanical properties was observed [8, 9]. Nc and ufg metals are also promising materials for the use in applications subjected to cyclic loading, as grain refinement is accompanied by an increase in the resistance against crack initiation [10, 11, 12]. However, also the fatigue crack growth (FCG) behavior has to be considered for an evaluation of the entire fatigue lifetime or the defect tolerance. Several works have shown that the FCG behavior of nc and ufg metals is deteriorated [13, 14, 15], i.e. the threshold for the propagation of an existing crack is lower and its crack growth rate higher. Hanlon et al. explained this result by the absence of extrinsic FCG mechanisms, such as closure, which therefore reduces the overall FCG resistance due to smaller crack path tortuosity [13]. In this work investigations on FCG are continued on pure Ni to gain further knowledge about the intrinsic and extrinsic processes controlling FCG.

When dealing with FCG it is important to distinguish between intrinsic and extrinsic mechanisms, which was established by Ritchie [16]. Intrinsic mechanisms are responsible for the material separation process when a cracked body is cyclically loaded. The separation process can be caused by mechanisms belonging to three different groups: fracture by accumulated damage, crack advance due to pure deformation and FCG by cyclic damage [17]. The inherent resistance of the material against these separation processes can be seen as the intrinsic crack growth resistance. However, there also exist so-called extrinsic or shielding mechanisms which can hinder crack growth and reduce the FCG rate. These mechanisms reduce the load at the crack tip and thereby the driving force of the FCG process. One possibility is crack deflection, which changes the loading conditions for geometric reasons when the crack deviates from a straight crack path. This can result in an overall reduction of the driving force [18]. So-called contact shielding mechanisms are based on a reduction of the load at the crack tip due to a premature contact of the crack faces. This type of closure can be induced by roughness, oxides, plasticity or due to crack bridging. It is important to take these shielding mechanisms into account in order to correctly describe FCG and to give lifetime predictions.

In this work two observations mentioned above will be further investigated: Firstly, the effect of the grain size, not only on the overall fatigue crack growth resistance, but also on the intrinsic and extrinsic FCG

mechanisms, will be studied. Grain size is expected to have also an influence on dislocation motion and thus on the intrinsic resistance. To study the effect of crack closure mechanisms, experiments at different load ratios were carried out. The load ratio R is defined as the ratio of the minimum load to the maximum load and equals the stress ratio (minimum stress to maximum stress) $R=F_{min}/F_{max}=\sigma_{min}/\sigma_{max}$. Furthermore detailed fracture surface studies on Ni with different grain sizes from the microcrystalline down to the nanocrystalline state are performed to gain more knowledge about this influence. Ni was chosen as data already exists for comparison. Furthermore a superior combination of strength and ductility was found [8], which should result in good FCG behavior. Secondly it will be investigated if anisotropy of fracture toughness found in ufg Ni produced by high pressure torsion [8] also results in fatigue crack growth anisotropy.

B.2 Material and experimental methods

Experiments were performed on high purity nickel with three different grain sizes (mc, ufg, nc) and different mechanical properties as shown in table B-1. Microcrystalline specimens were directly taken from as-received 99.99 % purity Ni from Goodfellow™. In order to produce an ultrafine-grained microstructure as-received Ni was deformed at room temperature by high pressure torsion for 16 rotations at a pressure of 3.67 GPa. The produced discs had a diameter of 30 mm and a thickness of 7.5 mm. Samples were only taken from regions having a saturation microstructure (shear strain γ of 40 to 200), which means a constant hardness and uniform microstructure along the radius. Plates of nanocrystalline Ni (65 x 35 x 2 mm) were produced by pulsed electrodeposition. The mechanical properties have already been studied in a work of Yang [19, 20]. Grain sizes were determined by EBSD or XRD. As-received Ni showed coarse equiaxed grains with an average diameter of about 50 µm (see Fig. B-1a). In ufg Ni grains are smaller and elongated in the tangential direction of the HPT process with a grain size of about 750x450x250 nm (Fig. B-1b). Grains of nc Ni are slightly elongated in ED growing direction with an average diameter of 30 nm (Fig. B-1c). Furthermore hardness measurements were carried out and further mechanical properties taken from literature [19, 20, 21, 22].

Table B-1: Properties of the three investigated Ni microstructures. (*) Yield strength is taken from [22]. (**) Data of nc Ni is taken from [19].

	mc Ni	ufg Ni *	nc Ni **
Production route	As-received	High pressure torsion	Pulsed electrodeposition
Purity [at%]	99.99%	99.99%	99.90%
Grain size	50 µm	750 x 450 x 250 nm	30 nm
Hardness	120 HV	280 HV	470 HV
Yield strength	385 MPa	800 MPa	1200 MPa

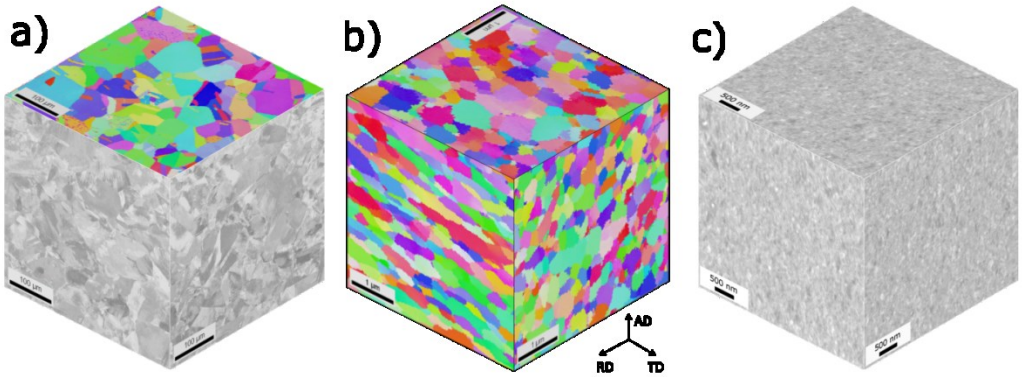

Fig. B-1: SEM images of the microstructure of a) mc Ni (top face EBSD, side faces BSE detector), b) ufg Ni (SEM, EBSD), c) nc Ni (SEM, BSE signal). Grains of mc Ni appear equiaxed. Ufg Ni has clearly elongated grains in tangential direction (TD). Nc Ni shows slightly elongated grains in axial direction (AD).

From the ufg and nc Ni compact tension (CT) specimens were produced with W=5.4 mm, B=1.0-1.3 mm and a=1.0-1.3 mm, depicted in Fig. B-2a. Ufg Ni samples with two different orientations with respect to the HPT process were produced, as shown in Fig. B-2b. In TD samples the crack-plane is parallel to the HPT shearing plane and the crack propagates in tangential direction (TD), see Fig. B-2c. In RD samples the crack-plane is perpendicular to the HPT shear plane and the designated crack growth direction is the radial direction (RD), see Fig. B-2d. In order to match the requirements of linear-elastic fracture mechanics the size of CT specimens of mc Ni was chosen to be larger with W=16.6 mm, B=1.9 mm and a=3.0-3.6. For all specimens notches were produced with a diamond wire saw and further extended and sharpened to a radius of 5 to 30 µm by razor blade grinding with 6 µm diamond paste. Finally a fatigue pre-crack was introduced with a resonance testing machine (Rumul Russenberger + Müller, Switzerland) under cyclic compression loading at a load ratio of R=10 to generate a short and open pre-crack.

In order to measure the crack length during the FCG experiments the potential drop technique (PDT) was used. Therefore wires were attached to the specimens by point welding for electrical current input and potential drop measurement at the crack, an example is shown in Fig. B-2a. The position of the attachment of the wires was the same for all specimens. Wires for the current input were attached at the height of the end of the pre-crack and wires for the potential measurement were welded 0.45 to 0.65mm symmetrically from the center. To calculate the crack length from the potential drop a calibration function was determined. This was done in two ways: Firstly by simulating the potential of a specimen with the same dimensions and the same electrical current input for various crack lengths with the simulation software FEMM [23]. Secondly by the usage of an analogue method, where an aluminum foil with dimensions 10 times larger than the actual CT specimens was slit by a razor blade and the change of the potential drop as a function of "crack length" was measured to check the simulation [24]. Both methods showed the same results and a fit of the simulated data was finally used to calculate the crack length.

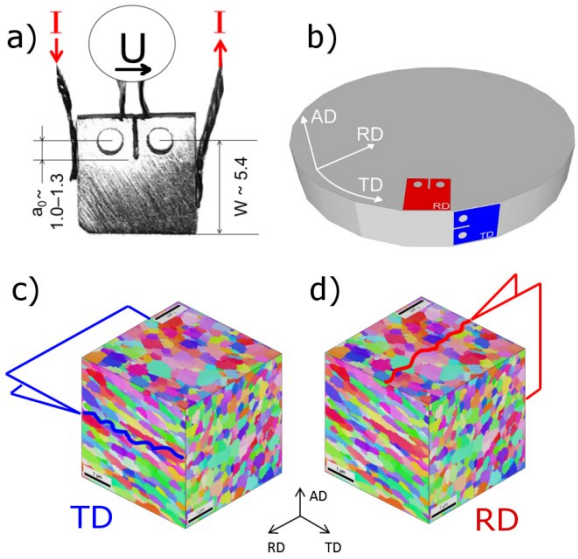

Fig. B-2: a) CT specimen with wires attached for crack length measurement using the potential drop technique. b) Schematic of the different samples taken from HPT discs. c) and d) Schematics of the orientation of cracks in TD and RD samples in relation to the microstructure. c) TD samples have a crack introduced in tangential direction (TD), with the cracking plane parallel to the HPT shear plane (RD – TD plane). d) RD samples have a crack introduced in radial direction (RD), with the cracking plane perpendicular to the HPT shear plane.

The FCG experiments were carried out on a MTS Tytron 250 microforce testing system with a 250 N load cell and a sinusoidal force with a frequency of 40 Hz. Specimens were tested at load ratios of R=0.1 and R=0.7. To find the threshold of stress intensity range ΔK_{th} the load rising method was used [25]: FCG experiments were started with low stress intensity ranges of about ΔK=1.5 MPa $m^{0.5}$. If after 500,000 load cycles the measured crack propagation was less than 10µm (i.e. a FCG rate less than $2*10^{-11}$ m/cycle), it was assumed that the crack did not propagate and the load was increased by a ΔK-increment of 0.2 MPa $m^{0.5}$. This was repeated until a crack growth rate higher than $2*10^{-11}$ m/cycle was detected and the crack finally propagated until the failure of the specimen. In order to get FCG data at higher ΔK as well, another set of samples was subjected to higher ΔK starting values and testing was continued until failure. During all tests data was only taken as long as the size of the plastic zone was significantly smaller than the thickness of the specimen B, i.e. $B > 2.5\ (K_{max}/\sigma_y)^2$, so that plane strain was prevailing [26]. Furthermore, for all data shown in this paper the remaining crack ligament (W-a) was large enough to guarantee the validity of linear elastic fracture mechanics according to [27], $W\text{-}a > (4/\pi)\ (K_{max}/\sigma_y)^2$. For all tested specimens the crack length exceeded $2.5\ (K_{max}/\sigma_y)^2$ so that short crack effects could be neglected.

After the FCG experiments the FCG curves were calculated and crack paths of the samples compared. Furthermore the fracture surfaces were studied in the scanning electron microscope (SEM) "LEO Gemini 1525" with field emission cathode. For a three-dimensional reconstruction of the surface topography stereophotogrammetric images with the SEM were taken at tilting angles of 0° and 3°. For details regarding this technique see [28].

B.3 Results

B.3.1 FCG data

FCG Experiments were performed on mc Ni, ufg Ni and nc Ni at the two different load ratios of R=0.1 and R=0.7 in order to see the effect of the mean stress and active closure mechanisms. The results are shown in Fig. B-3 and are discussed in the following sections.

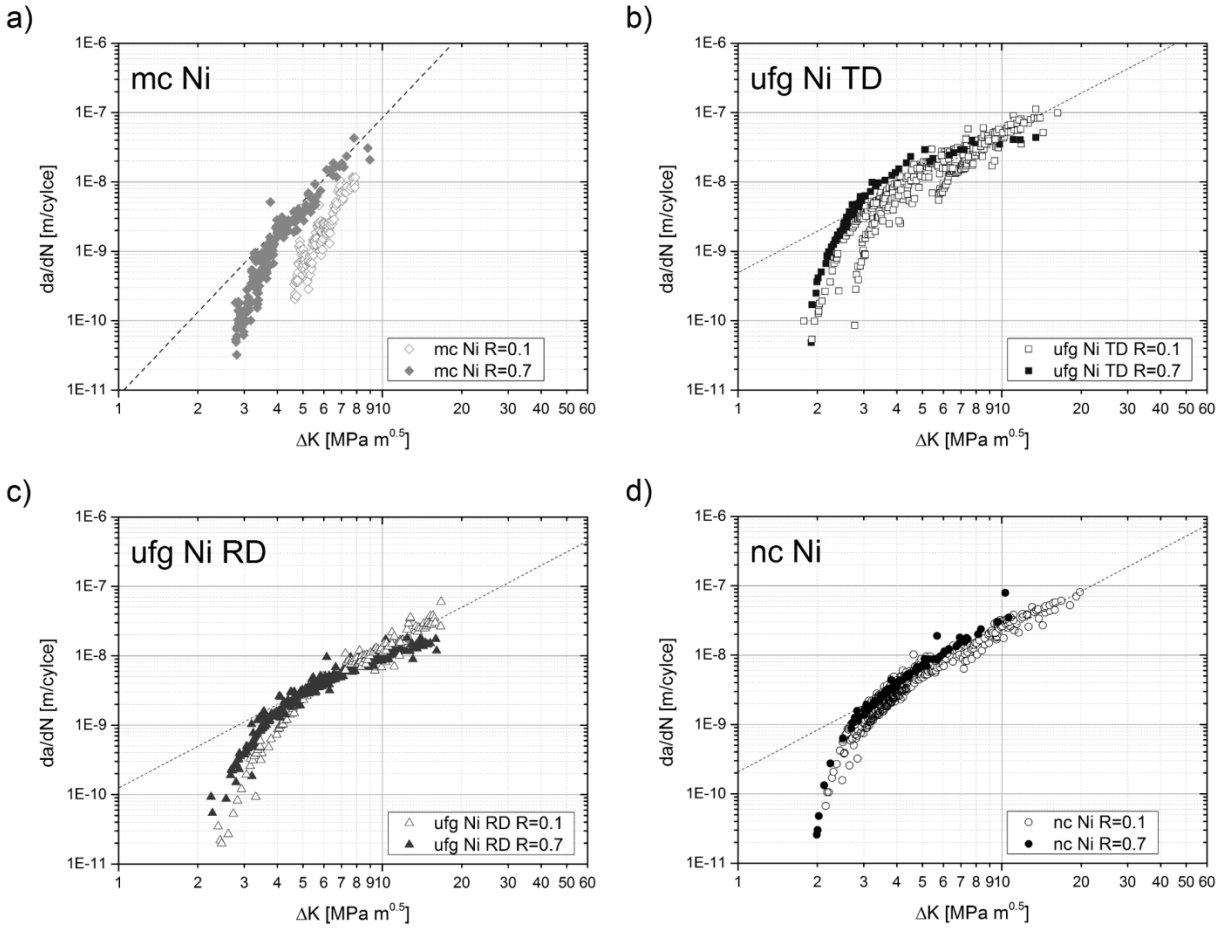

Fig. B-3: Fatigue crack growth diagrams of Ni with different grain sizes. Filled symbols represent data from R=0.7 experiments, open symbols represent data from R=0.1 experiments. Dashed lines are drawn for comparison with a slope of 2 (Paris exponent m=2) for nc and ufg Ni and with a slope of 4 (m=4) for mc Ni. As described in more detail in section 2, only valid data is shown in the diagrams.

B.3.1.1 Microcrystalline Ni

The results of FCG tests on mc Ni specimens are shown in Fig. B-3a. The open pre-cracks start to propagate when the stress intensity factor range ΔK reaches the effective threshold $\Delta K_{th,eff}$. However, the cracks always stopped growing after they had reached a certain length because crack closure was built up and thereby the load at the crack tip was reduced. When the load was increased this could happen again, until the load was equal or higher than the threshold value, ΔK_{th}. Once the stress intensity factor at the crack tip was larger than ΔK_{th} the crack propagated without stopping until failure. The onset and stopping of the crack

between $\Delta K_{th,eff}$ and ΔK_{th} is called cyclic R-curve behavior [29] and was found for all mc Ni samples. At higher mean stresses (R=0.7) first crack propagation was measured at $\Delta K_{th,eff}$=2.6 MPa.m$^{0.5}$, whereas for R=0.1 $\Delta K_{th,eff}$ was considerably higher (4.0 MPa.m$^{0.5}$). The same is true for the threshold values which were measured to be ΔK_{th}=2.8 MPa.m$^{0.5}$ and ΔK_{th}=4.6 MPa.m$^{0.5}$, for R=0.7 and R=0.1, respectively. From that it can be clearly seen that mc Ni shows an influence of the load ratio on the FCG behavior. The occurrence of R-curve behavior and the increase of the FCG rate with higher mean stresses indicate that crack closure mechanisms contribute to the FCG behavior [16]. The crack growth data in the FCG diagram shows a slope of about 4 between ΔK of 4 and 10 MPa.m$^{0.5}$ with higher FCG rates for increasing R.

B.3.1.2 Ultrafine-grained HPT Ni

In Fig. B-3b and B-3c the FCG data of ufg Ni with TD orientation and RD orientation respectively, is shown for experiments at R=0.1 and R=0.7. At higher mean stresses (R=0.7) ΔK_{th} is slightly lower and FCG rates are only marginally higher than for R=0.1. This indicates that the effect of roughness and plasticity induced crack closure is not very pronounced in ufg Ni, see section 4.1. In all ufg Ni samples, independent of the orientation, the crack did not propagate until applying a load corresponding to ΔK_{th}, from where on the crack started to grow until failure. Even in samples tested at R=0.1 the crack grew until failure of the specimen once crack growth was initiated at ΔK_{th}, i.e. no cyclic R-curve behavior was detected and $\Delta K_{th,eff}$ is equal to the stress intensity threshold ΔK_{th}.

The FCG behavior in the threshold and the Paris region showed remarkable differences depending on the orientation of the pre-crack with respect to the typical HPT-induced microstructure. A comparison of the FCG of two different ufg Ni orientations is included in Fig. B-4. It can be seen that samples with pre-cracks introduced parallel to the HPT shear plane, i.e. parallel to the grain elongation (TD samples) exhibit a 25% lower ΔK_{th} and a four times higher FCG rate in the Paris region than samples with the crack perpendicular to the HPT shear plane (RD samples). It is clearly shown that ufg Ni with TD orientation has a lower resistance against FCG than ufg Ni with RD orientation.

In contrast to the straight cracks of nc and mc Ni, in TD samples the fatigue cracks deviated about 15° from the designated growth direction, in RD samples the deviation angle of the crack continuously increased with the propagation of the crack. FCG data was only taken as long as the deviation angle of the crack was not larger than 30°. According to [30], a correction for long cracks is not necessary for a crack deflection angle smaller than 30°, as the difference in ΔK would be about 1% only.

B.3.1.3 Nanocrystalline ED Ni

For nc Ni basically the same results as for ufg Ni were obtained. FCG data at load ratio R=0.1 and R=0.7 are very similar to each other (see Fig. B-3d), again with only a slightly lower ΔK_{th} and slightly higher FCG rate for samples tested at R=0.7. Therefore, it seems that also in nc Ni the effect of plasticity and roughness induced crack closure is nearly negligible. More detailed explanations for the reduced effect of closure mechanisms are given in section 4.1. Like it was shown before for ufg HPT Ni, also nc Ni did not show a measurable R-curve behavior. Comparing the FCG data in Fig. B-4 it was found that the ΔK_{th} and the FCG rate of nc Ni is between the measured values of the two ufg HPT Ni orientations.

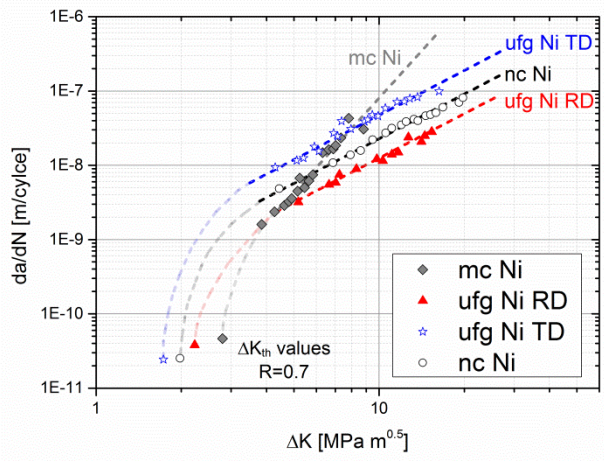

Fig. B-4: Comparison of the FCG data of nc Ni, ufg Ni with TD orientation, ufg Ni with RD orientation and mc Ni at higher ΔK. The measured threshold stress intensity factor ranges at R=0.7 and the corresponding FCG rates are also shown in the diagram (ΔKth values R=0.7).

Data of the samples corresponding to the Paris regime (region of constant slope of the FCG rate) of the da/dN – ΔK plot were fitted using the Paris law:

$$\frac{da}{dN} = C * \Delta K^m \tag{1}$$

It was found that the exponent m for nc and both orientations of ufg Ni is very close to 2, see table B-2. For a better comparison of the factors C, the exponent m was set to be 2 - which is close to the measured values – and the factors C were re-calculated to clearly show the differences in the FCG rates. As mentioned before and visible in the FCG diagrams, the FCG rate (and therefore also C) of nc Ni is about 2 times higher than the FCG rate of ufg Ni with RD orientation. Ufg Ni shows a four times higher FCG rate when cracks grow in TD orientation, i.e. parallel to the elongation direction of the grains, than when they grow in RD orientation, i.e. perpendicular to the elongation direction of the grains. An overview of the ΔK_{th} values is given in table B-3.

Table B-2: Factor C and exponent m of the Paris equation fitted to the FCG data of mc, ufg and nc Ni. In the last column the factor C is fitted under the premise m=2 for better comparison.

	C	m	C fitted for $m=2$
mc Ni	$3.16*10^{-12}$	4.4	–
ufg Ni RD	$0.72*10^{-10}$	2.22	$1.26*10^{-10}$
ufg Ni TD	$8.20*10^{-10}$	1.79	$4.90*10^{-10}$
nc Ni	$3.27*10^{-10}$	1.83	$2.12*10^{-10}$

Table B-3: Threshold stress intensity factor ranges ΔK_{th} of the studied Ni samples for the load ratios R=0.1 and R=0.7. For mc Ni the effective threshold stress intensity factor range $\Delta K_{th,eff}$ is put into parenthesis and the threshold stress intensity factor range ΔK_{th} is to the right.

	$R=0.1$	$R=0.7$
	ΔK_{th} MPa $m^{0.5}$	ΔK_{th} MPa $m^{0.5}$
nc Ni	2.1	2.0
ufg Ni TD	1.8	1.7
ufg Ni RD	2.4	2.2
mc Ni	(4.00) 4.63	(2.59) 2.80

B.3.2 Fracture surfaces

In order to explain the differences in the measured FCG data, the fracture surfaces of the samples were studied with the SEM and are shown in Fig. B-5 and Fig. B-6. Mc Ni shows a mixture of intercrystalline and transcrystalline fracture, with transcrystalline fracture dominating the threshold region (Fig. B-5a) and almost only intercrystalline fracture at higher ΔK (Fig. B-5b). Nc Ni exclusively exhibits intercrystalline fracture, independent of the ΔK (Fig. B-5c,d). The same is true for both ufg Ni states with TD and RD orientation (Fig. B-6a-d). On the fracture surfaces of ufg Ni with TD orientation it can be seen that the grains are elongated parallel to the crack growth direction (Fig. B-6a,b), whereas in the RD orientation grains appear more equiaxed (Fig. B-6c-d). In the nc Ni samples grains show an elongation perpendicular to the crack growth direction (Fig. B-5c-d). From the fracture surface images of nc and ufg Ni at higher ΔK (Fig. B-5d, B-6b, B-6d) it can be seen that grain coarsening occurs during cyclic loading.

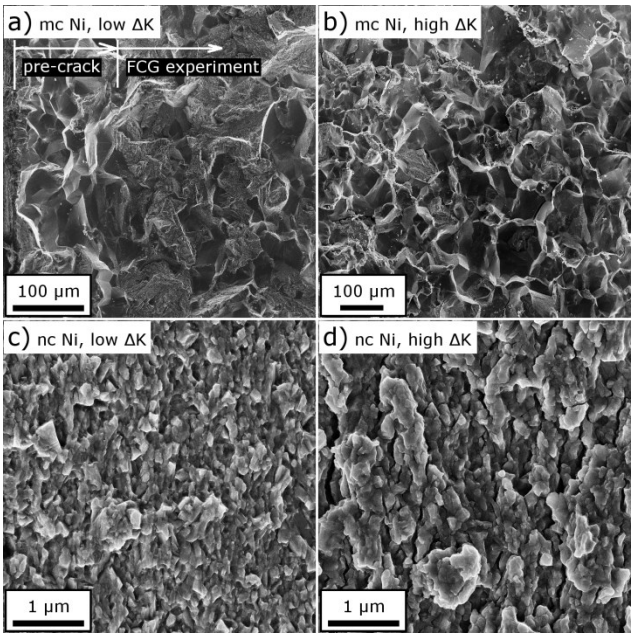

Fig. B-5: SEM images of the fracture surfaces of mc and nc Ni FCG sample. Images are taken in the near-threshold regime (a, c) and at higher stress intensity factor ranges ΔK=15-16 $MPa.m^{0.5}$ (b, d). The crack growth direction is from left to right.

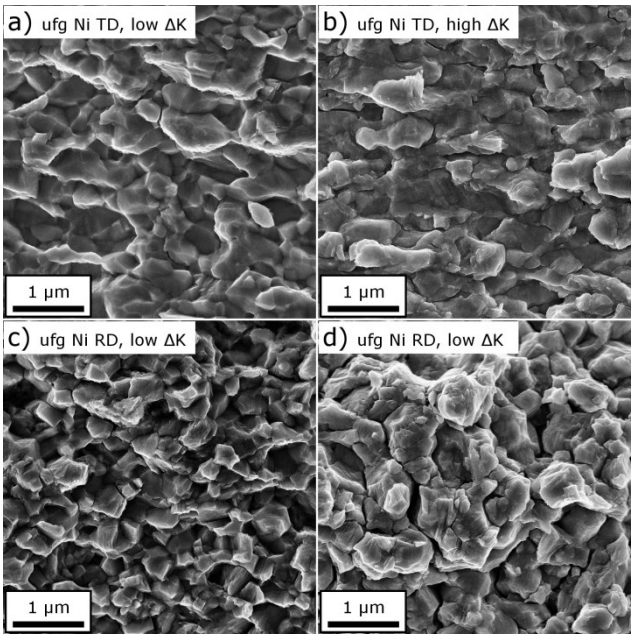

Fig. B-6: SEM images of the fracture surfaces of ufg Ni with TD orientation (a, b) and ufg Ni with RD orientation (c, d). Images are taken in the near-threshold regime (a,c) and at higher stress intensity factor ranges ΔK=15-16 MPa.m$^{0.5}$ (b, d). The crack growth direction is from left to right.

B.3.3 Crack path tortuosity

The crack path tortuosity, T, can be defined as the ratio of the true crack length to the projected crack length, $T= L_{true}/L_{proj}$. For the determination of the tortuosity the side faces of tested specimens were studied in the SEM and the crack lengths L_{true} and L_{proj} were measured. Area measurements of the fracture surfaces with stereophotogrammetric methods should yield the same result with the ratio of the true area to the projected area, $T= A_{true}/A_{proj}$, when the crack path tortuosity on the side faces is representative for the bulk. Stereophotogrammetric images of fracture surfaces were created using the Alincona MEX software and the true area and the projected area of the fracture surfaces were determined. The tortuosity values for the different microstructures are given in table B-4. Mc Ni has the highest crack path tortuosity, followed by ufg Ni with RD orientation. Ufg Ni with TD orientation and nc Ni show almost the same roughness, having the straightest crack path. Both approaches, line and area measurements, show the same trends with somewhat higher values for the area measurements.

Table B-4: Crack path tortuosity values calculated from line ($T= L_{true}/L_{proj}$) and area measurements ($T= A_{true}/A_{proj}$) at ΔK_{th}. Line and area measurements should yield the same result when the crack path tortuosity observed on the side face is representative for the bulk.

	Crack path tortuosity T at ΔK_{th}	
	Line measurement	Area measurement
ufg RD	1.54	1.77
ufg TD	1.11	1.44
nc	1.17	1.44
mc	1.68	1.51

B.4 Discussion

With respect to the present results some peculiarities in the FCG behavior of nc and ufg have been shown and will be discussed in more detail:

B.4.1 Why is the FCG behavior of nc and ufg Ni so insensitive to changes of the load ratio R?

In most materials with coarse- to fine-grained microstructures the increase of the load ratio and thereby the increase of the minimum load leads to faster fatigue crack propagation, especially in the near-threshold region [16]. At high load ratios this effect decreases or disappears in ductile materials. This is obviously an effect of crack closure: Oxide debris and crack face asperities in the crack wake behave like wedges at lower load ratios. With increasing load ratio and therefore increasing minimum load, the portion of the load cycles during which the crack is closed gets smaller and eventually no premature crack face contact can be observed anymore. Thus the full load amplitude acts on the crack tip, which results in faster crack growth at higher load ratio. Closure mechanisms are predominantly active in the near-threshold region, where loads and thus crack tip opening displacements are small. In contrast to these findings, no significant effect of the load ratio on the FCG rate in the near-threshold region and thus no pronounced effect of crack closure was observed for the investigated nc and ufg Ni specimens. However, this can be plausibly explained by the missing prerequisites of oxide- and roughness-induced crack closure. No debris or asperities from a cyclic formation and destruction of oxide layers were found on the fracture surfaces and hence an effect of oxide induced crack closure is negligible. For roughness induced crack closure (RICC) asperities large enough to lead to a premature contact of the crack faces, as well as a relative displacement of the crack faces in propagation direction is necessary (mode II component) [18,31]. From fracture surface studies and the measurement of the crack path tortuosity (table B-4) it can be seen that ufg Ni with RD orientation exhibits a fracture surface roughness comparable to the value of mc Ni. Despite the existence of these large asperities no pronounced effect of RICC was observed. Therefore it can be concluded that the absence of RICC is a result of reduced relative displacements of the crack faces in propagation direction for materials with very fine grains. This is in accordance with the results of other works [31, 32] which showed that the misfit becomes very small in nc and ufg metals. With only very small mode II displacements between the crack faces the effect of RICC diminishes for nc and ufg, even if asperities were large enough, as e.g. in ufg Ni with RD orientation.

Plasticity induced crack closure (PICC) is another mechanism, which leads to a reduction of the cyclic load at the crack tip and thus to a reduction of the FCG rate. Due to plastic deformation material flow to the crack tip is provoked, which again acts as a wedge. The existence of PICC under plane stress is easily explained by the out-of-plane plastic flow [33], prevalent for instance in thin sheets. However, also under plane strain conditions, which are predominant in the present test samples, PICC has been shown to be an active closure mechanism in the near threshold regime, as well as in the Paris regime in microcrystalline metals [34, 35]. When a crack propagates through the material, the crack tip is surrounded by a monotonic plastic zone. In this zone dislocations, which were emitted from the crack tip or generated in the vicinity of the crack tip, move and get stored. Due to cyclic loading a cyclic plastic zone forms, where some of these dislocations can glide back to the crack, depending on material properties such as grain size, effectiveness of obstacles for dislocations or flow stress. Dislocations which remain in the monotonic plastic zone cause a stress field which leads to the closure of the crack. In other words, dislocations forming the monotonic plastic wake cause a crack tip shielding (crack closure). However, during unloading the reversed motion of dislocations to the crack

tip in the cyclic plastic zone causes a reduction of shielding or causes anti-shielding and reduces the plasticity induced crack closure. It seems that in nc and ufg metals more of the previously generated dislocations can move back during unloading, compared to dislocations in coarser grained materials. In the threshold regime this might be caused by a more pronounced pile-up effect of the grain boundaries in nc and ufg materials. Dislocation pile-ups restrict the glide length and exert stresses, which promote a movement of dislocations back to the crack tip upon unloading. In the Paris regime the same effect results from cyclic softening of nc and ufg Ni due to grain coarsening. This coarsening is obvious when comparing fracture surface images in Fig. B-5 and Fig. B-6 for low and high ΔK. The grain coarsening, which occurs in the cyclic plastic zone, causes a reduction of the flow stress in the vicinity of the crack tip. Similar effects have been observed in LCF tests of ufg materials [36]. Thereby more dislocations previously generated in the monotonic plastic zone can glide back to the crack, i.e. the ratio of the size of the cyclic plastic zone to the size of the monotonic plastic zone gets larger. Hence, fewer dislocations remain in the area surrounding the crack tip, which leads to a reduction or nearly to a disappearance of PICC as described above.

In conclusion, the combination of the absence of oxide asperities and the strongly reduced roughness- and plasticity-induced closure is responsible for the insensitivity of the FCG behavior of nc and ufg Ni under plane strain conditions to changes in the load ratio.

B.4.2 What is the origin of the strong orientation dependence of FCG behavior in ufg Ni?

Experiments have shown that the FCG behavior of ufg Ni produced by HPT is anisotropic and depends on the orientation of the cracks in respect to the orientation of the elongated grains. This is similar to observations which were made for the fracture toughness of ufg Ni produced by HPT [8]. Samples with crack growth parallel to the elongation of the grains (TD orientation, see Fig. B-2) exhibit a 25% lower ΔK_{th} and a four times higher FCG rate than RD samples. A possible explanation for these differences is a variation in the effectiveness of geometrical shielding mechanisms. As discussed before, no pronounced oxide, roughness or plasticity induced crack closure is active in nc and ufg Ni. However, there is still the effect of crack deflection which should be taken into account. SEM studies and calculated roughness values of the fracture surfaces have shown that ufg Ni RD specimens exhibit more tortuous crack paths than TD samples. Cracks in TD can follow the elongated grains and are therefore much less deflected than cracks in RD samples (see Fig. B-2c). In RD samples cracks encounter more grain boundaries which are unfavorably orientated to its designated growth direction (Fig. B-2d). From this observation it seems reasonable that the amount of crack deflection is different for TD and RD samples. Crack deflection has two beneficial effects on the FCG in respect to the crack propagation rate: The driving force at the crack tip is reduced due to the geometry of the kinked crack. Additionally the true length of a regularly deflected crack is longer than that of a planar crack and therefore more cycles are needed for a regularly deflected crack to grow through a given structure or to reach a certain macroscopic crack length.

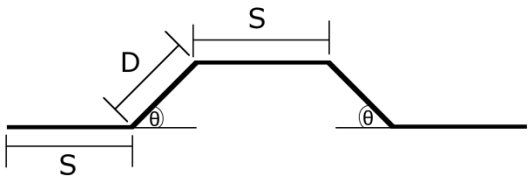

Fig. B-7: Schematic of a regularly tilted crack. Redrawn from [37].

S. Suresh proposed a model for regularly tilted cracks, as presented in Fig. B-7, which allows the calculation of the true crack driving force at the crack tip [37]. It is assumed that a crack consists of straight segments S and tilted segments D with an angle θ to the straight crack growth direction. It can be shown that a known crack path tortuosity T, i.e. a known ratio of true to projected area or length, is sufficient to calculate the crack driving force, ΔK_{tip} (see Eq. 2 and 3).

$$T = \frac{true\ area\ or\ length}{projected\ area\ or\ length} = \frac{S+D}{S+D*\cos(\theta)} \tag{2}$$

$$\Delta K_{tip} = \frac{D\ cos^2\left(\frac{\theta}{2}\right)+S}{D+S}\Delta K_{I,planar} = \frac{1+T}{2*T}\Delta K_{I,planar} \tag{3}$$

For the calculation of ΔK in general planar crack growth is assumed. This $\Delta K_{I,planar}$ is always higher than the real crack driving force at the crack tip ΔK_{tip} when crack deflections occur. With Eq. (3) taken from [37] the true crack driving force at the crack tip was recalculated, which is reduced by crack deflection shielding. As described before, RD and TD samples of ufg Ni are machined from the same pre-material and have the same microstructure, with only different crack growth directions. Thus, the threshold of crack propagation is expected to be the same. One reason that this was not the case in the experiments could be the different crack deflection behavior of the two orientations. The thresholds for crack growth in terms of the crack driving force $\Delta K_{tip,th}$ can be calculated with Eq. (3) and the measured crack path tortuosity values. The pre-cracks introduced by compression-compression loading, possess the same roughness as the specimens in the threshold region, i.e. the crack consists of differently deflected segments along the specimen thickness. From table B-5 we see that the local crack driving forces needed in RD and TD samples to initiate crack growth show a smaller difference (about 10%), compared to the threshold values with the assumption of a planar crack (22%). Thus it seems that in ufg Ni the influence of the crack orientation is at least partially an effect of the crack path tortuosity.

Table B-5: ΔK_{th} of ufg Ni samples at load ratios of R=0.7. The real driving force acting on the crack tip $\Delta K_{tip,th}$ was estimated with crack deflections taken into account.

	Measured ΔK_{th} @ $R=0.7$ [MPa $m^{0.5}$]	$\Delta K_{tip,th}$ (area measurement) [MPa $m^{0.5}$]	$\Delta K_{tip,th}$ (line measurement) [MPa $m^{0.5}$]
ufg Ni TD	1.73	1.47	1.64
ufg Ni RD	2.23	1.74	1.84
difference TD-RD	22.4%	16.0%	10.6%

The calculated crack length when using the potential drop technique is always the length of the crack projected on a straight crack path. Therefore the calculated FCG rate is the apparent FCG rate of a regularly deflected crack measured in Mode 1 direction, $(da/dN)_{apparent}$. The true FCG rate $(da/dN)_{true}$ of a crack with regular deflections, when taking the true crack length in account, is larger than that of a planar crack and can be calculated by Eq. (4).

$$\left(\frac{da}{dN}\right)_{true} = \left[\frac{D+S}{D\cos(\theta)+S}\right]\left(\frac{da}{dN}\right)_{apparent} = T\left(\frac{da}{dN}\right)_{apparent} \tag{4}$$

With Eq. (3) and (4) FCG curves can be calculated which show the true FCG rate (the true crack length is taken into account) in dependence of the crack driving force ΔK_{tip}. The FCG curves in Fig. B-8 are closer together than the original data, especially in the near-threshold region, however differences still exist.

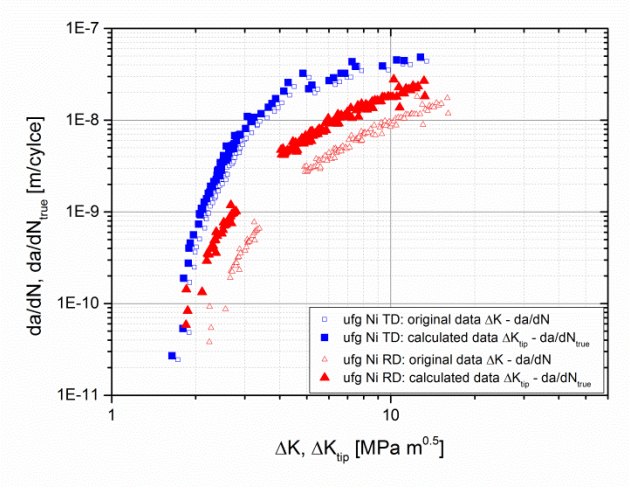

Fig. B-8: FCG curves of ufg Ni with TD and RD orientation. The open symbols show the original data, where da/dN is plotted over ΔK. The filled symbols represent the calculated true FCG rate, da/dN$_{true}$, in dependence on the calculated driving force at the crack tip, ΔK_{tip}.

From these calculations it can be assumed that a large part of the differences in the FCG behavior between ufg Ni samples with RD and TD orientations seem to be an effect caused by different crack deflection behavior. When a crack propagates parallel to the HPT shear plane (TD orientation) it can follow the boundaries of the elongated grains which serve as a weak crack path. Thus the crack shows less and smaller deflections. A crack growing perpendicular to the elongated grains is deflected continuously, resulting in a reduction of the local driving forces and hence in a higher resistance against FCG.

B.4.3 What induces the differences between nc and ufg Ni with respect to the FCG threshold and FCG rate?

The FCG behavior of nc and ufg Ni was found to be rather similar, despite the considerable difference in grain size (see section 3.1). For a better comparison, data from experiments with a load ratio of R=0.7 will be compared, where crack closure effects are reduced to a minimum. To exclude additional effects caused by different crack deflection behavior, nc Ni is compared to ufg Ni with a designated crack growth direction along the elongated grains (TD orientation). These samples show a similar crack path tortuosity and therefore no considerable difference in the effect of crack deflection should exist.

At a load ratio of R=0.7 ufg Ni shows a 15% lower threshold stress intensity factor range ΔK_{th} than ufg Ni with TD orientation, as can be seen in table B-3. Furthermore the FCG rate in ufg Ni with TD orientation is twice as high as in nc Ni (see Fig. B-3b,d and factors C in table B-2). Thus the overall FCG behavior of ufg Ni is deteriorated compared to nc Ni. In order to better understand the origins of these differences, it is important to find out which fracture mechanisms control FCG. In the FCG data of both nc and ufg Ni a slope of about 2 in the Paris region is measured. An exponent m of about 2 is an indication that in nc Ni as well as in ufg Ni FCG is controlled by plastic deformation, i.e. a result of a blunting and re-sharpening process [18]. This is surprising, as in fracture surface studies of nc and ufg Ni specimens only intercrystalline fracture

is observed (see Fig. B-5c-d and Fig. B-6), which is often believed to have its origin in grain boundary embrittlement, for example caused by sulfur [38]. However, high magnification SEM images, depicted in Fig. B-9, show that grain boundaries, which appear completely smooth at lower magnification, exhibit regular line patterns. These regularly appearing lines seem to be steps of slip bands resulting from the movement of dislocations in certain slip systems. Dislocations are moved and stored in slip bands and the crack has to propagate a certain distance from there on, in order to allow the formation of the next slip band [39]. On the fracture surfaces these steps can still be seen (Fig. B-9). From these findings it can be concluded that cracks propagate along the grain boundaries because they serve as weak crack paths. However, this intercrystalline FCG is not of brittle nature, i.e. not purely by material de-cohesion, but controlled by plastic deformation. This is also in accordance to the exponent m of about 2 observed in the Paris region of the FCG data of nc and ufg Ni.

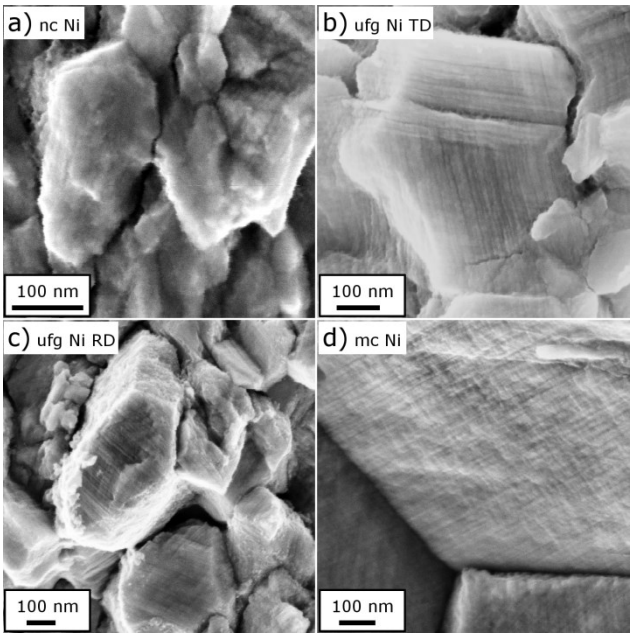

Fig. B-9: Steps from slip bands can be seen in SEM images at high magnifications as regular lines on all intercrystalline fracture surfaces, regardless of the grain size. a) nc Ni, b) ufg Ni TD, c) ufg Ni RD, d) mc Ni.

In order to explain the slightly deteriorated FCG behavior of ufg Ni with TD orientation it is obvious from the previous explanations that dislocation activity has to be taken into account. It is essential to compare the grain size to the size of the cyclic plastic zone (CPZ) to understand the influence of the microstructure on the cyclic deformation process. The size of the CPZ was estimated for plane strain conditions [40]:

$$r_{CPZ} = \frac{1}{3\pi}\left(\frac{\Delta K_I}{2\sigma_y}\right)^2 \tag{5}$$

A comparison of the grain sizes and the size of the CPZ for low and high ΔK is given in table B-6. In the near-threshold region the size of the CPZ is in the order of the grain size for nc and ufg Ni and thus the discrete nature of plasticity has to be considered. In ufg Ni the CPZ size is marginally smaller than the smallest grain dimension. Thus, during loading dislocations in general only glide to the next grain boundary, where they get preferentially blocked. This dislocation pile-up exerts a backstress, which causes a larger number of dislocations to return to the crack during unloading than without this dislocation pile-up. Hence, at smaller ΔK dislocations will move back and a larger number of dislocations will return to the crack tip. This

results in faster fatigue crack growth in ufg Ni near the threshold. In nc Ni the CPZ at ΔK_{th} is larger than the grain size. This means that in general dislocation activity can be found in various grains around the crack tip. However, at the threshold only dislocations from the grains adjacent to the crack tip can glide back to the crack during unloading. In other words, fewer dislocations than in ufg Ni return to the crack. This could be the reason for the higher ΔK_{th} of nc Ni.

Table B-6: Comparison of the grain size and the cyclic plastic zone size r_{cp} estimated with Eq. 5 for ΔK_{th} at R=0.7 and for ΔK=13 MPa $m^{0.5}$.

	ΔK_{th} [MPa $m^{0.5}$]	Grain size [µm]	r_{CPZ} at ΔK_{th} [µm]	r_{CPZ} at ΔK = 13 MPa $m^{0.5}$ [µm]
nc Ni	2.0	0.03	0.07	3.11
ufg Ni TD	1.7	0.25–0.75	0.12	7.00
ufg Ni RD	2.2	0.25–0.75	0.21	7.00
mc Ni	2.8	50	1.40	71.58

In the mid- and upper Paris regime the CPZ get substantially larger than the grain sizes of nc and ufg Ni and thus continuum mechanical properties, like the yield strength, determine FCG [41]. When blunting and re-sharpening is assumed to be the dominant FCG process, the relation between FCG rate da/dN, cyclic crack tip opening displacement ΔCTOD, yield strength σ_y and Young's modulus E for a given stress intensity factor range ΔK can be expressed as:

$$\frac{da}{dN} \propto \Delta CTOD \propto \frac{\Delta K^2}{\sigma_y * E} \tag{6}$$

From Eq. (6) it can be seen that a larger yield strength leads to a smaller cyclic crack tip opening displacement and therefore to a smaller crack growth per cycle due to geometric reasons. Thus, at a given ΔK an increase of the yield strength would predict a decrease in the FCG rate. Therefore the slower FCG of nc Ni in the Paris regime can be attributed to its higher yield strength.

B.4.4 What is the reason for the differences between very fine-grained (nc and ufg) Ni and mc Ni with respect to the FCG threshold and the FCG rate?

Nc and ufg Ni show similarities in their FCG behavior, including no marked influence of the load ratio, missing R-curve behavior of the threshold of stress intensity range and Paris exponents m of about 2. For the FCG behavior of mc Ni some distinct differences were observed. It was shown in section 3.1.1 that FCG in mc Ni shows a clear dependence on the load ratio and R-curve behavior for ΔK_{th}. This appears plausible, as in Ni with a grain size of about 50µm active roughness and plasticity induced crack closure, as well as crack deflection is expected from classical models [18, 34, 37]. A comparison of FCG data of mc, ufg and nc Ni, measured at R=0.7, where the contribution of crack closure should be small, gives the following differences: Mc Ni shows a higher ΔK_{th} with lower FCG rates at low ΔK, a larger slope m of about 4 in the low Paris region and therefore faster FCG rates at higher ΔK compared to nc and ufg Ni. Furthermore mc Ni specimens show a mixture of inter- and transcrystalline fracture in the near-threshold region (Fig. B-5a) and almost exclusively intercrystalline fracture at higher loads (Fig. B-5b). This is in contrast to the very fine-grained Ni samples (ufg and nc Ni) where exclusively intercrystalline fracture was observed at all ΔK (Fig. B-5c-d, Fig B-6). However, in regions with intercrystalline fracture steps from slip bands were observed, which

can also be seen in nc and ufg Ni. Thus it is clear that plastic deformation controls also the FCG in mc Ni and therefore the differences in dislocation motion must be responsible for the distinct FCG behavior of mc Ni.

For mc Ni the size of the cyclic and monotonic plastic zone region is substantially smaller than the grain size in the near threshold, see table B-6. Dislocation motion is therefore easier in mc Ni than in nc and ufg Ni because in general dislocations generated at the crack tip can glide freely in the large grains. In mc Ni dislocations in general do not reach grain boundaries at ΔK_{th} and so crack growth exclusively along the grain boundaries, like observed in ufg and nc Ni, is improbable. Thus, the cracks have to grow through the grains in a transcrystalline way. In experiments with nc and ufg Ni it was seen that cracks preferentially grow along the grain boundaries, which serve as a weak crack path. Therefore it is not surprising that there is a higher resistance against transcrystalline crack growth. As a consequence for mc Ni a 27% higher ΔK_{th} was measured than for ufg Ni with TD orientation. In the near-threshold region intercrystalline fracture is only possible if the crack tip is close to a grain boundary. The crack follows then preferably grain boundaries and only changes to a transcrystalline fracture mode if grain boundaries are unfavorably aligned to the present loading. In the Paris region, where the load is large enough to have a CPZ size in the order or larger than the grain size, almost exclusively intercrystalline fracture is observed. In this case the situation in mc Ni is the same as in the very fine-grained structures, where dislocations can reach grain boundaries more easily. Mc Ni shows a steeper slope in the FCG data (exponent m of about 4) than ufg and nc Ni. A steeper slope could mean that FCG is not mainly controlled by plasticity but by other damage mechanisms like damage accumulation. However, it is also possible that even at ΔK = 10 MPa.m$^{0.5}$ mc Ni is still in the transition to the Paris regime and thus the FCG curve shows a steeper slope. This assumption is supported by fatigue crack propagation simulation by means of a discrete dislocation technique [17], which shows that in coarse-grained or low strength materials an extended transition region from the threshold to the Paris regime occurs. In this case it would be expected that FCG experiments on mc Ni at higher ΔK would again show an exponent of 2, as for high loads the same fracture mechanisms were observed in the fracture surface analysis of mc Ni like in ufg and nc Ni. Unfortunately it is difficult to conduct FCG experiments on mc Ni in this load range because very large specimens are needed in order to stay within the limitations of linear elastic fracture mechanics due to the low yield strength of mc Ni.

It seems also possible that grain boundaries in mc Ni are additionally embrittled because compared to ufg Ni the same amount of impurities would be distributed on a much smaller internal grain boundary area. This could lead to brittle crack propagation by grain boundary de-cohesion, e.g. caused by sulfur embrittlement [38]. However, slip steps are also observed on the grain boundaries in regions with intercrystalline fracture of mc Ni as described before. Therefore, we assume that in mc Ni also FCG due to a blunting process plays the major role and not cyclic brittle failure because of grain boundary embrittlement. This is further proven by inspecting the overload fracture of tested specimens. All tested samples show a transition from intercrystalline FCG to ductile overload fracture. An example is given in Fig. B-10 for ufg Ni. The observed formation of pores and plastic necking clearly shows that ductile failure occurs.

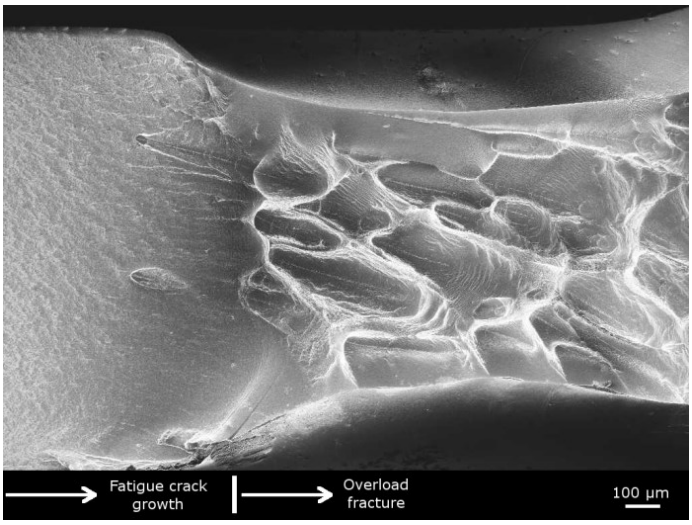

Fig. B-10: SEM image of the fracture surface of an ufg Ni FCG specimen showing the transition from intercrystalline FCG (on the left) to ductile overload fracture. The ductile nature of the overload fracture can be seen by the formation of pores and clear plastic necking.

In contrast to the findings of the present study, Hanlon et al. attributed a large part of the differences in the FCG curves of Ni with different grain sizes to the effect of roughness induced crack closure, which gets larger for coarser-grained materials. Furthermore they observed a clear influence of the load ratio on the FCG behavior of nc and ufg Ni [13]. For that study thin specimens were used with a thickness of 100µm and therefore plane stress conditions must have been prevailing, especially in the Paris regime. However, the results of Hanlon et al. [13] might be caused by the explanations given in the previous sections. For that, according to section 4.1, it could be assumed that no pronounced effect of roughness induced crack closure exists in nc and ufg Ni. Due to the prevailing plane stress condition in the thin samples PICC could be active because of the out-of-plane plastic flow - despite the occurrence of grain coarsening. This would explain the influence of the load ratio on the FCG behavior. Due to the effect of the yield strength, PICC is larger in mc Ni samples than in ufg Ni and larger in ufg Ni than in nc Ni. Therefore it seems that explanations based on differences in dislocation motion given in this work would also be capable of describing the results of [13].

B.5 Conclusion

In this study the fatigue crack growth behavior of high purity nickel with different grain sizes, spanning from microcrystalline to nanocrystalline states, were investigated. The main findings can be summarized as follows:

(i) It was found that in high purity Ni fatigue crack growth is controlled by dislocation motion, i.e. by a blunting and re-sharping process. Grain boundaries serve as weak crack paths, resulting in intercrystalline fracture when the size of the cyclic plastic zone is in the order of the grain size

(ii) Nc and ufg Ni is insensitive to changes of the load ratio because the contribution of oxide-, plasticity- and roughness-induced crack closure is negligible. No significant influence of oxide-induced crack closure is expected as no oxide debris were observed. Changes in the amount of stored dislocations in the wake of the crack due to grain coarsening lead to a decrease of plasticity-induced crack closure. Small mode II displacements of the crack faces result in a diminishing roughness induced crack closure, even if fracture surfaces exhibit a high roughness.

(iii) The FCG behavior of ufg Ni produced by HPT shows strong orientation dependence due to grain elongation induced by the shear deformation of the HPT processing. Grain orientations unfavorable for crack growth (e.g. a crack growth direction perpendicular to the elongated grains) can considerably increase the overall resistance against FCG growth due to regular crack deflections.

(iv) Nc Ni shows a slightly enhanced FCG behavior compared to ufg Ni with TD orientation, with a higher ΔK_{th} and lower FCG rates. In the near-threshold regime the difference can be related to the ratio of the cyclic plastic zone to the grain size. In the Paris regime the strength determines the variation in the FCG rate, due to the change of the cyclic crack tip opening displacement.

(v) For mc Ni a higher ΔK is needed for first crack propagation (higher ΔK_{th}) because the crack is forced to propagate in a transcrystalline way due to the small size of the cyclic plastic zone compared to the large grain size. However, at high ΔK faster fatigue crack propagation was observed in mc Ni than in the finer-grained Ni as a consequence of the lower yield strength.

(vi) A re-introduction of closure mechanisms, e.g. plasticity-induced crack closure by stabilizing the microstructure, and a specific alignment of the microstructure, i.e. grains elongated perpendicular to the expected crack growth directions, could enhance the FCG behavior. This could make these high strength materials more interesting for cyclic applications where damage tolerance is of importance.

B.6 References

[1] K.S. Kumar, S. Suresh, M.F. Chisholm, J.A. Horton, P. Wang, Deformation of electrodeposited nanocrystalline nickel, Acta Mater. 51 (2003) 387–405.

[2] R. Valiev, R. Islamgaliev, I. Alexandrov, Bulk nanostructured materials from severe plastic deformation, Prog. Mater. Sci. 45 (2000) 103–189.

[3] A. Zhilyaev, T. Langdon, Using high-pressure torsion for metal processing: Fundamentals and applications, Prog. Mater. Sci. 53 (2008) 893–979.

[4] C. Koch, Optimization of strength and ductility in nanocrystalline and ultrafine grained metals, Scr. Mater. 49 (2003) 657–662.

[5] Y. Wang, M. Chen, F. Zhou, E. Ma, High tensile ductility in a nanostructured metal, Nature 419 (2002) 912–915.

[6] I. Sabirov, Y. Estrin, M.R. Barnett, I. Timokhina, P.D. Hodgson, Tensile deformation of an ultrafine-grained aluminium alloy: Micro shear banding and grain boundary sliding, Acta Mater. 56 (2008) 2223–2230.

[7] M. Faleschini, H. Kreuzer, D. Kiener, R. Pippan, Fracture toughness investigations of tungsten alloys and SPD tungsten alloys, J. Nucl. Mater. 367-370 (2007) 800–805.

[8] A. Hohenwarter, R. Pippan, Fracture toughness evaluation of ultrafine-grained nickel, Scr. Mater. 64 (2011) 982–985.

[9] A. Hohenwarter, R. Pippan, Anisotropic fracture behavior of ultrafine-grained iron, Mater. Sci. Eng. A 527 (2010) 2649–2656.

[10] T. Hanlon, Y.-N. Kwon, S. Suresh, Grain size effects on the fatigue response of nanocrystalline metals, Scr. Mater. 49 (2003) 675–680.

[11] H. Bomas, H.W. Höppel, M. Kautz, C. Xu, M. Murashkin, T.G. Langdon, et al., An overview: Fatigue behaviour of ultrafine-grained metals and alloys, Int. J. Fatigue 28 (2006) 1001–1010.

[12] P. Cavaliere, Fatigue properties and crack behavior of ultra-fine and nanocrystalline pure metals, Int. J. Fatigue 31 (2009) 1476–1489.
[13] T. Hanlon, E. Tabachnikova, S. Suresh, Fatigue behavior of nanocrystalline metals and alloys, Int. J. Fatigue. 27 (2005) 1147–1158.
[14] H.A. Padilla, B.L. Boyce, A review of fatigue behavior in nanocrystalline metals, Exp. Mech. 50 (2009) 5–23.
[15] K. Hockauf, M. Hockauf, M.F.-X. Wagner, T. Lampke, T. Halle, Fatigue crack propagation in an ECAP-processed aluminium alloy - influence of shear plane orientation, Materwiss. Werksttech. 43 (2012) 609–616.
[16] R.O. Ritchie, Mechanisms of fatigue crack propagation in metals, ceramics and composites: Role of crack tip shielding, Mater. Sci. Eng. A 103 (1988) 15–28.
[17] R. Pippan, C. Zelger, E. Gach, C. Bichler, H. Weinhandl, On the mechanism of fatigue crack propagation in ductile metallic materials, Fat. Fract. Eng. Mat. Struct 34 (2010) 1-16
[18] S. Suresh, Fatigue of Materials, second ed., Cambridge University Press, 2000.
[19] B. Yang, Grain size effects on the mechanical behaviour of polycrystalline nickel from micro to nanoscale, PhD thesis, Materwiss. Werksttech. 8 (2006).
[20] B. Yang, Influence of annealing on the microstructure and mechanical properties of electrodeposited nanocrystalline nickel, Mat. Sci. Forum 683 (2011) 103-112.
[21] G.B. Rathmayr, R. Pippan, Influence of impurities and deformation temperature on the saturation microstructure and ductility of HPT-deformed nickel, Acta Mater. 59 (2011) 7228–7240.
[22] G.B. Rathmayr, A. Hohenwarter, R. Pippan, Influence of grain shape and orientation on the mechanical properties of high pressure torsion deformed nickel, Mater. Sci. Eng. A 560 (2013) 224–231.
[23] D.C. Meeker, Finite Element Method Magnetics, Version 4.0.1, http://www.femm.info
[24] R.A. Smith, Calibration for the electrical potential method of crack growth by a direct electrical analogy, Strain 10 (1974) 183-187
[25] R. Pippan, H.P. Stüwe, K. Golos, A comparison of different methods to determine the threshold of fatigue crack propagation, Fatigue16 (1994) 579-582.
[26] ASTM E-399-90, Annual Book of ASTM Standards, American Society of Testing and Materials, Philadelphia (PA), 1990.
[27] ASTM E 647-13a, Annual Book of ASTM Standards, American Society of Testing and Materials, Philadelphia (PA), Vol. 03.01., 2013.
[28] J. Stampfl, S. Scherer, M. Gruber, O. Kolednik, Reconstruction of surface topographies by scanning electron microscopy for application in fracture research, Applied Physics A: Mat. Sci. Proc. 63 (1996) 341-346.
[29] R. Pippan, L. Plöchl, F. Klanner, H.P. Stüwe, The use of fatigue specimens precracked in compression for measuring threshold values and crack growth, J. Test. Eval. 22 (1994) 98-103.
[30] S. C. Forth, D. J. Herman, M. A. James, W. M. Johnston, Fatigue crack growth rate and stress-intensity factor corrections for out-of-plane crack growth, ASTM JAI 2 (2005) 124-137.
[31] R. Pippan, G. Strobl, H. Kreuzer, C. Motz, Asymmetric crack wake plasticity – a reason for roughness induced crack closure, Acta Mat. 52 (2004) 4493-4502.
[32] J. Pokluda, R. Pippan, Analysis of roughness-induced crack closure based on asymmetric crack-wake plasticity and size ratio effect, Mat. Sci. Eng. A 462 (2007) 355-358.
[33] B. Budiansky, J.W. Hutchinson, Analysis of closure in fatigue crack growth, J. Appl. Mech. 45 (1978) 267-276.

[34] F.O. Riemelmoser, R. Pippan, Crack Closure: A concept of fatigue crack growth under examination, Fat. Fract. Eng. Mat. Struct. 20 (1997) 1529-1540.
[35] R. Pippan, F.O. Riemelmoser, Modeling of fatigue crack growth: dislocation models, Comprehensive Structural Integrity 4 (2003) 191-207.
[36] H. Mughrabi, H.W. Höppel, Cyclic deformation and fatigue properties of very fine-grained metals and alloys, Int. J. Fatigue 32 (2010) 1413–1427.
[37] S. Suresh, Fatigue crack deflection and fracture surface contact: Micromechanical models, Met. Trans. A 16 (1985) 249–260.
[38] T.E. Buchheit, S.H. Goods, P.G. Kotula, P.F. Hlava, Electrodeposited 80Ni–20Fe (Permalloy) as a structural material for high aspect ratio microfabrication, Mater. Sci. Eng. A 432 (2006) 149–157.
[39] F.O. Riemelmoser, R. Pippan, H.P. Stüwe, An argument for a cycle-by-cycle propagation of fatigue cracks at small stress intensity ranges, Acta Mater. 46 (1998) 1793–1799.
[40] G.R. Irwin, Plastic zone near a crack and fracture toughness, Proc. Seventh Sagamore Ordnance Materials Conference 4 (1960) 63-78.
[41] R. Pippan, F.O. Riemelmoser, H. Kreuzer, Effect of the discrete nature of plasticity on fatigue crack propagation, J. Phys. IV France 11 (2001) 77-84.

C Fatigue crack growth anisotropy in ultrafine-grained iron

Thomas Leitner [1*], Anton Hohenwarter [1], Walter Ochensberger [2], Reinhard Pippan [2]

[1] Department of Materials Physics, Montanuniversität Leoben, Austria

[2] Erich Schmid Institute of Materials Science, Austrian Academy of Sciences, Leoben, Austria

Abstract

Nanocrystalline and ultrafine-grained (UFG) metals produced by severe plastic deformation exhibit often microstructures with elongated grains, which result in orientation dependent mechanical properties. This anisotropy is especially pronounced for the resistance against quasi-static and cyclic crack growth. In order to gain more knowledge about the consequences of anisotropic microstructures in the case of cyclic loading, fatigue crack growth (FCG) experiments were performed on UFG iron processed by high pressure torsion, with a mean grain size of 500 x 400 x 150 nm^3. Samples with four different orientations were prepared and tested with two mean stresses to account for crack closure effects. The FCG rate varies by one order of magnitude between cracks propagating parallel to elongated grains and cracks advancing perpendicular to it. This larger difference is discussed in the light of intrinsic and extrinsic toughening mechanisms. It is concluded that crack closure contributions are reduced in UFG Fe, however, geometric shielding due to more frequently occurring crack branching leads to a significantly higher FCG resistance for cracks perpendicular to the grain elongation. Furthermore, it is observed that grain refinement leads to a transition from transgranular to intergranular fracture. However, it can be shown that this intergranular crack growth of UFG iron under cyclic loading is not the result of grain boundary embrittlement, but occurs due to a blunting and re-sharpening process along the grain boundaries.

C.1 Introduction

Ultrafine-grained (UFG) and nanocrystalline (NC) metals, i.e. metals with grain sizes below 1 μm and 100 nm respectively, show various improved mechanical properties compared to microcrystalline (MC) counterparts and have been the topic of a large number of studies in recent years [1–4]. Besides electrodeposition, mechanical alloying and gas-phase condensation, severe plastic deformation (SPD) can be applied to obtain NC and UFG metals. With SPD methods the grain refinement is achieved by the introduction of large plastic strains, which reduces the grain size until an equilibrium between grain fragmentation and restoration processes is reached. Metals processed by SPD methods have in common that in many cases the developing microstructure exhibits elongated grains [5–7] which results in anisotropic mechanical properties [8–12]. This is especially the case for a number of continuous SPD techniques which are able to produce larger volumes of materials and thus are of great interest for industry, as for example accumulative roll bonding (ARB), continuous confined strip shearing (C2S2) and the equal channel angular pressing (ECAP) conform method [13–15]. With other methods, such as high pressure torsion (HPT) and ECAP, the processed material volumes are small, however, comparable features evolve [5–7]. Smaller-sized samples make it possible to conduct a larger number of fundamental studies on these materials by changing process parameters, like the applied shear strain, strain rate and deformation temperature. Especially with HPT a large variety of materials can be processed due to the high hydrostatic pressure, which allows investigations even on high strength and brittle metals. However, elongated grains are also characteristic for NC metals produced by other techniques, like electrodeposition.

Anisotropic microstructures lead to orientation dependent mechanical properties, especially concerning the resistance against static and cyclic crack growth, which is well known from bio materials [16]. In principle, the anisotropy of the mechanical properties is not a drawback and, as in nature, can be used as toughening strategy. For example, fracture toughness was found to be relatively low for cracks introduced parallel to elongated grains [8–10]. However, the existence of this weak crack path leads to a significantly enhanced crack growth resistance for crack propagation perpendicular to the elongated grains [8–10]. For example, fracture experiments on HPT deformed UFG ARMCO Fe revealed that the fracture toughness of cracks oriented perpendicular to the shear plane of the HPT process is about 3.5 times higher than the fracture toughness of cracks parallel to it (49.0 $MPa.m^{0.5}$ for perpendicular cracks, 14.2 $MPa.m^{0.5}$ for parallel cracks) [9][11][11]. The same behavior has been found for crack propagation under cyclic loading for UFG Ni produced by HPT, where a significantly higher fatigue crack growth (FCG) resistance was measured for cracks perpendicular to the grain elongation direction, compared to cracks parallel to the elongated grains [12].In order to improve the understanding of the effect of grain shape on the FCG resistance in UFG and NC metals, FCG tests were performed on HPT deformed UFG iron as a representative of body-centered cubic structures, with various different sample orientations. The experimental results are discussed with focus on intrinsic and extrinsic toughening mechanisms and the role of crack closure and crack tip shielding.

C.2 Material and experimental methods

In this study ARMCO-iron with the composition given in Table 1 was used as a model material for bcc metals. Discs with 30 mm diameter and 7.5 mm height were subjected to HPT at room temperature at a nominal pressure of 2.8 GPa for 10 rotations, which yields a von Mises strain of ε_{vM}~ 70 at a radius of 15 mm. The grain size of the as-received and HPT deformed microstructure was determined by electron backscatter diffraction (EBSD) in the scanning electron microscope (SEM), see Fig. C-1. The as-received microcrystalline

Fe exhibits equiaxed grains with a mean grain size of ~ 15 µm (Fig. C-1(a)). As can be seen in Fig. C-1(b), HPT deformation results in a microstructure with grains elongated in the shear direction of the process, with the shortest grain length parallel to the axial direction. The elongated grains are furthermore slightly tilted to the shear plane by about 20°. The grain dimensions are approximately 500 x 400 x 150 nm³, or about 310 nm in diameter for globular grains with an equivalent volume, i.e. microstructure consists of pancake-shaped grains. EBSD images of UFG Fe with different viewing directions are projected on a cube in Fig. C-1(c) to provide a better visualization of the microstructure.

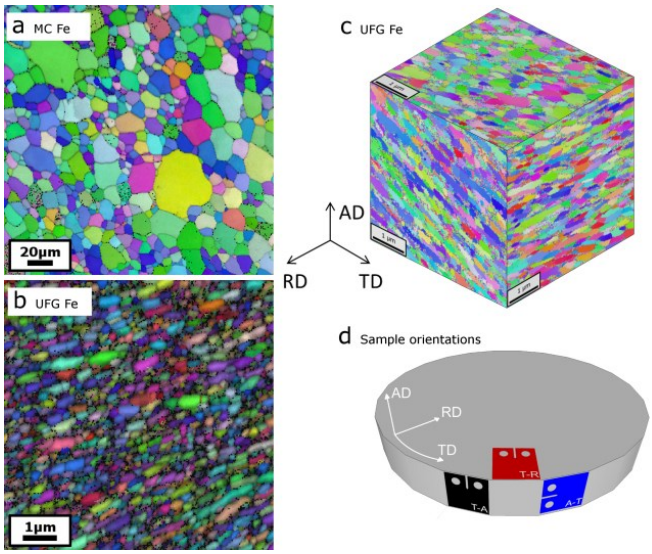

Fig. C-1: SEM images of the microstructure of a MC Fe (a) and the UFG Fe (b,c) derived from EBSD analyses. In (c) EBSD images are projected on a cube to better visualize the elongation of the grains in tangential direction of the HPT disc. (d) shows the orientation of the different specimen types in the HPT disc.

The substantial grain-refinement was accompanied by a hardness increase from 95 HV in the as-received state to 410 HV in the HPT-deformed state (see Table C-1), which was measured between a radius of 2 and 15 mm of the HPT disc. Yield strengths were estimated with the Tabor rule ($\sigma_y \approx 3 * H * 1\ MPa/HV$) [17], which are in good agreement with the measured strength of a similarly HPT deformed pure Fe [9].

Table C-1: Material properties of MC and UFG Fe, including the grain size, d_m, hardness H and yield strength σ_y.

	MC Fe	UFG Fe
Production route	as-received	High pressure torsion
d_m	15 µm	500 x 400 x 150 nm³
H	95 HV	410 HV
σ_y *	285 MPa	1230 MPa
Composition	0.009 wt% C, 0.060 wt% Mn, 0.009 wt% P, 0.007 wt% S, balance Fe	

Compact-tension specimens were produced from the HPT deformed material, with W=5.4 mm, B=1.3 mm and a=1.0 – 1.3 mm. The notches were introduced by a diamond wire saw and further sharpened to a radius of 5-30 µm by razor blade grinding. Cyclic compression loading (R=10) with a resonance testing machine (Rumul Russenberger + Müller, Switzerland) was used to create short and open fatigue pre-cracks, which allow to start the experiments with crack-closure free conditions [18]. For the analysis of the FCG anisotropy, samples were taken with three different orientations in respect to the HPT process. The nomenclature of the specimens was chosen according to the standard E399 [19], with the first letter indicating

the normal direction of the crack plane and the second letter indicating the direction of the crack growth. The directions axial (A), radial (R) and tangential (T) refer to the geometry of the HPT deformed disc and are depicted in Fig. C-1(d). As shown in Fig. C-1(d), four different sample orientations (T-A, R-A, T-R and A-T) were prepared and tested.

An electrodynamic testing instrument, Instron ElectroPuls™, with a 250 N load cell was used for the cyclic loading of the samples. The specimens were tested with a sinusoidal force and a frequency of 45 Hz at load ratios of R=0.1 and R=0.7. The potential drop technique (PDT) was used to measure the crack length in-situ during the FCG test. More details about the PDT can be found elsewhere [12]. The effective threshold stress intensity factor range $\Delta K_{th,eff}$ was determined with the load rising method [18], where the experiments were started at a low ΔK (1.5 MPa.m$^{0.5}$) and step-wise increased (0.2 MPa.m$^{0.5}$ increment size) until the first crack growth is detected. $\Delta K_{th,eff}$ lies between this and the previous ΔK level. If the crack growth decelerates and stops, which means that the material shows cyclic R-curve behavior and crack closure or other shielding mechanisms have built up, the load is increased for a further increment of 0.2 MPa.m$^{0.5}$. When ΔK is equal or larger than the threshold stress intensity factor range of a long crack ΔK_{th}, the crack propagates without stopping until failure.[2] Following the standard E647 [20], small partitions of the crack length and cycle number data were repeatedly fitted by a polynomial function of second order and the derivative calculated to get the FCG rate da/dN. The tests were stopped before the samples failed by overload fracture. The final crack length was measured optically and the value compared to the crack length determined from the PDT. Finally, the samples were cyclically loaded until failure.

After the FCG tests images of the samples were examined with a field emission gun SEM "LEO Gemini 1525". The crack path was inspected on the side faces of the specimens at different crack lengths and hence at different ΔK values and quantitative roughness parameters were calculated from SEM images. The true and the projected length was measured from these profiles and the linear roughness parameter determined by R_L=*(true length)/(projected length)*. Furthermore the maximum roughness amplitude of the profile was measured and the arithmetic average of the absolute values R_a calculated. The crack profiles were subdivided into 100 nm long segments and the deflection angles from the straight crack path measured.

C.2.1 Validity of FCG data

Due to the limited size of HPT discs the CT samples used in this study are smaller than the minimum recommendations of ASTM E647 [20], with W=5.4 mm. Therefore additional care has to be taken that linear elastic fracture mechanics (LEFM) is applicable and that plane strain conditions prevail to allow a comparison of FCG data. Hence, data can only be taken as valid when the maximum size of the plastic zone is small compared to the un-cracked ligament and the thickness of the samples. The size of the monotonic plastic zone was calculated for plane strain conditions with [21]:

$$r_{pl} = \frac{1}{3\pi}\left(\frac{K_I}{\sigma_y}\right)^2 \tag{1}$$

The standard for fracture toughness testing, E399 [19] recommends an uncracked ligament and a specimen thickness larger than about 25 times the plastic zone size. For a typical maximum crack length of a=3 mm and

[2] The quantities can also be named as the short-crack threshold $\Delta K_{th,eff}$ and the long-crack threshold ΔK_{th}. With the load shedding procedure only the long-crack threshold can be determined.

the estimated yield strength of UFG Fe σ_y Equ. 1 yields that K_{max} must be smaller than 37.0 MPa.m$^{0.5}$, which is fulfilled for tests at R=0.1 up to a ΔK of 33.3 MPa.m$^{0.5}$, and for R=0.7 up to a ΔK of 11.1 MPa.m$^{0.5}$. A more severe limitation, however, arises from the requirement for the prevalence plain strain conditions. For the nominal sample thickness of B=1.35 mm the stress intensity factor range ΔK must be smaller than 25.0 MPa.m$^{0.5}$ and 8.3 MPa.m$^{0.5}$, for R=0.1 and R=0.7 respectively. In the following sections only FCG data within these limits are shown and discussed.

A further requirement for valid FCG data from E647 is that cracks do not deflect more than ±20° from the plane of symmetry [20]. As will be seen in the results section, this is not the case for all crack orientations. Therefore, finite element simulations were performed in order to study the effect of larger deflection angles on the crack driving force. The numerical results demonstrate that even deviations larger than 20° have only small effects on the calculated ΔK values, as long as the crack extension is short. Further details and results of the FE modeling can be found in the supplementary material.

C.3 Results

C.3.1 Crack paths

Fatigue cracks show deviations from their designated paths for all tested orientations in UFG Fe, see Fig. C-2. In T-A specimens cracks immediately deflect to about 75° from the direction of the notch. In R-A samples the crack starts to grow under a small angle to the straight crack path but continuously changes its direction to a final deflection of about 75°. This strong deviation from the straight crack path changes the loading conditions and strongly affects the ΔK_I and crack length calculations, so that no reliable FCG data could be obtained for this orientation. For comparison, only ΔK_{th} has been taken as valid, as deviations are small during the first crack advance. Therefore, comparisons of the FCG curves are limited to the other two orientations (A-T and T-R samples) in the rest of the study. Despite this, the R-A orientation is interesting for the design, because under these loading conditions the crack barely reduces the cross-section of a component. In A-T specimens the deflection is less pronounced (about 10°) but almost coincides with the crack growth direction of T-A specimens, when their orientation in respect to the HPT disc is taken into account, see also Fig. C-3. In T-R samples the cracks continuously change their direction from 5° to about 80°. Furthermore the crack planes get tilted towards the shear plane of the HPT disc. From these observations crack propagation in tangential direction on a plane 10° inclined to the shear plane of the HPT process seems to be favorable. This preferred crack path is in good accordance with the orientation of the elongated grains of the HPT microstructure. From Fig. C-3 it can be seen that all fatigue cracks in HPT deformed Fe, regardless of the orientation of the samples, tend to change their direction until they can follow the direction of the elongated grains.

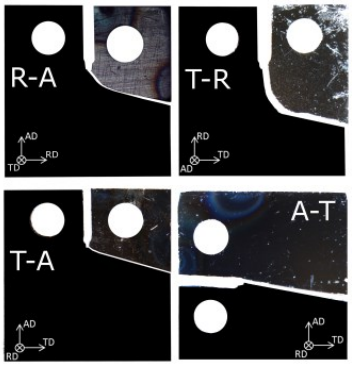

Fig. C-2: Illustration of the macroscopic fatigue crack paths in R-A, T-R, T-A and A-T specimens.

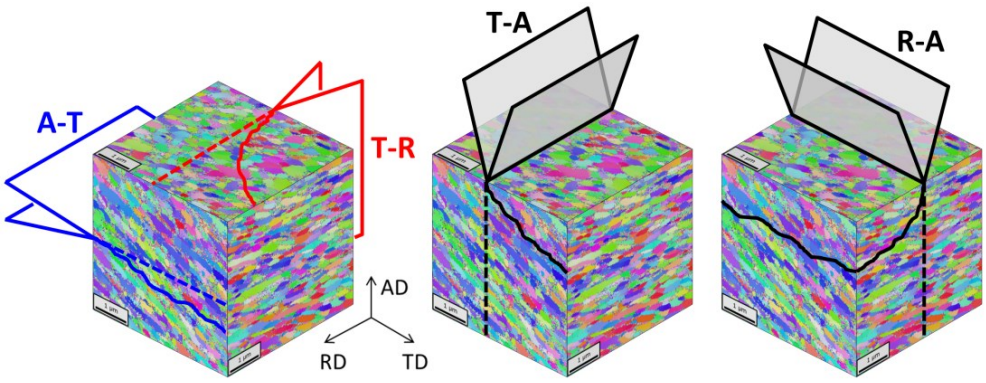

Fig. C-3: Schematic of the crack growth planes and directions of A-T, T-R, T-A and R-A samples. The wedges show the notch orientation and the dashed lines the designated crack growth direction. Solid wavy lines illustrate the observed crack paths.

Examples of the crack paths analyzed in the SEM are shown for ΔK=5.7 MPa.m$^{0.5}$ in Fig. C-4(a) and (b) for UFG Fe A-T and T-R, respectively. Microscopically, it can be seen from Fig. C-4(a) and (b) that fatigue cracks propagating in radial direction (T-R orientation) exhibit more pronounced deflections than cracks in tangential direction (A-T). In UFG T-R samples frequent crack branching occurs, even though these branches stop to grow after short distances and the main crack continuous to follow the designated Mode I direction. In contrast, hardly any crack branching is visible in the crack path of A-T specimens. The quantitatively determined roughness parameters are listed in Table C-2 and confirm the large differences in roughness for the two orientations.

Table C-2: Linear roughness parameter RL=(true length)/(projected length), arithmetic average of the absolute values Ra and maximum roughness amplitude of the profiles shown in Fig. C-4(a) and (b) for the orientations A-T and T-R.

	A-T	T-R
R_L	1.08	1.77
R_a	28 nm	125 nm
Max - Min	168 nm	624 nm

As visible from the deflection angle histograms in Fig. C-4(c) and (d), fatigue cracks in tangential direction exhibit only small direction changes, with the majority of the segments deviating less than ± 15° and at maximum ± 40°. On the contrary, cracks in radial direction show a wider distribution of the deflection angles of the crack path segments (up to ± 70°).

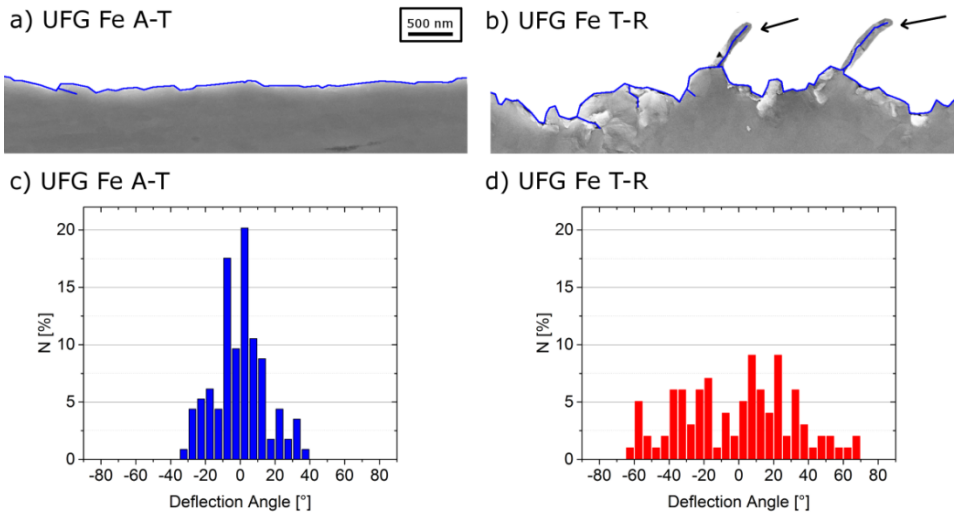

Fig. C-4: (a) and (b) show parts of the crack paths of UFG Fe A-T and T-R samples at ΔK=5.7 MPa.m$^{0.5}$. Cracks in the T-R orientation show frequent crack branching; two examples are marked by arrows in (b). In (c) and (d) histograms of the deflection angle of the cracks are given.

C.3.2 FCG data of UFG Fe

The FCG data of UFG Fe specimens with T-R, A-T and R-A orientation is shown in Fig. C-5. Threshold stress intensity factor ranges ΔK_{th} of the different orientations are listed in Table C-3. From experiments at R=0.1 (open symbols) and R=0.7 (filled symbols) for T-R, A-T and R-A samples it can be seen that only a weak stress-ratio dependency is observed. FCG tests at both R-ratios yield comparable results for each orientation, with only somewhat lower ΔK_{th} and slightly higher FCG rates at R=0.7. Differences in ΔK_{th} between T-R, A-T and R-A oriented specimens are small, with a tendency of lower ΔK_{th} for A-T (see Table C-3).

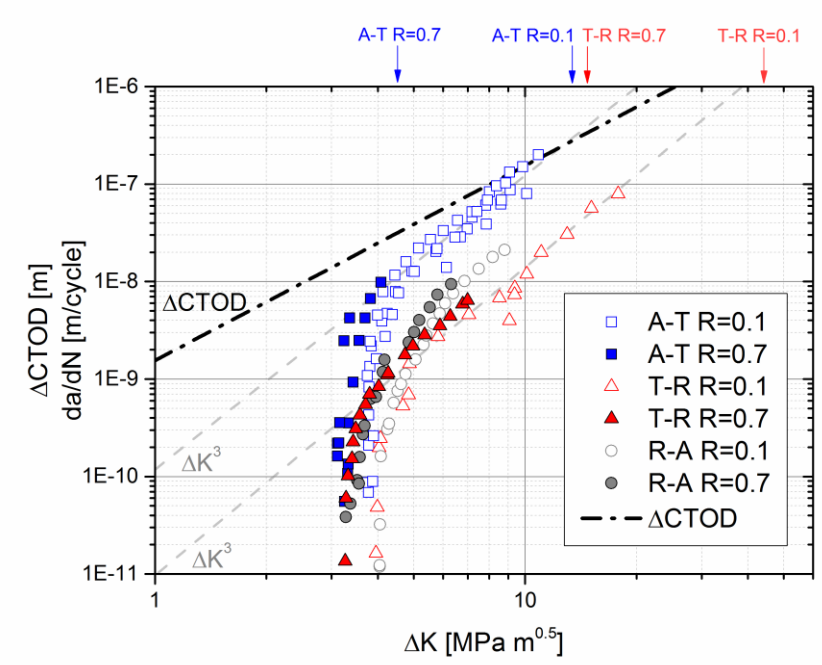

Fig. C-5: FCG curves of UFG Fe with A-T, T-R and R-A orientations, measured at R=0.1 and R=0.7. The dashed gray lines are ΔK^3 guidelines, which have the same slope as the measured data in the Paris regime. The black dash-dotted line shows the calculated $\Delta CTOD$ values for UFG Fe with d_n=0.78. The upper limits of the FCG curves are indicated by arrows on top of the diagram for both orientations at R=0.1 and R=0.7. At these ΔK the maximum stress intensities, K_{max}, correspond to the fracture toughness of the respective orientation, which was measured in [9].

For the T-A sample a more than 40 % higher ΔK_{th} was measured than for the other orientations (Table C-3). Data in the Paris regime was fitted to the Paris equation (Equ. 2), to evaluate the coefficient C and exponent m of the Paris relation for A-T and T-R samples.

$$\frac{da}{dN} = C * \Delta K^m \tag{2}$$

For both orientations, independent of the R-ratio, curve fitting gives values close to 3 for the exponent m (listed in Table C-4). This is in good accordance to the observation that ΔK^3 guidelines, shown in the FCG diagrams (Fig. C-5) fit the FCG curves in the Paris region well. For a better comparison of the coefficients C, data in the Paris regime was fitted again for a fixed m of 3. This yields an approximately 10 times higher C value for samples with A-T orientation compared to T-R samples, indicating a 10 times higher FCG rate and thus a lower FCG resistance.

Table C-3: Threshold stress intensity factor ranges of UFG Fe with different orientations, measured at R=0.1 and R=0.7.

	R=0.1 ΔK_{th} MPa m$^{0.5}$	R=0.7 ΔK_{th} MPa m$^{0.5}$
UFG Fe A-T	3.7	3.1
UFG Fe T-R	4.0	3.3
UFG Fe R-A	4.0	3.3
UFG Fe T-A	5.6	-

Table C-4: Fitted Paris coefficients C and exponents m for UFG Fe with T-R and A-T orientation.

	m	C	C fitted for m=3
UFG Fe T-R	3.1 ± 0.2	$1.0*10^{-11}$ ± $0.5*10^{-11}$	$1.4*10^{-11}$ ± $0.04*10^{-11}$
UFG Fe A-T	3.3 ± 0.1	$7.7*10^{-11}$ ± $1.9*10^{-11}$	$15.1*10^{-11}$ ± $0.3*10^{-11}$

Error estimation shows that the effect of measurement errors on the FCG curves is small and thus the FCG results and relations discussed in this paper are significant. More details can be found in section 2 of the supplementary material.

C.3.3 Fracture surfaces

Fig. C-6 shows the fracture surfaces of UFG Fe samples with T-R orientation (a-b) and A-T orientation (c-d). All UFG Fe specimens, regardless of *R*-ratio and ΔK, exhibit almost exclusively intergranular fracture (Fig. C-6). Grains appear smaller on the fracture surface of samples with T-R orientation, because only the smaller axes of the elongated grains are visible. In A-T samples the crack can grow along the larger axis, giving a coarser-grained impression. The mean stress and the magnitude of ΔK have only a small influence on the appearance of the fracture surfaces, which indicates that the same fracture mechanisms are active independent of ΔK and *R*.

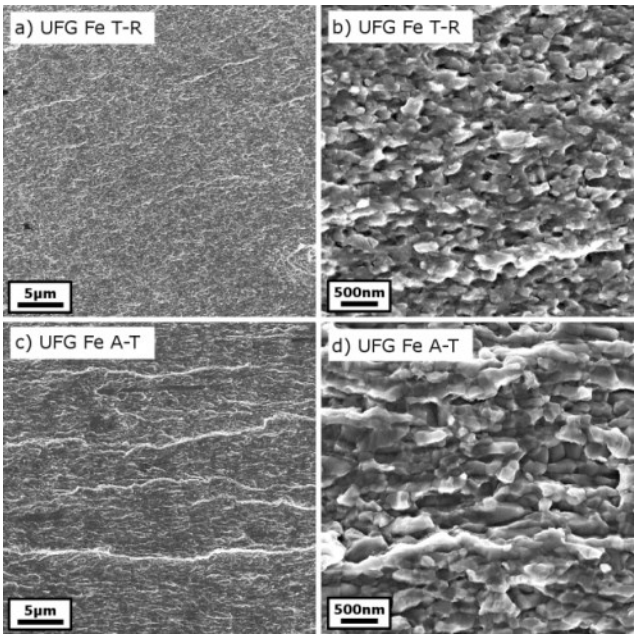

Fig. C-6: Fracture surfaces of UFG Fe samples with T-R orientation (a,b) and A-T orientation (c,d), tested at *R*=0.1. The crack propagation direction is from left to the right.

C.4 Discussion

It has been shown that there is a pronounced orientation dependence in the crack paths and the resistance against FCG in UFG Fe. In the following section the reasons for this FCG anisotropy will be discussed and compared to results for HPT deformed UFG Ni and ECAPed metals. In the discussion it will be

distinguished between intrinsic and extrinsic mechanisms affecting the FCG rate, according to [22]. Extrinsic mechanisms, like crack closure or crack deflection, reduce the local crack driving force, whereas intrinsic mechanisms are responsible for the material separation at the crack tip and, therefore, for the propagation of the crack. However, at first the effect of the macroscopic crack path has to be considered.

C.4.1 Macroscopic crack path deviations

If a crack deviates macroscopically from its straight path, the crack driving force is changed because the loading changes from Mode I to a mixed mode combination of Mode I, II and III. This means that instead of the globally applied ΔK_I a reduced local Δk is acting at the crack tip, so that the measured FCG rates correspond in reality to lower driving forces. With FE simulations the k values of different crack deflections were calculated and compared to the K_I values of a straight crack as a function of the true physical crack lengths (see section 2.1 for more details). The FE results clearly demonstrate that K_I delivers good estimations for the "true" local crack driving force k, provided the crack deflection angle and crack extension is small. For samples with a large instant crack deviation (e.g. T-A samples) k is significantly reduced even at small crack extensions, which has to be kept in mind when interpreting FCG data. However, the other crack configurations (10° and continuous change from 10° to 90°) exhibit reductions of the crack driving force of less than 5%, when data is taken only for crack extension shorter than 1.5 mm, which was the case for all data shown in this work. This confirms our assumptions for the validity of FCG data from section 2.1 for A-T, T-R and R-A samples that macroscopic geometric shielding is not an issue that needed to be considered.

C.4.2 The FCG threshold of UFG Fe and the contribution of crack closure mechanisms

Regarding the threshold of HPT deformed UFG Fe two observations can be made from Fig. C-5: Firstly, there is only a weak dependence of the threshold on the mean stress for both orientations. Secondly, hardly any orientation dependence of ΔK_{th} exists between A-T and T-R samples, although FCG rates differ markedly in the higher ΔK regime.

C.4.2.1 The dependence of ΔK_{th} on the mean stress

For both orientations the threshold decreases when the R-ratio is increased, with a 16 % lower ΔK_{th} at R=0.7 than at R=0.1 for A-T and a difference of 18 % for T-R samples (see Table C-3). A difference between 15 % and 20 % coincides with estimations for the contribution of plasticity induced crack closure (PICC) under plain strain conditions. PICC under plane strain conditions is a result of material transport to the crack tip due to the formation of a plastic wedge, which reduces the effective stress intensity range at the crack tip [23,24]. Even at higher ΔK and larger crack openings the load at the crack tip is reduced in the same relation, as the dimension of the plastic wedge scales with the rising ΔK. Therefore the presence of PICC should result in higher FCG rates for R=0.7 than for R=0.1 even at higher ΔK, which is in fact observed. Since the differences in ΔK_{th} agree with the estimations for PICC, it seems that PICC is the major contribution causing the difference between R=0.7 and 0.1 and other crack closure mechanisms play a minor role. This is not surprising for the A-T orientation, where little roughness of the crack path was observed, however, very surprising for T-R samples, which exhibits significantly larger crack path tortuosity.

Roughness induced crack closure (RICC), which is usually more pronounced in coarser grained metals, seems to be negligible in UFG Fe. Otherwise the difference in the fracture surface roughness between A-T and T-R specimens should entail a strong variation in the threshold values, which, however, was not observed. The reduced RICC seems to be a consequence of small mode II displacements Δu_2 of the crack faces of NC and UFG metals (depicted in Fig. C-7), which, besides a rough crack path, is necessary to get this crack closure contribution [25,26].

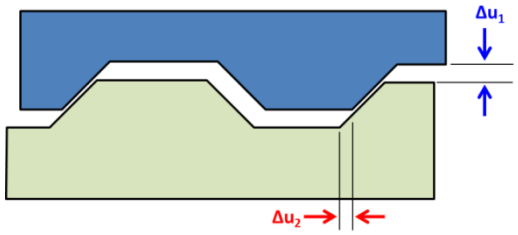

Fig. C-7: Schematic of the two sides of a crack with displacements in Mode I (Δu_1) and in Mode II (Δu_2).

The mode II displacement of the two crack flanks is a result of a local asymmetry of the plastic deformation in the plastic wake of the crack tip. Furthermore Δu_2 is proportional to the size of the cyclic plastic zone r_{CPZ} and hence dependent on the yield strength of the material σ_y [25,26]:

$$\Delta u_2 \propto r_{CPZ} \propto \frac{1}{\sigma_y} \tag{3}$$

Due to the high strength of UFG metals, the size of the plastic zone is smaller, which leads to less displacement parallel to the crack propagation direction. Additionally the small grain size might reduce the plastic asymmetry. Thus, the two sides of the crack show less mismatch of the fracture surfaces and hence less RICC. It can be concluded that the small differences between FCG data from experiments at R=0.7 and 0.1 seem to be caused by PICC.

As the FCG experiments have been started on closure free pre-cracks an R-curve behavior for the ΔK_{th} value at R=0.1 is expected. However, for all samples tested at R=0.1 no crack extension was detected until the long crack threshold was reached. The built-up of PICC requires a crack extension in the range of the plastic zone size. However, the size of the plastic zone at ΔK_{th} is only few micrometers and the detection limit of the potential drop method is about 5 µm. Therefore we assume that the very small R-curve effect of ΔK_{th} could not be detected with the used technique.

C.4.2.2 The orientation dependence of ΔK_{th}

The FCG curves in Fig. C-5 and Table C-3 show that there is hardly any orientation dependence of the threshold stress intensity factor range ΔK_{th} for UFG Fe with A-T, T-R and R-A orientation at the two tested R-ratios. However, for a T-A sample a 40 % higher ΔK_{th} is found compared to the other specimens. This higher threshold can be explained by the immediate macroscopic deviation of the crack to about 75°, which reduces the local stress intensity factor to about 60 % of the globally applied value [27] (see supplementary material more details on the simulations) The calculated local threshold value k_{th} for a T-A sample (3.4 MPa.m$^{0.5}$) correlates well with the ΔK_{th} of the other two crack orientations. This good agreement indicates that ΔK_{th} is independent of the orientation when the deviation from the straight crack path and the local stress intensity factor is taken into account.

From literature it is known, that ΔK_{th} is sensitive to the microstructure and therefore it seems surprising that no orientation dependence is found in our case. In standard literature, such as for example in [1], it is stated that the FCG in the near-threshold regime is sensitive to the microstructure, but becomes less sensitive in stage II (Paris regime). It is explained that the transition from microstructure sensitive to less sensitive occurs, when the cyclic plastic zone becomes larger than the grain size. In the case of commercially used metals, with grain sizes in the range of a few micrometers or larger, this may coincide with the transition from near-threshold to the Paris regime. In nanocrystalline (NC) and ultrafine-grained (UFG) metals, however, this does not hold true, as the grain size is so small that the cyclic plastic zone is about the same size or already larger than the mean grain size, even at the threshold. Therefore, it is reasonable that ΔK_{th} is insensitive to the orientation.

Furthermore the microstructure is the same for all orientations, however, the direction of the maximum grain elongation is different. This does not influence the ΔK_{th}, as dislocations emitted from the crack tip are supposed to experience the same forces due to the same Young's moduli and the same characteristic distances of obstacles in form of grain boundaries. However, when the crack propagates it can experience more FCG resistance for a growth direction parallel to the smaller axis of the grains, or less resistance when it propagates along the elongated grain boundaries. Therefore, in contrast to findings for microcrystalline metals, the ΔK_{th} values of NC and UFG metals with elongated grains can be orientation independent, while the FCG rates in the Paris show pronounced anisotropy.

C.4.2.3 The weak crack path in HPT deformed metals along elongated grain boundaries

In the Paris regime UFG Fe produced by HPT shows clear differences in its FCG rate depending on the orientation of the crack in respect to the alignment of the elongated grains. All samples have in common that cracks tend to change their crack path either abruptly or continuously to a crack plane almost parallel to the HPT shear plane and a crack growth in tangential direction, which is close to the situation in A-T samples (see Fig. C-2 and Fig. C-3). It can be assumed that cracks only deviate to crack paths with lower FCG resistance and so this combination of cracking plane and crack growth direction is expected to result in the fastest FCG. The FCG data shown in Fig. C-5 confirms the assumption, with an up to 10 times higher FCG rate in the Paris regime for A-T samples, compared to T-R. This is a similar trend as found for the fracture toughness [9], which also revealed a reduced resistance against crack propagation for the same orientation in quasi-static experiments. The differences between T-R and A-T samples are even larger for the FCG rate (about 10 times faster FCG in A-T) than for fracture toughness (about 5 times lower fracture toughness for A-T). Hence, macroscopic crack path analyses, as well as FCG data show that a cracking plane slightly inclined to the shear plane of the HPT process (i.e. parallel to the long axis of the elongated grains) and crack propagation in tangential direction serves as a weak path for fatigue cracks. This is also in good accordance with FCG data for HPT deformed UFG Ni of a previous work [12], where the same weak crack path was observed. Thus it seems that this feature of NC and UFG metals is independent of its crystal structure. However, it has to be noted that the differences in the FCG rates are smaller between A-T and T-R oriented samples in UFG Ni (about 4 times higher FCG rate for A-T than for T-R samples) compared to UFG Fe (about 10 times faster FCG in A-T than in T-R). The magnitude of the anisotropy seems to be influenced by material properties, as for example by the grain geometry, the grain boundary strength and maybe the impurity content.

C.4.3 FCG growth mechanisms in UFG Fe

The pronounced orientation dependence of the FCG rates might be an effect of a change in the intrinsic crack propagation mechanism, an extrinsic effect or a change of both. As already discussed only PICC delivers a small contribution at low *R*-ratios, which, however is independent of the propagation direction. Hence, only geometric shielding mechanisms (crack deflection and crack branching) and a change of the intrinsic mechanism should explain the observed FCG anisotropy. The slope of the FCG curve in the Paris regime and the effect of the mean stress are indicators of the prevalent FCG mechanisms. The total crack advance per cycle is a result of the crack advance due to plastic deformation and the contribution from damage accumulation and static fracture, which can be expressed by:

$$\left(\frac{da}{dN}\right)_{total} = \left(\frac{da}{dN}\right)_{pl.\ deformation} + \left(\frac{da}{dN}\right)_{damage+static\ fract.} \tag{4}$$

Ductile metals in general exhibit a cycle by cycle fatigue crack growth, which means that after each loading cycle the crack propagated for a characteristic distance. The crack advance per cycle caused by the ductile blunting and re-sharpening process depends on the cyclic crack tip opening displacement ⊿*CTOD*, as well as on the morphology of the crack tip and can be estimated by:

$$\left(\frac{da}{dN}\right)_{pl.\ deformation} = c * \Delta CTOD \tag{5}$$

The factor *c* is dimensionless and depends on the geometry and the reversibility of the deformation of the crack tip, which, in other words, is the reversibility of the formation of new fracture surface. This *c* value should also depend strongly on the crack morphology, i.e. if the crack grows predominantly under ideal mode I condition or under heavy local mixed mode loading. The coefficient *c* should not be confused with *C* of the Paris equation. ⊿*CTOD* can be estimated by the following equation:

$$\Delta CTOD = d_n \cdot \frac{\Delta k^2}{2\sigma_y E} \tag{6}$$

where σ_y is the yield strength, *E* the Young's modulus, ⊿*k* the local effective stress intensity factor range and d_n a factor dependent on the cyclic hardening behavior of the material. d_n was taken to be 0.78, representing a non-hardening behavior [33], which is a good approximation for the present SPD material. From Equ. 5 and 6 several relations for the blunting and re-sharpening process can be derived, which are depicted schematically in Fig. C-8. In this figure the crack tip of a ductile material is shown during two load cycles (1-5) for five different situations (a-e) of FCG. All situations have in common that at first the crack is closed (1) and opens by blunting due to plastic deformation upon loading (2). After unloading (3) the crack is closed again, however the crack advanced for the distance ⊿*a*. The loading and unloading steps are repeated in (4) and (5). Fig. C-8(b) shows the situation for a higher load amplitude than in (a). This leads to a larger ⊿*CTOD* and hence to a larger crack advance, provided that the crack tip geometry is the same and crack tip opening angle stays constant. The load amplitude and hence the ⊿*CTOD* in Fig. C-8 (c-e) are the same as in the first case, however, the crack tip geometry and the crack propagation mode are different and so are the lengths of the crack advances. The contribution of static fracture and further damage, described by the second term in Equ. 4, can change the crack tip opening angle and can lead to larger crack advance per cycle (Fig. C-8(c)). However, the contribution from damage accumulation is not necessarily a cycle by cycle contribution, as it can cause a significant additional crack extension after a certain number of cycles, as shown in Fig. C-8(d)

and (e). In Fig. C-8(d) damage accumulation in the vicinity of the crack tip is marked by a shaded area. The crack advance during the first cycle is purely a result of plastic deformation, in the second cycle, however, additional crack extension from local fracture occurs. In Fig. C-8(e) a microcrack is depicted ahead of the main crack, which coalesces with the main crack upon loading.

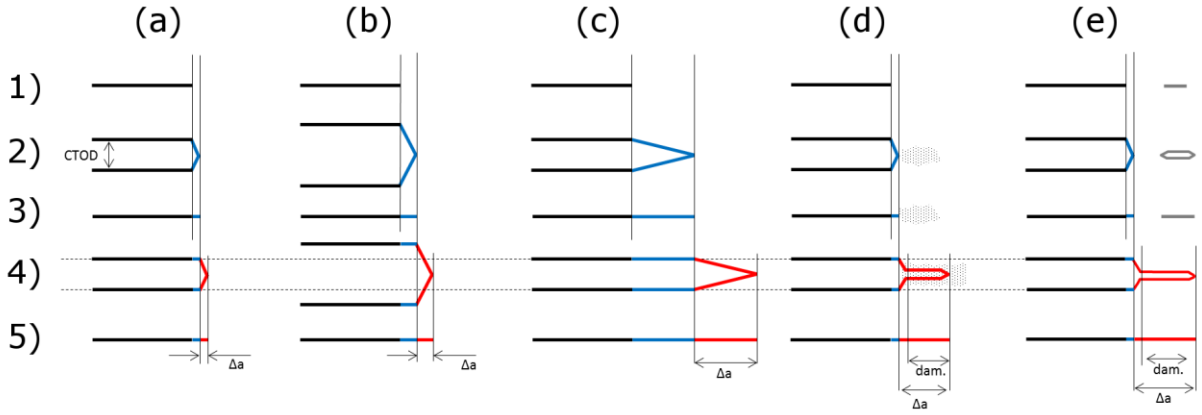

Fig. C-8: Illustration of a crack tip in a ductile material during cyclic loading for 5 different situations (a-e). In step (1) the crack is unloaded and closed. The crack opens upon loading (2), which results in the blunting of the crack tip. In step (3) the crack is unloaded, however, the crack propagated, which is marked by a blue segment. In (4) and (5) the loading and unloading is repeated and the crack advance marked by Δa and a red segment. In loading case (a) and (c-e) the crack is loaded by the same ΔK_{eff} which results in the same *CTOD*, marked by dotted lines in step (4). In (b) ΔK_{eff} is higher and thus a larger *CTOD* is visible. Situations (a) and (b) show FCG as a result of blunting and re-sharpening only. In (c-e) FCG is a result of plastic deformation and local fracture, as well as damage accumulation. The shaded areas in (d) mark damaged material ahead of the crack tip, which upon loading in a certain cycle fracture and deliver additional crack advance (marked by "dam." in step 5). In (e) additional crack extension occurs due the coalescence of a microcrack with the main crack (marked by "dam."), which is similarly to d) not a cycle by cycle process.

The most prominent model for FCG as a result of pure crack tip deformation predicts an exponent m of 2 in the Paris regime (see Equ. 2). This is a result of the proportionality of the FCG rate (da/dN) to the cyclic crack tip opening displacement ($\Delta CTOD$) and hence a proportionality of (da/dN) to ΔK^2 [28–31], as given by Equ. 5 and 6. Damage accumulation based models of FCG, in contrast, would yield an exponent of 4, according to [32].For all samples of the present study a slope close to 3 was determined, as can be seen in Fig. C-5 and Table C-4. The exponent of 3 of the FCG data of UFG Fe is the main difference compared to UFG Ni, where an m value of 2 was observed [12]. Despite this difference in the exponent m we believe that for both materials the FCG mechanisms are similar and mainly governed by blunting and re-sharpening. If FCG by damage accumulation or static fracture was important, the crack growth rate should be larger than expected from the $\Delta CTOD$ values, and this is not the case. Furthermore, the K_{max} values of the applied cyclic loads are smaller than the determined fracture toughness values of A-T and T-R specimens (see [9]). Therefore, the FCG process should not be significantly influenced by fracture toughness of the material.

If contributions of damage accumulation are excluded, an exponent larger than 2 could mean, that the factor c is not constant but increasing with increasing $\Delta CTOD$. In the present experiments the estimated FCG rate with a factor c of 0.3 is too high to match the measured data at small ΔK and small $\Delta CTOD$ and hence a larger crack opening angle (lower factor c) seems to be more appropriate (see dash-dotted line Fig. C-5). At higher ΔK and larger $\Delta CTOD$ the estimation of c with 0.3 seems to be correct, as the calculated and measured data coincide. It has to be noted, that the estimation of the FCG rate from plastic deformation gives larger values in the near-threshold regime and seems to be an upper limit in the Paris regime. Thus, it is unlikely that

damage accumulation, like microcracks, and static fracture events strongly contribute to the FCG process, as this would increase the FCG rate, although the measured FCG rates are smaller than expected.

Furthermore it has to be noted that also in very ductile coarse-grained materials, especially in ferritic steels sometimes a ΔK^3 relation is observed [35]. This is especially the case in the crack growth regime between FCG rates of 1 and 100 nm/cycle, while for larger growth rates a transition to a ΔK^2 relation occurs. However, due to the limitations in the sample geometry and the limited fracture toughness of HPT deformed materials no valid FCG data for T-R specimens could be obtained for higher ΔK. For A-T specimens the low fracture toughness of this orientation (about 14 MPa.m$^{0.5}$ [9], indicated in Fig. C-5 by arrows) could additionally promote higher slopes. For cyclic loading with a maximum stress intensity factor K_{max} close to the fracture toughness unstable crack growth and an acceleration of the FCG occurs, leading to a higher slope in the FCG curve. For a material with low fracture toughness, such as UFG Fe with A-T orientation, it means that the Paris region can be less developed, as K_{max} is already approaching the fracture toughness when the near-threshold behavior would end and stable crack growth would set in. Another observation in favor of a FCG by blunting is the occurrence of deformation patterns which can be seen on the fracture surfaces. An example of an A-T sample is given in Fig. C-9. The regular lines correlate well with slip steps from dislocations, which were calculated in simulations to form regular patterns during the propagation of a fatigue crack by a blunting and re-sharpening process [36].

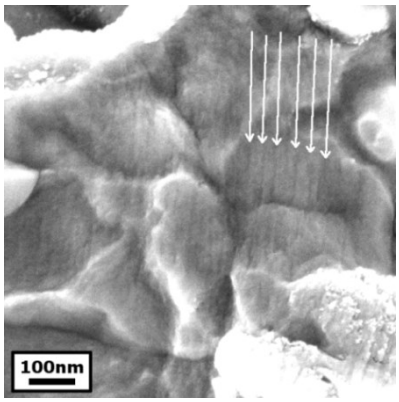

Fig. C-9: SEM image of the fracture surface of a Fe UFG A-T sample, with the crack propagation direction from left to right. Regular lines can be observed under high magnifications, examples are marked by white arrows.

C.4.4 The effect of crack deflection

In the previous sections it was shown that fatigue crack growth occurs along the grain boundaries in all tested samples. In A-T oriented samples the designated crack growth direction is almost parallel to the long axis of the elongated grains, which means that cracks can easily follow long grain boundaries (see schematic in Fig. C-10(a)). On triple points of the grain boundaries the crack has to deviate only slightly from its path to follow the next grain boundary and hence crack segments in A-T specimens show low deflection angles, as shown in the diagram in Fig. C-4(c). In T-R specimens the fatigue crack has in general to deviate to larger angles at grain boundary triple points to follow the next grain boundary, which also results in a rougher fracture surface, a frequent branching of the crack and a longer true crack path (Fig. C-10(b)). With such variations in the crack paths, also differences in the FCG growth rate can be expected. The repeated microscopic crack deflections reduce the local crack driving force at the crack. Furthermore, with the potential drop technique projected mean crack lengths are determined during the FCG tests and not the true crack

length, which can be substantially longer. Therefore the projected crack advance per cycle is determined and not the true FCG rate. In the following possibilities will be presented, how the stress intensity range at the crack tip (Δk) and the true FCG rate $(da/dN)_{true}$ can be calculated from the measured data. If these recalculated FCG curves of the differently oriented samples coincide, geometric shielding could be identified as the main reason for the varying FCG rates.

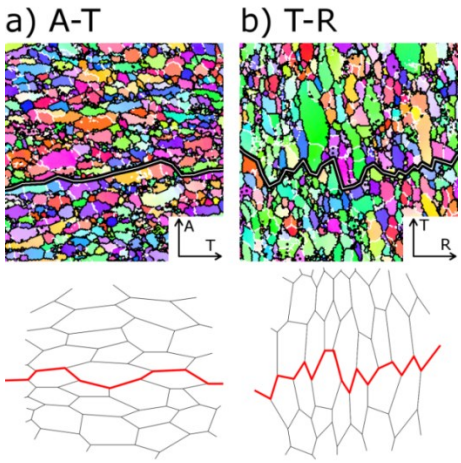

Fig. C-10: Crack path of (a) A-T and (b) T-R oriented samples, marked on EBSD images. Additionally schematic illustrations of the microstructure and the crack path are shown.

Repeated changes in the crack growth direction, e.g. due to deflections along grain boundaries, can reduce the crack driving force locally and lead to FCG curves shifted to lower ΔK values, if the effective driving force at the crack tip would be considered. This can be modelled by a crack with straight segments of the length S and regular deviations of the length D with an inclination of the angle θ to the straight crack path [37] and from that an effective stress intensity range (Δk) can be derived. Δk can be calculated from the globally applied ΔK_I when the ratio of the true to the projected crack length, which is equal to the linear roughness parameter R_L, is known [12]:

$$R_L = \frac{true\ length}{projected\ length} = \frac{S+D}{S+D*\cos(\theta)} \tag{7}$$

$$\Delta \mathrm{k} = \frac{D\ cos^2\left(\frac{\theta}{2}\right)+S}{D+S}\Delta K_I = \frac{1+R_L}{2*R_L}\Delta K_I \tag{8}$$

With the linear roughness parameters from Table C-2 the Δk values were calculated for the FCG data of A-T and T-R specimens measured at R=0.1 and R=0.7. In Fig. C-11(a) and (d) the original data (slightly transparent symbols) is shown together with the recalculated data for R=0.1 and R=0.7 experiments. The FCG curves are shifted to lower ΔK values when Δk is used instead of the globally applied ΔK. This is especially the case for the T-R orientation, which exhibits larger crack deviations and hence a larger R_L value. By this recalculation the differences in the FCG rates between the two orientations become smaller at ΔK larger than 3 MPa.m$^{0.5}$, however, there is still a remarkable difference.

Due to the nature of the potential drop technique, only projected mean crack lengths are determined during the FCG tests. However, as shown in Fig. C-4 the true crack length and the new surface created by crack advance can be substantially larger when there are crack deflections like in the case of T-R orientations.

For a known R_L a true FCG rate $(da/dN)_{true}$ can be calculated from the measured FCG rate (da/dN) by the following expression [12,37]:

$$\left(\frac{da}{dN}\right)_{true} = \left[\frac{D+S}{D\cos(\theta)+S}\right]\left(\frac{da}{dN}\right) = R_L\left(\frac{da}{dN}\right) \tag{9}$$

The true FCG rates were calculated for R=0.7 data of A-T and T-R specimens and are shown in Fig. C-11(b) and (e). The recalculated curves are shifted to higher FCG rates and as before the modification has larger effects on T-R data, due to the larger roughness parameter. The variation between the A-T and T-R orientation decreases, but the FCG rates are still considerably higher for A-T samples. A difference in the roughness value R_L by a factor of 10 between A-T and T-R samples would be needed in order to fully explain the differences in the FCG rates by this simplified assumption. However, this extreme difference in the roughness of the fracture paths was clearly not observed. Thus, the difference in the newly created surface can contribute to the orientation dependent FCG rates but is not the sole reason for it.

In Fig. C-11(c) and (f) both previously described corrections are applied to the FCG data at the same time. Thereby the differences in the FCG rates between A-T and T-R specimens are reduced in the Paris regime, however, the FCG is still about two times faster in A-T samples. Thus, even by taking geometric shielding into account the anisotropic FCG behavior cannot be fully explained.

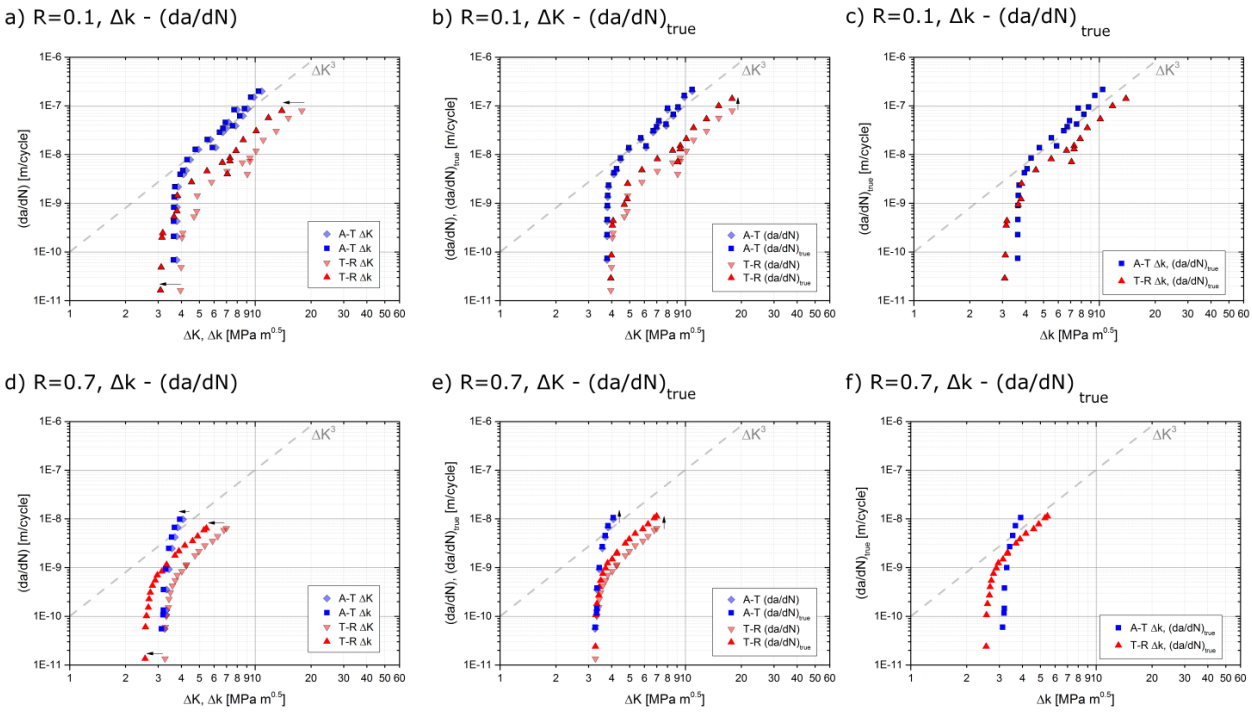

Fig. C-11: FCG diagrams for UFG Fe samples with A-T and T-R orientation, tested at R=0.1 (a-c) and R=0.7 (d-f). The originally measured data is shown by slightly transparent symbols for comparison. For (a) and (d) the regular microscopic crack deviations were taken into account and the effective stress intensity range at the crack tip was calculated. The FCG curves are shifted to lower ΔK values. In (b) and (e) the FCG rate is recalculated for the true crack length. The FCG curves are shifted to higher FCG rates. In (c) and (f) both recalculations are applied.

There are few phenomena which have not been taken into account so far:

- Local crack branching (see also Fig. C-4) may further reduce the locale Δk. This is more frequently observed in the T-R orientation of UFG Fe than in the same orientation of UFG Ni, which could explain the larger anisotropy in UFG Fe.
- The 3D nature of the crack shape, which may induce an additional Mode III component of the stress intensity factor range. Thereby the local Δk is further reduced, which would explain why the ΔK_{th} is not orientation dependent. In the straight regions of the crack front the crack starts to propagate at ΔK_{th}. In deflected segments, however, the locale crack driving force is reduced and thus the crack front does not advance. After a certain crack extension in the straight segments the crack driving force in the deflected parts is increased enough to overcome the threshold and to also cause crack advance in this regions of the crack front. This process seems to significantly reduce the global crack growth rate compared to samples where less crack deflection occurs along the crack front.
- Finally one should note that also the intrinsic mechanisms may contribute to the orientation dependence, because the prefactor c in Equ. 5 may depend on the load mixity, which may introduce an additional effect to the orientation dependence of the FCG rate.

C.4.5 Comparison of HPT to ECAP results

The few FCG experiments on UFG metals were performed predominately on ECAPed materials. Also the orientation dependence of some ECAPed metals has already been in focus, as can be seen for example in the works of Vinogradov et al. [38] for a CuCrZr alloy and Niendorf et al. [39] for IF steel. In contrast to the findings on HPT deformed Ni and Fe, the ECAPed materials in these studies show hardly any FCG anisotropy. One explanation for this difference could be the orientation of the samples in respect to the shear plane of the deformation process. The orientations of the HPT samples were chosen to represent extreme conditions: either crack growth parallel to the shear plane or perpendicular to it. This, however, is not the case for the ECAP specimens of the two works mentioned above, where cracks are introduced in an angle of about 45° to the shear plane, due to the inclination of the shear plane to the extrusion direction. Therefore, differences in the FCG behavior can be expected to be less pronounced than in HPT samples. Furthermore, during the deformation of the usually investigated ECAP material the shear plane changes for each pressing due to the rotation of the billet for 90° (ECAP route B_C). Thus the grains are less elongated than in HPT deformed material, where the shear plane is the same during the whole process. This more equiaxed grain geometry can also reduce the FCG anisotropy and may be more important than the mean grain size. Additionally, due to the limited number of passes ECAPed material shows a lower fraction of high angle grain boundaries (HAGB) compared to HPT deformed metals [40,41]. As FCG is preferentially found on HAGB, reduced orientation dependence can be expected for materials processed by ECAP.

C.5 Conclusion

For this study severely plastically deformed UFG ARMCO Fe was chosen as a model material to investigate the fatigue crack growth behavior of a body-centered cubic UFG metal. The FCG characteristics of UFG Fe can be summarized as follows:

(1) Intergranular fatigue crack growth in UFG Fe is the result of a blunting and re-sharpening process along the grain boundaries and not due to grain boundary embrittlement.

(2) Fatigue cracks change their paths either abruptly or continuously in order to propagate in a plane parallel to the shear plane, which is parallel to the long axis of the elongated grains.
(3) The contribution of crack closure to the FCG resistance is small and mainly plasticity-induced. Thus, only a weak influence of the mean stress on ΔK_{th} and the FCG rates was found.
(4) No orientation dependency is observed for the threshold stress intensity factor range ΔK_{th} when the macroscopic deviation of the fatigue crack is taken into account.
(5) Cracks introduced in shear direction of the HPT process exhibit a 10 times faster FCG than cracks perpendicular to it. The differences can neither be fully explained by extrinsic shielding mechanisms, nor by the crystallographic texture. It seems that regular crack branching reduces the local load at the crack tip and hence the $\Delta CTOD$ even more than estimated by common models.
(6) The FCG of UFG ARMCO Fe shows basically the same characteristics as for UFG Ni, except the somewhat larger exponent m in the Paris regime. Hence, it can be assumed that FCG is governed by the same mechanisms irrespective of the crystal lattice.

C.6 Acknowledgment

Funding of this work has been provided by the European Research Council under ERC Grant Agreement No. 340185 USMS and by the Austrian Science Fund in the framework of research project P26729-N19.

C.7 References

[1] R.. Valiev, R.. Islamgaliev, I.. Alexandrov, Bulk nanostructured materials from severe plastic deformation, Prog. Mater. Sci. 45 (2000) 103–189.
[2] K.. Kumar, H. Van Swygenhoven, S. Suresh, Mechanical behavior of nanocrystalline metals and alloys, Acta Mater. 51 (2003) 5743–5774.
[3] Y.T. Zhu, T.G. Langdon, The fundamentals of nanostructured materials processed by severe plastic deformation, JOM. 56 (2004) 58–63.
[4] A. Zhilyaev, T. Langdon, Using high-pressure torsion for metal processing: Fundamentals and applications, Prog. Mater. Sci. 53 (2008) 893–979.
[5] R.Z. Valiev, Y.V. Ivanisenko, E.F. Rauch, B. Baudelet, Structure and deformaton behaviour of Armco iron subjected to severe plastic deformation, Acta Mater. 44 (1996) 4705–4712.
[6] F. Wetscher, A. Vorhauer, R. Stock, R. Pippan, Structural refinement of low alloyed steels during severe plastic deformation, Mater. Sci. Eng. A. 387-389 (2004) 809–816.
[7] A. Vorhauer, R. Pippan, On the Onset of a Steady State in Body-Centered Cubic Iron during Severe Plastic Deformation at Low Homologous Temperatures, Metall. Mater. Trans. A. 39 (2007) 417–429.
[8] A. Hohenwarter, R. Pippan, Fracture toughness evaluation of ultrafine-grained nickel, Scr. Mater. 64 (2011) 982–985.
[9] A. Hohenwarter, R. Pippan, Anisotropic fracture behavior of ultrafine-grained iron, Mater. Sci. Eng. A. 527 (2010) 2649–2656.
[10] A. Hohenwarter, R. Pippan, Fracture and fracture toughness of nanopolycrystalline metals produced by severe plastic deformation., Philos. Trans. A. Math. Phys. Eng. Sci. 373 (2015) 20140366–.
[11] G.B. Rathmayr, A. Hohenwarter, R. Pippan, Influence of grain shape and orientation on the mechanical properties of high pressure torsion deformed nickel, Mater. Sci. Eng. A. 560 (2013) 224–231.
[12] T. Leitner, A. Hohenwarter, R. Pippan, Revisiting fatigue crack growth in various grain size regimes of Ni, Mater. Sci. Eng. A. 646 (2015) 294–305.

[13] J.-C. Lee, H.-K. Seok, J.-Y. Suh, Microstructural evolutions of the Al strip prepared by cold rolling and continuous equal channel angular pressing, Acta Mater. 50 (2002) 4005–4019.
[14] D.V. Gunderov, A.V. Polyakov, I.P. Semenova, G.I. Raab, A.A. Churakova, E.I. Gimaltdinova, I. Sabirov, J. Segurado, V.D. Sitdikov, I.V. Alexandrov, N.A. Enikeev, R.Z. Valiev, Evolution of microstructure, macrotexture and mechanical properties of commercially pure Ti during ECAP-conform processing and drawing, Mater. Sci. Eng. A. 562 (2013) 128–136.
[15] N. Kamikawa, T. Sakai, N. Tsuji, Effect of redundant shear strain on microstructure and texture evolution during accumulative roll-bonding in ultralow carbon IF steel, Acta Mater. 55 (2007) 5873–5888.
[16] R.O. Ritchie, The conflicts between strength and toughness, Nat. Mater. 10 (2011) 817–822.
[17] D. Tabor, A Simple Theory of Static and Dynamic Hardness, Proc. R. Soc. A Math. Phys. Eng. Sci. 192 (1948) 247–274.
[18] R. Pippan, L. Plochl, F. Klanner, H.P. Stuwe, Use of fatigue specimens precracked in compression for measuring threshold values and crack growth, J. Test. Eval. 22 (1994) 98–103.
[19] ASTM E399-12e3, Standard Test Method for Linear-Elastic Plane-Strain Fracture Toughness KIc of Metallic Materials, ASTM Int. (2012).
[20] ASTM E647-15, Standard Test Method for Measurement of Fatigue Crack Growth Rates, ASTM Int. (2015).
[21] G.R. Irwin, Plastic zone near a crack and fracture toughness, Proc. Seventh Sagamore Ordnance Mater. Res. Conf. (1960) IV–63.
[22] R.O. Ritchie, Mechanisms of fatigue crack propagation in metals, ceramics and composites: Role of crack tip shielding, Mater. Sci. Eng. A. 103 (1988) 15–28.
[23] S. Suresh, Fatigue of Materials, Cambridge University Press, 1991.
[24] F.O. Riemelmoser, R. Pippan, Mechanical reasons for plasticity-induced crack closure under plane strain conditions, Fatigue Fract. Eng. Mater. Struct. 21 (1998) 1425–1433.
[25] R. Pippan, G. Strobl, H. Kreuzer, C. Motz, Asymmetric crack wake plasticity – a reason for roughness induced crack closure, Acta Mater. 52 (2004) 4493–4502.
[26] J. Pokluda, R. Pippan, Analysis of roughness-induced crack closure based on asymmetric crack-wake plasticity and size ratio effect, Mater. Sci. Eng. A. 462 (2007) 355–358.
[27] H. Kitagawa, R. Yuuki, T. Ohira, Crack-morphological aspects in fracture mechanics, Eng. Fract. Mech. 7 (1975) 515–529.
[28] C. Laird, The Influence of Metallurgical Structure on the Mechanisms of Fatigue Crack Propagation, Fatigue Crack Propagation, ASTM STP 415. (1967) 131.
[29] C. Laird, G.C. Smith, Crack propagation in high stress fatigue, Philos. Mag. 7 (1962) 847–857.
[30] P. Neumann, Coarse slip model of fatigue, Acta Metall. 17 (1969) 1219–1225.
[31] R.M.N. Pelloux, Crack extension by alternating shear, Eng. Fract. Mech. 1 (1970) 697–704.
[32] J. Ricel, The mechanics of crack tip deformation and extension by fatigue, Fatigue Crack Propagation, ASTM, ASTM STP. (1967) 415.
[33] C.F. Shih, Relationships between the J-integral and the crack opening displacement for stationary and extending cracks, J. Mech. Phys. Solids. 29 (1981) 305–326.
[34] R.O. Ritchie, Mechanisms of fatigue-crack propagation in ductile and brittle solids, Int. J. Fract. 100 (1999) 55–83.
[35] R. Pippan, C. Zelger, E. Gach, C. Bichler, H. Weinhandl, On the mechanism of fatigue crack propagation in ductile metallic materials, Fatigue Fract. Eng. Mater. Struct. 34 (2011) 1–16.

[36] R. Pippan, H. Weinhandl, Discrete dislocation modelling of near threshold fatigue crack propagation, Int. J. Fatigue. 32 (2010) 1503–1510.
[37] S. Suresh, Fatigue crack deflection and fracture surface contact: Micromechanical models, Metall. Trans. A. 16 (1985) 249–260.
[38] A. Vinogradov, K. Kitagawa, V.I. Kopylov, Fracture and Fatigue Resistance of Ultrafine Grain CuCrZr Alloy Produced ECAP, Mater. Sci. Forum. 503-504 (2006) 811–816.
[39] T. Niendorf, F. Rubitschek, H.J. Maier, D. Canadinc, I. Karaman, On the fatigue crack growth–microstructure relationship in ultrafine-grained interstitial-free steel, J. Mater. Sci. 45 (2010) 4813–4821.
[40] R. Pippan, S. Scheriau, A. Taylor, M. Hafok, A. Hohenwarter, A. Bachmaier, Saturation of Fragmentation During Severe Plastic Deformation, Annu. Rev. Mater. Res. 40 (2010) 319–343.
[41] A.P. Zhilyaev, B.-K. Kim, J.A. Szpunar, M.D. Baró, T.G. Langdon, The microstructural characteristics of ultrafine-grained nickel, Mater. Sci. Eng. A. 391 (2005) 377–389.
[42] B. Cotterell, J.R. Rice, Slightly curved or kinked cracks, Int. J. Fract. 16 (1980) 155–169.

C.8 Supplementary Material

C.8.1 Effect of macroscopic crack deflections

In order to study the effect of crack deflections on the effective crack driving force, and hence the FCG curves, finite element (FE) simulations were performed for two-dimensional CT specimens with the same dimensions as the samples used in the experiments (W = 5.4 mm, B = 1.3 mm and initial crack length a_0 = 1.08 mm; see also section 2). Straight crack growth with 5 different deflection angles ranging from 0° to 80°, as well as a continuous change in the crack growth direction were considered. A crack deflection by 10° represents sample orientation A-T, 80° crack deflection represents orientation T-A and a continuous change in the crack growth direction represents the T-R orientation. For each configuration various "true" crack extensions, i.e. the length of the deflected part of the crack, between Δa_{true} = 0.2 mm – 2.9 mm were modelled. The specimens were subjected to monotonic loading in Mode I by prescribing a (constant) load F = 100 N. It should be mentioned that the relations between the effective K values, basically, do not change if cyclic loading is modelled, hence, it is possible to draw the same conclusions for cyclic loading as for monotonic loading. The commercially available FE program ABAQUS (see http://simulia.com/products/abaqus_fea.html) was used to create the model and to perform the stress and strain analysis. Bilinear 4-node elements were used for the FE-mesh. Small strain setting was assumed. The material was selected to be homogeneous, isotropic elastic–ideally plastic (following incremental theory of plasticity), with Young's modulus E = 210 GPa, Poisson's ratio ν = 0.3 and yield strength σ_y = 1230 (estimated via indentation tests). The magnitudes of the crack driving force were evaluated in terms of local stress intensity factor values, k. For the straight crack $k = K_I$ applies. For deflected cracks k was calculated from the local Mode I and II stress intensity factors following [1],

$$k = \sqrt{{k_I}^2 + {k_{II}}^2} \quad . \tag{1}$$

At this point, it should be emphasized that the requirements for the applicability of the stress intensity factor was met for all modelled scenarios. The k values of the deflected cracks were related to the K values of an undeflected crack (i) with equal projected crack extension $\Delta a_{proj.}$ and (ii) with equal true physical crack lengths Δa_{true}, i.e. the extension of the undeflected crack is equal to the length of the deflected part of the crack. Additionally, the relations k/K_I were calculated from the analytical model for cracks with infinitesimally short deflections for deflection angles of 30°, 45° and 80° [2] and compared with the simulated results.

Fig. 1 presents the variations of the stress intensity ratios k/K_I of straight cracks with different deflection angles, plotted against crack extension Δa. In Fig. 2 the results of three different configurations are depicted, which represent the three sample orientations used in this study. Fig. 1(a) and Fig. 2(a) show k/K_I values as a function of the true crack extension Δa_{true}; here, the total crack length of the straight and kinked crack are the same. Fig. 1(b) and Fig. 2(b) show the k/K_I values versus the projected crack extension $\Delta a_{proj.}$; here, the K_I value corresponds to a crack length obtained after projection of the kinked crack onto the symmetry plane. From the results in Fig. 1(a) it can be seen that even for a crack with a deflection angle of 30° the reduction of the k compared to a straight crack is only about 10%. The same is true for the crack with a continuous change of the crack growth direction (T-R) in Fig. 2(a) up to a crack extension of 1.25 mm, at which the crack deflection angle is 30°. Cracks with an instant deflection to 80° (T-A) experience a 40% reduced driving force at the crack tip, even at small crack deflections, which is in good agreement with the analytical solution of [2].

For small crack extensions and a current introduction from the side faces, the potential drop method yields a crack length close to the projected length of the crack and thus the comparisons in Fig. 1(b) and Fig. 2(b) have to be considered. Basically, the same conclusions can be drawn as for the previous comparison: The 80° crack configuration shows larger differences even for small crack extension, for the other configurations with deflections angles from 0° to 30° differences are less than 5% up to a crack extension of 1.25 mm. Hence, only for the immediate 80° deflection of the crack the macroscopic deflection of the crack has been taken into account.

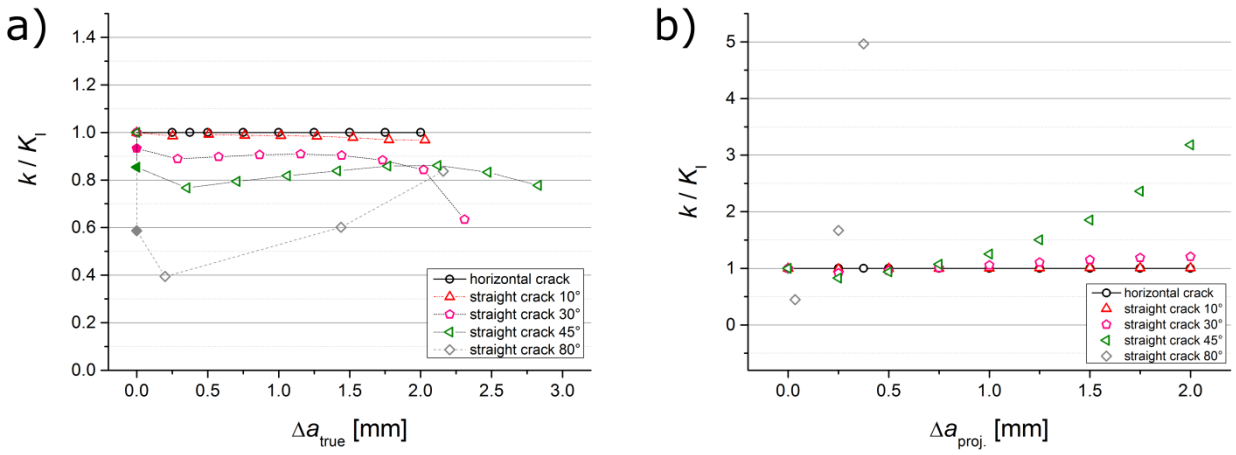

Supplementary Fig. 1: The effective local stress intensity factor k_f for cracks with different deflection angles (10°, 30°, 45° and 80°) is compared to the mode I stress intensity factor of a undeflected crack. a) shows the relations for chosen true crack extensions (Δa_{true}) and b) for chosen projected crack extensions ($\Delta a_{proj.}$). The first data points (filled symbols) are calculated from the analytical model for cracks with infinitesimally short deflections [2].

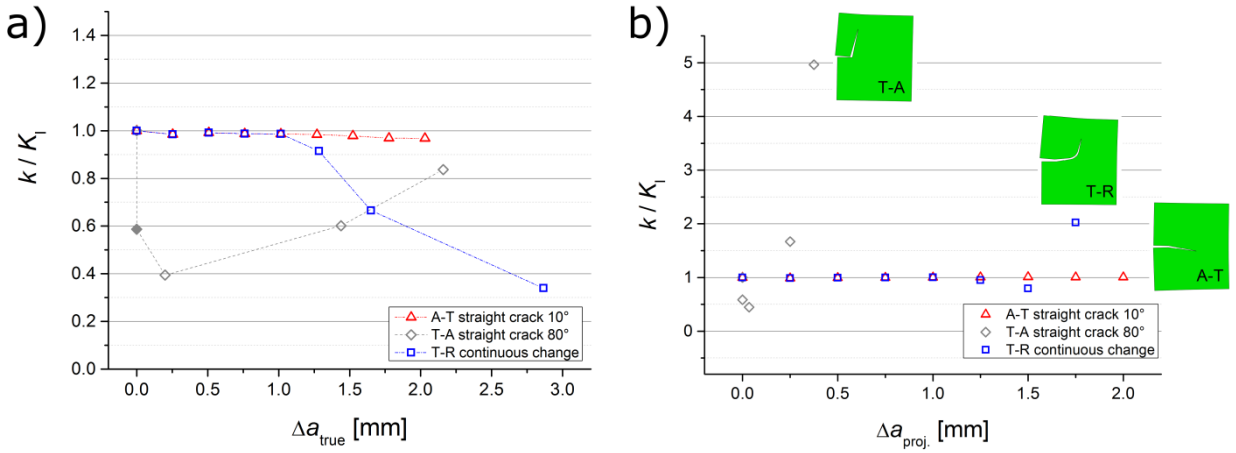

Supplementary Fig. 2: Comparison of the k_f for deflected cracks, which represent three different sample orientations used in this study, to the mode I stress intensity factor of an undeflected crack. a) shows the relations for chosen true crack extensions (Δa_{true}) and b) for chosen projected crack extensions ($\Delta a_{proj.}$). The first data point of the T-A crack (filled symbol) is calculated from the analytical model for cracks with infinitesimally short deflections [2].

C.8.2 Error estimation

Errors in the FCG curves can arise from the measurement of the crack length and the measurement of the force. The crack length determined by PDT was controlled with optical measurements and a good accordance was found. An exception was a sample for which the optical measurement yielded an about 20% longer crack length. In order to see the effect of this largest found error of the crack length measurement on the FCG curve, the crack length data of this T-R sample tested at R=0.1 was scaled to get a 20% larger crack length value at the end of the FCG test (depicted in Fig. 3). From the scaled data da/dN and ΔK were re-calculated and plotted together with the original data in Fig. 3. It can be seen that the error in the double logarithmic plot is small, even at high ΔK values around 20 MPa.m$^{0.5}$ and does not change the slope of the curve in the Paris regime. The error of the FCG curve is even smaller in the near threshold regime, as the error of the crack length measurement will be smaller for short crack extensions. Additionally, the error resulting from the force measurement was assessed, which originates from the error of the load cell (which is less than 1%) and the transformation to an analog signal for the input to the data acquisition system. By comparing the force values from the measurement system to the values of the controller of the testing system only small errors less than then 5% were found. To account for the maximum error, ΔK was re-calculated for 5% higher forces and the resulting FCG curve added to Fig. 3. Even with the error from the force measurement included the FCG curve does not substantially change its shape. Thus, it can be concluded that the errors of the crack length and force measurement do not change the FCG curves significantly and hence the relations discussed in the paper and the conclusions are not affected by the measurement error.

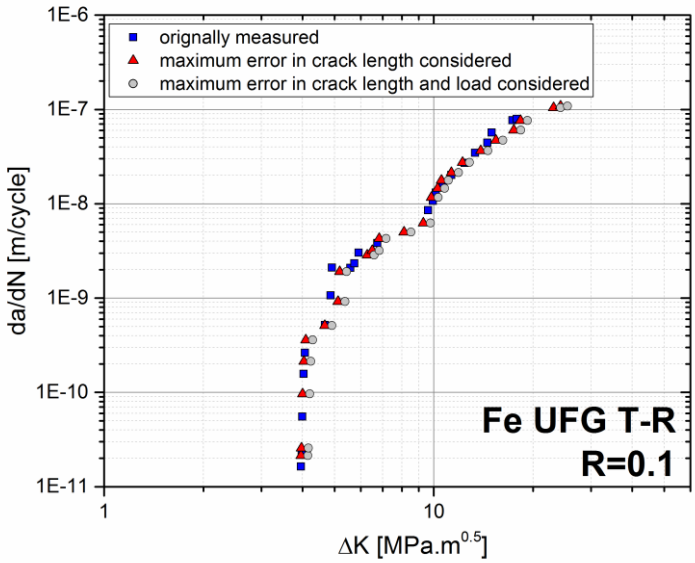

Supplementary Fig. 3: Estimated errors resulting from crack length and force measurement are taken into account by re-calculating the FCG curves for data with the maximum error found during the FCG tests. Exemplarily the re-calculated FCG curves for a T-R specimen tested at R=0.1 are shown together with the originally determined FCG curve.

C.8.3 References

[1] S. Suresh, Fatigue crack deflection and fracture surface contact: Micromechanical models, Metall. Trans. A. 16 (1985) 249–260.

[2] B. Cotterell, J.R. Rice, Slightly curved or kinked cracks, Int. J. Fract. 16 (1980) 155–169.

D The effect of severe grain refinement on the damage tolerance of a superelastic NiTi shape memory alloy

Thomas Leitner [1], Ilchat Sabirov [2], Reinhard Pippan [3], Anton Hohenwarter [1]

[1] Department of Materials Physics, Montanuniversität Leoben, Leoben, Austria

[2] Madrid Institute for Advanced Studies of Materials, Madrid, Spain

[3] Erich Schmid Institute of Materials Science, Austrian Academy of Sciences, Leoben, Austria

Abstract

Nickel-titanium (NiTi) shape memory alloys are widely used for medical components, as they can accommodate large strains in their superelastic state. In order to further improve the mechanical properties of NiTi, grain refinement by severe plastic deformation is applied to generate an ultrafine-grained microstructure with increased strength. In this work comprehensive fracture and fatigue crack growth experiments were performed on ultrafine-grained NiTi to assess its damage tolerance, which is essential for the safe use of this material in medical applications. It was found, that equal channel angular pressing of NiTi for 8 passes route B_C increases the transformation stress by a factor of 1.5 and the yield stress of the martensite by a factor of 2.6, without significantly deteriorating its fracture and fatigue crack growth behavior. The fatigue crack growth behavior at high mean stresses is even improved, with lower fatigue crack growth rates and higher threshold stress intensity factor ranges, however, beneficial contributions from crack closure are slightly reduced.

D.1 Introduction

Since the discovery of the superelastic and shape memory properties of nickel-titanium alloys in the 1960s, the material has been implemented in many applications. Responsible for both effects is the phase transformation of the intermetallic alloys between an austenitic (simple cubic B2 structure) and a martensitic phase (monoclinic B19' structure) as described in early studies [1,2]. In their superelastic state NiTi alloys can accommodate strains up to 10% by a stress induced transformation of austenite to martensite and the subsequent detwinning of the martensitic phase. In contrast to plastic deformation, this process is reversible, which makes superelastic NiTi interesting for applications in which large cyclic strains have to be accommodated [3,4]. In combination with its good biocompatibility this shape memory alloy (SMA) is attractive for medical purposes and used for example for endovascular stents or endodontic files [5–7]. In such applications failure can have severe consequences and thus an appropriate design of the device and adequate material quality are necessary to ensure safe operation. From the materials point of view, thin-structured devices, like endovascular stents, require to keep the number and size of defects as low as possible to avoid initiation sites for crack propagation. However, as structural materials are seldomly defect free and the introduction of flaws may also occur during service, the damage tolerance of SMAs is of great importance. Although this means that the fracture and the fatigue crack growth (FCG) behavior are crucial for designing damage tolerant medical components, only a small number of studies on this aspect is available [8–16]. Furthermore, the comparison of the results is somewhat cumbersome for various reasons: Firstly, tests were performed on NiTi alloys with varying compositions, which affect the phase transition temperatures and thus also the mechanical properties. Even if it was guaranteed that NiTi samples were, for example, tested in their superelastic state, the difference between testing temperature and austenite start temperature can significantly influence the fracture toughness [9]. Furthermore, many experiments were not performed in accordance with testing standards and thus the results do not necessarily represent conservative and size-independent fracture toughness values. This can be caused for example by

- using notches instead of sharp cracks as initial flaws,
- using samples too thin to guarantee the prevalence of plane strain conditions,
- using samples with an insufficient ligament length to ensure the applicability of linear elastic fracture mechanics,
- calculating the fracture toughness from maximum force values in force-displacement curves, rather than applying the evaluation-procedures from standards.

Nevertheless, the data can be used as reference values as long as the experimental circumstances are kept in mind. In this study, sharp and open fatigue pre-cracks were used and the samples adequate dimensions to fulfill the requirements of ASTM standard E1820 and E647 [17,18]. Under quasi-static loading of NiTi, samples do not fail abruptly after reaching a specific load, but exhibit stable crack growth with an increasing crack growth resistance [13]. Therefore, in this paper the entire crack propagation was monitored to be able to determine the crack resistance curve (R-curve) of the material, instead of evaluating only a single measure for the fracture toughness, such as a maximum stress intensity factor.

Concerning the crack propagation behavior of NiTi under quasi-static and cyclic loading several important observations have already been made in previous studies. The latest works indicate that stable martensite and superelastic NiTi have a lower fracture toughness than stable austenite [11]. The quite similar fracture toughness of superelastic and martensitic NiTi is explained by the finding that in the superelastic state

martensite is induced ahead of the crack tip upon loading, regardless whether plane strain or plane stress conditions prevail [11,12,19]. Hence, crack growth in the martensitic phase and fracture toughness of superelastic NiTi seems to be controlled by the properties of the martensite [12].

FCG experiments revealed a strong dependence of the fatigue threshold stress intensity factor range ΔK_{th} on the initial microstructure, with significantly higher ΔK_{th} for stable martensite and reduced threshold values for superelastic austenite and stable austenite [9,20]. Furthermore, a pronounced load ratio dependency was found for ΔK_{th}, with lower threshold values for higher mean stresses [9,20]. FCG behavior in the Paris regime seems to be less affected by the phase and the load ratio, giving Paris exponents between 3 and 4 [9].

A novel strategy to further improve the mechanical and functional properties of shape memory alloys is grain refinement down to the ultrafine-grained (grains smaller than 1 μm) or nanocrystalline regime (grains smaller than 100 nm) [21–24], especially in combination with post-deformation heat-treatments [25,26]. Severe plastic deformation (SPD) techniques, such as equal channel angular pressing (ECAP) or high pressure torsion (HPT), can be used to achieve the desired fine-grained microstructures by imposing large plastic strains. For ultrafine-grained (UFG) and nanocrystalline (NC) NiTi an increase in the yield stress of the martensite and an increase of the transition stress together with large recoverable strains are reported. Concerning the fracture toughness of UFG NiTi only a few studies exist. Ahadi and Sun reported a reduction of fracture toughness with decreasing grain size achieved by thermo-mechanical treatment, especially pronounced for grain sizes below 80 nm [15].

In the present study, UFG NiTi generated by ECAP is investigated with special focus on the damage tolerance. For that fracture toughness and FCG experiments were performed. Since the ECAP-process may lead to anisotropic mechanical properties, samples with different orientations were in use. The main aim of the work is to provide input for a damage tolerant design of components made from UFG NiTi under quasi-static and cyclic loading conditions.

D.2 Material and methods

Experiments were performed with a 50.2% Ni – 49.8 % Ti alloy in the superelastic state, with a martensitic transformation temperature close to room temperature [24]. Microstructure analyses were performed with a *LEO Gemini 1525* scanning electron microscope (SEM), using a secondary electron (SE) and a backscattered electron (BSE) detector. Moreover electron backscatter diffraction (EBSD) was employed. The as-received (AR) material exhibits a microcrystalline microstructure, which is shown in Fig. D-1(a). A mean grain size of about 100 μm was determined from EBSD data, as depicted in Fig. D-1(b). Within the material a large number of Ti-rich precipitates were found with a size of up to a few microns (see dark spots in Fig. D-1(a)). A billet with a diameter of 20 mm of the AR NiTi was subjected to ECAP using route B_C[3] at 450°C for 8 passes, with a channel angle of 110°, imposing a total von Mises strain ε_{vM} of about 6.5. From the AR material, as well as from the ECAPed NiTi tensile samples were taken, with a cross section of 1.5 mm x 1.1 mm and a gauge length of 7.5 mm. The tensile experiments were conducted on a Kammrath and Weiss™ testing machine with a testing speed of 10 μm/s. For fracture experiments, CT specimens were produced from the ECAPed material, with a ligament width W = 9 mm, a thickness of B = 4.5 mm and further dimensions according to the ASTM standard E399 [27] for fracture experiments. Two different orientations, E-R and R-E, as shown in Fig. D-2, were tested in order to take a possible anisotropy of the fracture behavior into account. The sample

[3] For ECAP route B_C the billet is rotated 90° after each cycle.

orientations are denoted according to E399 [27], with the first letter indicating the direction of the crack surface normal and the second letter indicating the crack growth direction. The directions are related to the ECAP process and are visualized in Fig. D-2, with the extrusion direction E and the radial direction R. For FCG tests smaller CT samples (W=5.4 mm, B=1.3 mm and a=1.0 – 1.3 mm) were taken from the AR material and from ECAPed NiTi. Specimens from ECAPed NiTi were prepared with three different orientations (E-R, R-E and R-R), as depicted in Fig. D-2. Notches were introduced with a diamond-wire saw, further sharpened by razor-blade grinding and finally fatigue pre-cracks were introduced under cyclic compression-compression loading with a resonance testing machine (Rumul Russenberger + Müller, Switzerland) at a load ratio of R=(maximum force)/(maximum force)=10. For the fracture experiments the pre-cracks were extended under cyclic tensile loading for 10,000 cycles at ΔK=6 - 8 MPa.m$^{0.5}$ and R=0.3 in order to get a/W-relations of about 0.55. The fracture tests were performed on a Zwick testing machine type 1832 (Zwick Roell, Germany) with a cross head speed of 0.153 mm/min. The toughness of the ECAPed NiTi was evaluated using three different approaches: (i) linear-elastic fracture mechanics and determining the stress intensity factors K_Q from the load-displacement curve, (ii) elastic-plastic fracture mechanics and determining $J_{0.2}$ from the J-integral resistance curve (J-R-curve) at 0.2 mm crack extension and (iii) determining the initiation toughness K_i from the crack tip opening displacement (*CTOD*) as a local fracture parameter. Evaluations (i) and (ii) were performed according to ASTM standard E1820 [17]. Since pre-experiments on the ECAPed NiTi clearly showed extensive ductile behavior, the use of elastic-plastic fracture mechanics was required and crack resistance curves were monitored to account for the stable tearing of the specimens. The crack extension Δa was measured by a direct current potential drop method in order to get J-R-curves and K-R-curves. The blunting line was calculated according to ASTM standard E1820 [17], with

$$J = M\sigma_y \Delta a \tag{1}$$

Where M is a pre-factor with a value of 2 and σ_y is the yield strength of the martensitic phase determined from tensile tests. The J-integral value at a stable crack extension of 0.2 mm was determined ($J_{0.2}$) and converted to a stress intensity factor ($K_{0.2}$) for the specimens by the following relation [28]:

$$K_{0.2} = \sqrt{\frac{J_{0.2}E}{1-\nu^2}} \tag{2}$$

For the Young's modulus E a value of 68 GPa and for the Poisson's ratio ν a value of 0.33 was taken. For the determination of the local fracture toughness stereophotogrammetric images of the fracture surfaces were acquired in the SEM and crack profiles of both specimen halves following identical crack paths were related to each other.

the opposite halves of the samples related to each other. From the profiles the *CTOD* necessary for the coalescence of the first pore with the pre-crack was measured ($CTOD_i$) and taken as criterion for the initiation fracture toughness of the crack growth. Several measurements were performed on different positions of each sample to get information about the variation of the local fracture toughness values. More details about the measurement of $CTOD_i$ can be found in [29]. The $CTOD_i$ can be converted to a J-integral value J_i by [30]:

$$J_i = \frac{1}{d_n}\sigma_y CTOD_i \tag{3}$$

The factor d_n, which depends on the hardening behavior of the material, was taken to be 0.78, as an approximation for a non-hardening material.

The FCG measurements were carried out on an electrodynamic Instron ElectroPuls™ E3000 testing machine at load ratios of R=0.1 and R=0.7. The potential drop technique was applied to monitor the crack lengths during the tests. More details about the testing procedure can be found elsewhere [31,32]. In order to measure the effective threshold stress intensity factor range $\Delta K_{th,eff}$ and the long crack threshold stress intensity factor range ΔK_{th}, the load rising method was applied [33]. $\Delta K_{th,eff}$ is the stress intensity factor range at which first crack growth is detected. During this first crack propagation crack closure mechanisms build-up and reduce the crack driving force at the crack tip. Therefore, retardation or even a stop of the crack growth can occur after short crack advances, which can be interpreted as a cyclic R-curve behavior. When the stress intensity factor range exceeds ΔK_{th} the crack propagates, without stopping, until final failure. With the commonly used load shedding method only the long crack threshold stress intensity factor range, ΔK_{th}, can be determined. After the experiments the fracture surfaces and the side faces of the specimens were analyzed with the SEM.

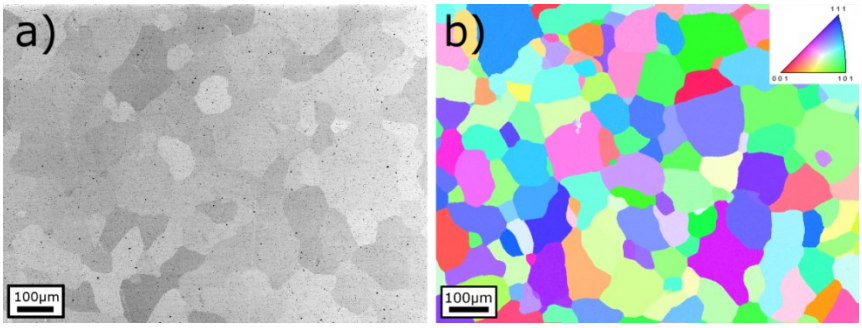

Fig. D-1: Microstructure of the as-received NiTi. a) BSE image of the as-received NiTi, with a grain size of about 100 µm. The black spots are precipitates with a size of up to a few microns. b) Microstructure derived from EBSD data. A cleanup with a minimum grain size of 50 points was applied in order to exclude unsatisfactorily indexed points for the grain size determination.

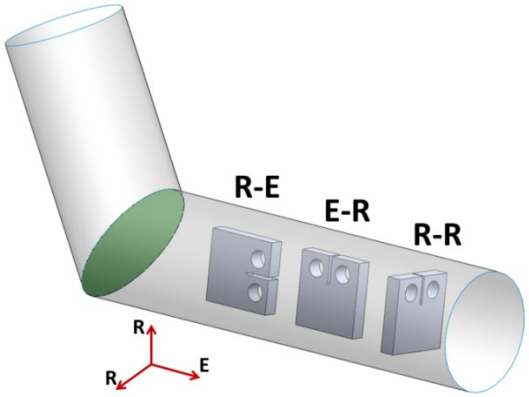

Fig. D-2: Schematic of an ECAP deformed billet and the different sample orientations.

D.3 Results

D.3.1 Microstructure of ECAPed NiTi

BSE and EBSD analyses of the ECAPed NiTi revealed a significant grain refinement, with large fractions of the material exhibiting an UFG microstructure with grain sizes below 1 µm (Fig. D-3). However, also larger-grained areas were detected, with grain sizes up to a few microns, as shown in the lower right parts of

Fig. D-3(a) and (b) and in the EBSD image in Fig. D-3(c). By inspecting the microstructure in radial direction of the billet, elongated structures are revealed, which are about 45° inclined to the extrusion direction (Fig. D-3(d-f)). The grain refinement was accompanied by an increase in hardness of about 25%, from 237±10 HV 0.5 in the as-received state, to 296±7 HV 0.5 for the ECAPed NiTi. A Young's modulus of 67.6 ± 0.8 GPa was obtained by nanoindentation (Nano Indenter G200, Keysight Technologies, USA) using a Berkovich tip and following the analysis procedure proposed by Oliver and Pharr [34].

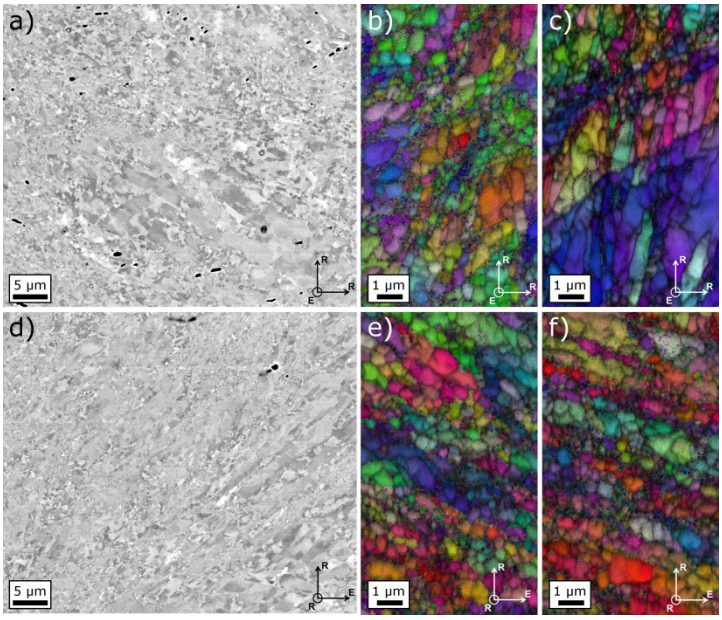

Fig. D-3: Microstructure of the ECAPed NiTi shown with BSE (a & d) and EBSD (b,c,e,f) images. Images (a – c) were taken in the viewing direction parallel to the extrusion direction, in images (d – f) the viewing direction was parallel to the radial direction.

D.3.2 Tensile tests

Tensile tests on AR and ECAPed NiTi show that grain refinement leads to a higher transformation stress σ_{tr} and to a higher yield strength of the martensitic phase σ_y. Exemplary stress-strain curves for AR and ECPAed NiTi are shown in Fig. D-4. The stress of the martensitic phase transformation is increased from 180 ± 14 MPa in the AR state to 283 ± 62 MPa in the ECAPed state. The yield stress of the martensitic phase in AR NiTi gets increased by ECAP deformation from 467 ± 79 MPa to 1216 ± 73 MPa. The ductility in terms of elongation to fracture is only marginally affected by the SPD processing.

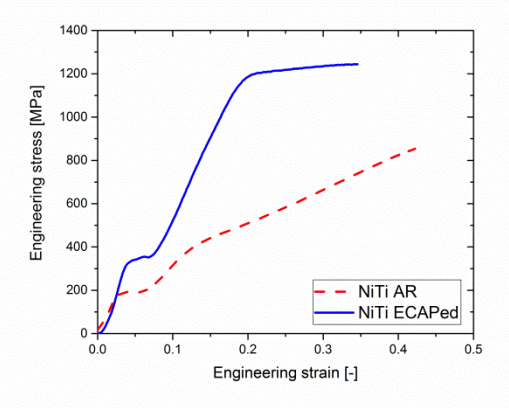

Fig. D-4: Examplary stress – strain curves of AR and ECAPed NiTi.

D.3.3 Fracture experiments

As described in section 2, the fracture behavior of ECAPed NiTi was assessed by three different approaches and an overview of the results is given in Table D-1. Fracture surface analyses revealed that a local *CTOD* of 1.0 to 4.5 µm and 0.7 to 4.6 µm is necessary to initiate crack growth in the R-E and R-E sample, respectively. From the *CTOD* values stress intensity factors at crack initiation (K_i) were calculated, ranging from about 11 to 29 MPa.m$^{0.5}$. The K_Q values determined from the load-displacement curves in Fig. D-5(a) and (b) are in the range of 19.7 (R-E) to 22.0 MPa.m$^{0.5}$ (E-R). Similar to the K_i value, also the K_Q value shows little dependence on the orientation of the specimens, with only about 10 % difference between both orientations. For the comparison with results from literature K_{max} was calculated from the maximum force in the load-displacement curve. The orientational variation of the K_{max} values is small, with a difference of less than 10 % (32.0 MPa.m$^{0.5}$ for the R-E and 29.3 MPa.m$^{0.5}$ for the E-R sample).

Table D-1: *CTOD*, *J*-integral and *K* values obtained from the fracture experiments on ECAPed NiTi.

	COD_i [µm]	J_i [kJ/m^2]	K_i [MPa.m$^{0.5}$]	K_Q [MPa.m$^{0.5}$]	$J_{0.2}$ [kJ/m^2]	$K_{0.2}$ [MPa.m$^{0.5}$]	K_{max} [MPa.m$^{0.5}$]
R-E	1.0 - 4.5	1.1 - 5.1	11.6 - 24.7	19.7	22.4	41.3	32.0
E-R	0.7 - 4.6	0.8 - 5.2	9.7 -25.0	22.0	18.0	37.1	29.3

The J-integral plotted against the crack extension (J-R-curves) in Fig. D-5(c) and (d) clearly shows a rising R-curve behavior, i.e. the crack growth resistance increases with crack extension. In order to quantify the crack growth resistance during stable crack propagation, $J_{0.2}$ values were obtained from the intersection of the blunting line shifted to 0.2 mm crack extension with the *J*-R-curve. Stress intensity factor values calculated from $J_{0.2}$ were found to be up to two times higher than K_Q and K_i. From this evaluation a 10 % higher toughness value $K_{0.2}$ for sample orientation R-E was determined (41.3 MPa.m$^{0.5}$) compared to E-R (37.1 MPa.m$^{0.5}$). The initiation and fracture toughness expressed as J-integral values were found to be in the range of 1.1 to 7.2 kJ/m² for the initiation toughness J_i and 18.0 to 22.4 kJ/m² for $J_{0.2}$. The R-curves are also plotted in Fig. D-6 in terms of *K* over the crack extension measured by potential drop (*K*-R-curves), although the validity of *K* after the crack initiation will be discussed in section 4.1.1.

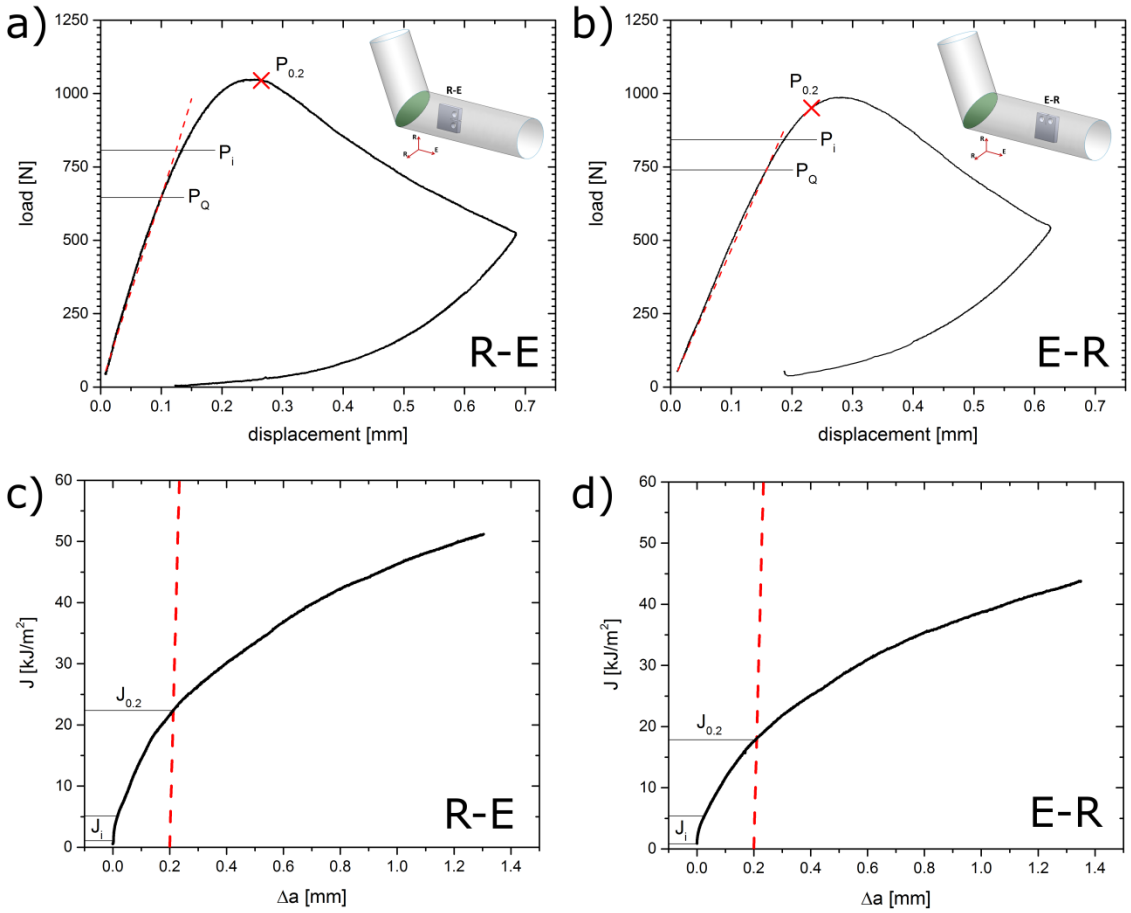

Fig. D-5: Fracture behavior of the two different orientations of ECAPed NiTi. (a) and (b) show the load-displacement curves of the ECAPed NiTi CT samples, with orientation R-E and E-R, respectively. The intersections with lines of 95% initial slope are marked by P_Q. In (c) and (d) the *J*-R-curves of the two orientations are presented. The initiation toughness calculated from the $CTOD_i$ value is marked by P_i and J_i, the load and *J*-integral value at 0.2 mm crack extension is marked by $P_{0.2}$ and $J_{0.2}$.

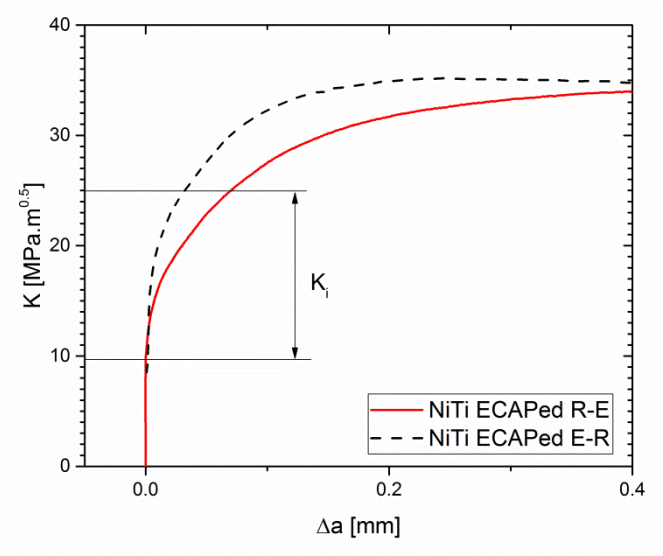

Fig. D-6: *K*-R-curves of the two tested orientations. The crack extension Δa was obtained from potential drop measurements. The range of the initiation toughness values is marked by K_i.

The fracture surface images in Fig. D-7 reveal a clear difference between the fatigue pre-crack and the overload fracture. The fracture surface of the fatigue pre-crack is characterized by transgranular fracture with small ridge-like features. In contrast to that, ductile shallow dimples are observed for the overload fracture with diameters of a few micrometers. Only in few cases inclusions or precipitates can be found as initiation sites for dimple formation. More often single grains or the contour of several grains are visible in the center, as for example shown in Fig. D-7c), which suggests that nanovoids are initiated at grain boundaries. This is supported by simulation studies of NC and UFG microstructures, which predict the formation of voids at grain boundaries and triple junctions [35,36].

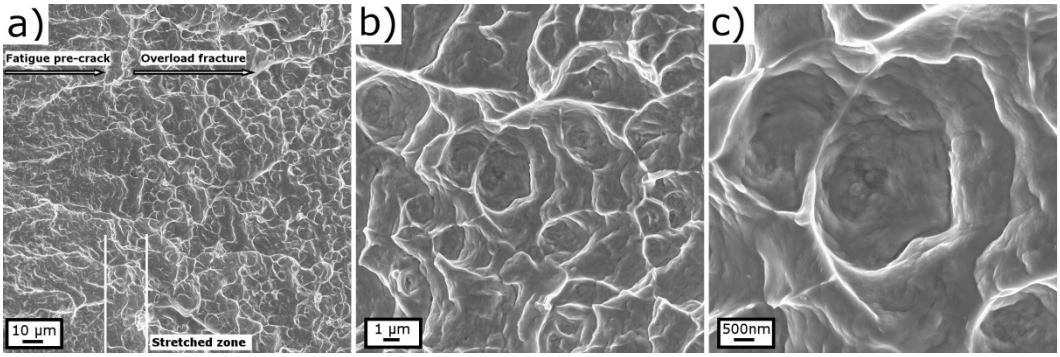

Fig. D-7: SEM images of the fracture surface of an ECAPed NiTi sample. In a) the transition from the fatigue pre-crack to the overload fracture is shown and marked by arrows. Furthermore, the stretched zone is marked in the lower part of the image. Transgranular fracture is visible in the pre-crack area. The region of the overload fracture exhibits ductile dimples, as shown in b) and c) under higher magnification.

D.3.4 FCG experiments

FCG curves of AR NiTi and ECAPed NiTi, tested at R=0.1 and R=0.7 are presented in Fig. D-8. For AR NiTi, as well as for all orientations of ECAPed NiTi a clear mean stress dependency can be observed. The ΔK_{th} and $\Delta K_{th,eff}$ values coincide for all samples tested at R=0.7. In contrast, at lower mean stresses all samples

show pronounced cyclic R-curve behavior for the threshold of the stress intensity factor range, which means that $\Delta K_{th,eff}$ and ΔK_{th} values differ. From the threshold values summarized in Table D-2 it can be seen that the $\Delta K_{th,eff}$ values for both load ratios and all sample orientations and microstructures show negligible small variations between 0.8 and 1.1 MPa.m$^{0.5}$. More pronounced differences can be observed for ΔK_{th}, with the lowest for ECAPed NiTi with orientation R-R (1.3 MPa.m$^{0.5}$) and the highest for ECAPed NiTi with orientation E-R (2.4 MPa.m$^{0.5}$). For orientation R-E an additional sample was tested at R=0.1 and a difference of 27 % was found for the ΔK_{th} values of the two specimens (1.6 and 2.2 MPa.m$^{0.5}$). This reveals that the variation of the ΔK_{th} values of the different orientations is comparable to the scatter of ΔK_{th} values.

In the Paris regime the FCG curves of all tested samples, regardless of the microstructure and their orientation, can be fitted with the Paris law (Equ. 4) and an exponent m close to 3.

$$\frac{da}{dN} = C * \Delta K^m \tag{4}$$

In Fig. D-8(a) dashed guidelines for a proportionality of the FCG rate da/dN to ΔK^3 are fitted to data of AR NiTi. The same guidelines are also shown in the FCG diagrams of ECAPed samples in Fig. D-8(b-d) for comparison. It can be observed that at R=0.7 (filled symbols in Fig. D-8) the FCG rate of AR NiTi is higher than in the case of ECAPed samples. For orientations with crack growth in radial direction (R-R and E-R specimens) the FCG rates in the Paris regime are even reduced by a factor of 2 to 3, compared to AR NiTi. At low mean stresses (R=0.1, open symbols in Fig. D-8) the FCG rates during stable crack growth are comparable for all tested microstructures and orientations, with slightly faster FCG of ECAPed NiTi with R-E orientation. In summary, differences between the tested samples are in general small, however, at R=0.7 ECAPed samples exhibit slower FCG compared to the AR state. Furthermore, a common $\Delta K_{th,eff}$ value of about 1 MPa.m$^{0.5}$ was found for all tested specimens. The long-crack threshold values ΔK_{th} vary even for different samples from the same microstructure and orientation.

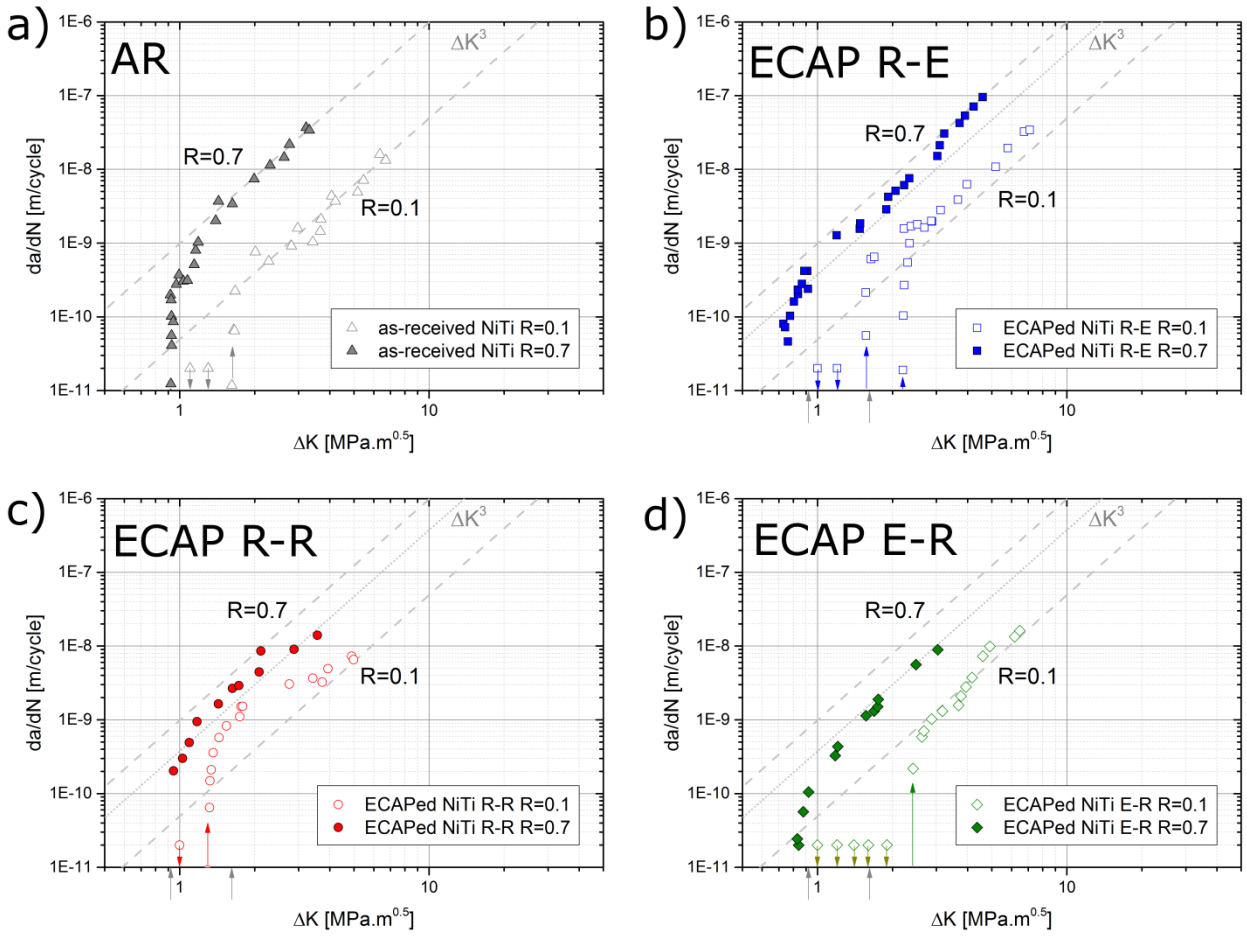

Fig. D-8: FCG diagrams of 50.2%Ni-49.8%Ti measured at R=0.1 and R=0.7. a) FCG curves of the as-received NiTi. b) – d) FCG curves of the ECAPed NiTi with different sample orientations. ΔK values, at which crack advance was detected but the crack was stopped, are marked by arrows pointing downwards. Arrows pointing upwards mark the ΔK_{th} values. The ΔK_{th} values of as-received NiTi at R=0.1 and R=0.7 are shown for comparison in the FCG diagrams of ECAPed NiTi and are marked by gray arrows underneath the ΔK-axis. The gray dashed lines are guidelines for the FCG data of the as-received NiTi in the Paris regime and are also shown in the diagrams of the ECAPed NiTi for comparison.

Table D-2: Effective threshold stress intensity factor ranges $\Delta K_{th,eff}$ and long-crack threshold stress intensity factor ranges ΔK_{th} of AR and ECAPed NiTi with different orientations, determined at load ratios of R=0.1 and R=0.7. For all samples tested at R=0.7 the $\Delta K_{th,eff}$ and ΔK_{th} values coincide.

[MPa.m$^{0.5}$]	R=0.7	R=0.1	
	$K_{th,eff} = K_{th}$	$K_{th,eff}$	K_{th}
AR Niti	0.9	1.1	1.6
ECAPed NiTi R-E	0.8	1.0	1.6 - 2.2
ECAPed NiTi R-R	1.0	1.0	1.3
ECAPed NiTi E-R	0.8	1.0	2.4

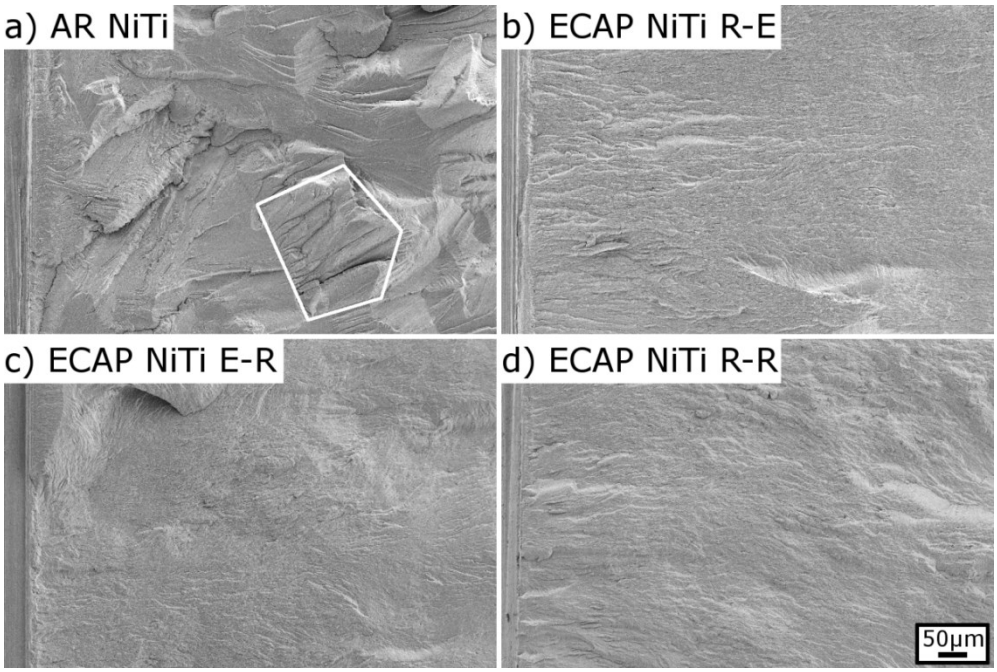

Fig. D-9: SEM images of the fatigue fracture surfaces of samples tested at R=0.1 in the threshold and lower Paris regime. (a) Fracture surface of AR NiTi. (b-d) Fracture surfaces of ECAPed NiTi samples with R-E, E-R and R-R orientation. All images were taken at the same magnification, with the scale shown in (d). The crack propagated from left to right.

From the images of the fracture surfaces in Fig. D-9 it is obvious, that AR NiTi exhibits a significantly rougher fracture surface compared to ECAPed NiTi samples. In AR NiTi the crack propagated by transgranular fracture along crystallographic planes, which can be seen as ledges on the fracture surface. Grains can be recognized as areas, where ledges appear to be parallel, as for example marked in Fig. D-9(a). The fracture surfaces of the differently oriented ECAPed NiTi samples have in common that they are smoother and exhibit smaller topographic features than AR NiTi. Nevertheless, the fracture surfaces appear inhomogeneous, as there exist very flat areas, but also regions with ledges (see Fig. D-9(b-d)). In Fig. D-10 SEM images of the fracture surfaces of the three differently oriented samples taken at higher magnifications are presented, which reveal that they have microscopically a similar appearance. Crack propagation occurred by transgranular fracture and no grain structure is visible.

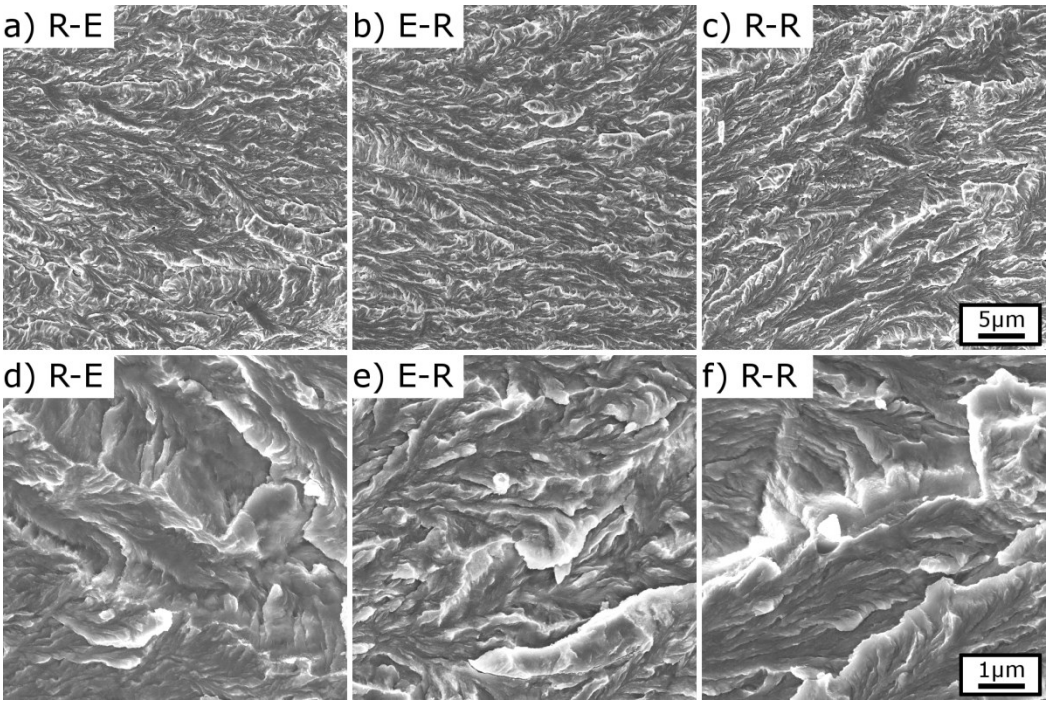

Fig. D-10: SEM images of the fracture surfaces of ECAPed NiTi with R-E (a,d), E-R (b,e) and R-R(c,f) orientation. Small features from transgranular fracture can be observed, with no pronounced differences between the three sample orientations.

In order to assess the roughness of the crack path, the side faces of the CT specimens of the ECAPed material were studied in the SEM, see Fig. D-11. A small crack path tortuosity is found for all orientations, however, also crack branching and therefore secondary cracks can be observed, which stopped after short crack advances. The crack path of the E-R sample in Fig. D-11(c) appears slightly smoother than for the other two orientations, however, due to the observed inhomogeneity of the fracture surface the representativeness of these crack paths is limited. Nevertheless, they give a rough impression of the overall crack path tortuosity.

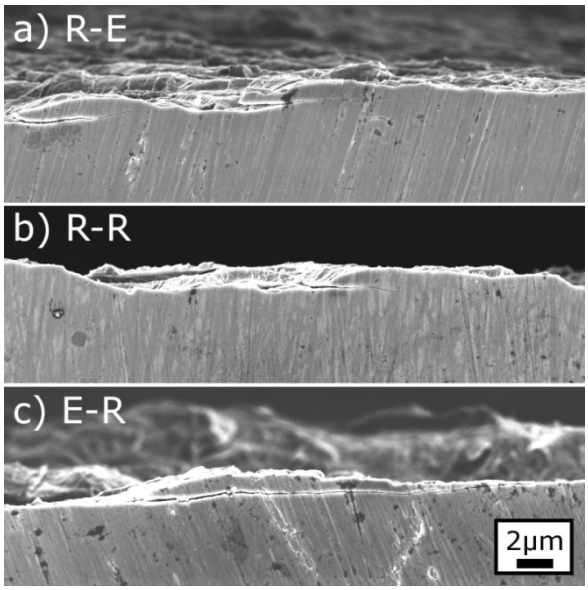

Fig. D-11: SEM images of the side faces of ECAPed NiTi samples with different orientations, tested at R=0.1. The images show the crack paths at ΔK between 1.6 and 2.1 MPa.m$^{0.5}$.

D.4 Discussion

In the following the results of the fracture and FCG experiments on ECAPed NiTi will be discussed and compared to the coarse-grained material state. Special focus is devoted to the orientation dependence of these properties.

D.4.1 Fracture behavior

By combining the different test and evaluation methods as described in section 2 and 3.3 the fracture process in superelastic ECAPed NiTi was attempted to be comprehensively studied on the differently oriented samples. Characteristic values for the fracture process based on different concepts have been determined, however, their validity has to be scrutinized.

D.4.1.1 Some remarks to the validity of fracture toughness measurements

In general, the thickness (B) of the samples, as well as the width of the remaining ligament (W-a) have to be large enough to ensure the applicability of linear-elastic fracture mechanics and the dominance of small scale yielding. According to ASTM E399 [27] this is guaranteed, if the following condition is fulfilled:

$$B, W-a > 2.5*(K/\sigma)^2 \qquad (5)$$

with K being the stress intensity factor and σ the stress describing the deviation from linear-elastic behavior. For classic ductile metals the yield strength can be taken for σ. For superelastic NiTi, however, the first deviation from elastic behavior occurs at the transformation stress σ_{tr}, due to the phase transformation from austenite to martensite. By considering σ_{tr} for the calculation of the limit of linear elastic fracture mechanics it can be shown that K values are valid up to only 12 MPa.m$^{0.5}$ for the sample geometry given in section 2. As this is lower than the measured K values, the application of elastic-plastic fracture mechanics and the determination of a critical J-integral value appears be more appropriate. Additionally, for the determination of a valid K_{IC} value, a relation P_{max}/P_Q smaller than 1.10 is required as well in order to guarantee

small scale yielding conditions. This requirement is not fulfilled by the fracture experiments of the present study. Nevertheless, K_Q values, which represent lower limit values for the fracture toughness, are taken for the comparison of the toughness of differently oriented samples. Therefore, the results will be discussed in respect to critical stress intensity factors, as well as *J*-integral values.

Furthermore, it should be taken into account that the crack tip opening displacement determined from post-fracture investigations of the fracture surface underestimates the fracture toughness of shape memory alloys. Due to the superelasticity of NiTi, even the deformation up to large strains of about 10 % is fully reversible. Thus, the *CTOD* measured on the fracture surface, which can be regarded as the *CTOD* in the unloaded state, could be significantly smaller than at maximum load. In contrast to that, in classical elastic-plastic material the elastic relaxation is negligible small. Therefore, toughness values determined from the *CTOD* measurements in NiTi can only be regarded as conservative lower limits for the crack initiation. To conclude, the quantitative description of the fracture process has to be cautiously treated.

D.4.1.2 Fracture process

During the loading of the specimens elastic deformation of the preexisting austenite occurs, which corresponds to the linear part of the load-displacement curves. A deviation from linearity follows at loads around 500 N, which is equivalent to stress intensity factor values of about 15 MPa.m$^{0.5}$ for both samples. This non-linearity can be caused by three different mechanisms: (i) stress induced transformation from austenite to martensite, (ii) plastic deformation, i.e. blunting of the crack tip and (iii) crack initiation and propagation. Synchrotron X-ray diffraction experiments [11] and thermographic measurements [12] revealed that martensite is induced in an limited area ahead of the crack tip before plastic deformation or crack growth was detected. Thus, a certain contribution to the first deviation from linearity would be caused by this stress induced superelastic martensitic transformation. The authors in [11] could not detect blunting of the crack tip by viewing the side faces of the specimen during the experiment and argued that the deviation from linearity is solely a result of the phase transformation. This, however, is not confirmed by the fracture surface observations of the present study, which clearly show that the fatigue pre-crack is followed by a stretched zone, which is commonly accepted to be a result of the blunting of the crack tip (see Fig. D-7). Furthermore, the analyses of stereophotogrammetric images of the fracture surfaces reveal, that a CTOD of 1 µm to 5 µm remains after the crack started to propagate. From these *CTOD* values it can be estimated that the initiation toughness K_i lies at least in the range of about 10 to 25 MPa.m$^{0.5}$. However, at maximum load, i.e. before a back-deformation can occur, the *CTOD* is even higher and thus the K_i determined from the remaining *CTOD* in the unloaded state can only be a lower limit, as discussed in section 4.1.1. Nevertheless, the K_i values correlate well with the measured R-curves based on the stress intensity factor *K* in Fig. D-6, which show first crack advance for a *K* of 10 to 15 MPa.m$^{0.5}$ and give a lower bound for the crack initiation. When the upper bound of K_i, calculated from the largest measured $CTOD_i$, is inserted into the R-curve, it can be seen that the crack has overall already extended up to 200 µm. However, the measured crack extension by potential drop is always an averaged quantity and therefore, an overall crack propagation can be detected, although not the whole crack front has advanced. The crack could grow, for example, along certain areas of the crack front; in other parts, however, the crack faces can still be connected and further blunted, which can finally be detected as crack paths with larger *CTOD*. The K value corresponding to the largest measured *CTOD* is needed for the crack to grow along the entire crack front. During further stable crack propagation the crack growth resistance increases until a plateau of about 35 MPa.m$^{0.5}$ is reached. This *K*-based description is very useful to explain the onset of crack growth in a deformation regime, where small scale yielding can still be applied. In order to take

the pronounced plastic deformation into account it is required to apply elastic-plastic fracture mechanics and assess the toughness and crack growth resistance in terms of the *J*-integral. Fig. D-5(c-d) show the rising *J*-R-curves of the ECAPed NiTi, i.e. the crack growth resistance is increasing during stable crack advance. In order to compare the R-curves, the *J* values at a crack advance of 0.2 mm are determined and marked as $J_{0.2}$ in the diagrams. Converted to stress intensity factors $K_{0.2}$ these values are with 37 to 41 MPa.m$^{0.5}$ even higher than the plateau values of the *K*-R-curves, which is clear as the K-description can only deliver lower bound values due to the loss of small scale yielding conditions.

For a comparison to other studies also K_Q values, according to ASTM standard E1820 [17] and K_{max} values calculated from the maximum load of the load-displacement curves were calculated. The K_Q values lie in the range of 19.7 to 22.0 MPa.m$^{0.5}$ and are therefore higher than the lower bound of the initiation toughness determined from *CTOD* and from the *K*-R-curves. K_{max} values are closer to the plateau-value of the *K*-R-curves with 29.3 to 32.0 MPa.m$^{0.5}$.

In order to assess the orientation dependence of the fracture behavior of ECAPed NiTi, the toughness values and R-curves of the two differently oriented specimens are compared. $CTOD_i$ values vary in the same range for both orientations and the plateau values of the *K*-R-curve show a difference of only about 3 %. The R-E sample shows slightly steeper R-curves than the E-R sample and therefore also higher $J_{0.2}$ and $K_{0.2}$ values. To conclude, a weakly pronounced anisotropy of the fracture toughness is observed in ECAPed NiTi, especially compared to other UFG materials, which, however, were deformed to larger strains (see for example UFG iron [37] or nickel [32], both processed by HPT). Furthermore, the more equiaxed grain shape due to the ECAP deformation route B_C seems to reduce the orientation dependency of the UFG NiTi. In contrast to that, UFG iron deformed by ECAP route A exhibited more strongly elongated grains and therefore also a pronounced orientation dependent fracture behavior [38].

Furthermore, the results were compared to studies from literature to see the effect of the ECAP deformation on the fracture behavior of NiTi. In [11] a mean K_{max} value of 34 MPa.m$^{0.5}$ was measured for superelastic NiTi, which is only slightly higher than the results obtained in the present study. Also the K_{max} values of 20 to 35 MPa.m$^{0.5}$ from [16] on NiTi with a few microns grain size are in good accordance, although one has to note that in this study the thickness of the samples was only 640 µm and the notch radius was very large with 100 µm, instead of a sharp pre-crack, as used in this study. *K*-R-curves were measured in [13,15] for microcrystalline down to nanocrystalline NiTi. Samples of flattened commercial NiTi tubing [13] exhibited a initiation toughness K_i of 10 to 16 MPa.m$^{0.5}$, which is in good agreement with the measurements of the ECAPed NiTi. In [15] clearly higher initiation toughness values (K_i = 42 to 46 MPa.m$^{0.5}$) and steeper *K*-R-curves are reported for NiTi with a grain size between 80 nm and 1500 nm. However, specimens were prepared from a sheet with a thickness of 1 mm only and thus, with respect to the strength of the material, plane stress conditions were dominating, which results in higher measureable fracture toughness values. Furthermore, the crack length was measured optically on the side faces of the specimen. This measurement method is less sensitive to small crack advances than the PDT and cannot monitor crack advance in the interior of the sample, where plane strain conditions control the crack growth. Therefore it might be possible, that small crack advances occurred already before the reported K_i values.

The conclusion of this the comprehensive comparison between the majority of studies on commercially available coarse-grained NiTi and the present results is that the increase in strength resulting from ECAP deformation has no observable detrimental effect on the fracture behavior of NiTi.

D.4.2 Fatigue crack growth behavior

In the following discussion of the FCG behavior it will be distinguished between intrinsic and extrinsic toughening mechanisms [39]. Intrinsic mechanisms determine the resistance against material separation, which can be influenced by microstructural aspects, such as grain size, texture and grain boundary morphology. Extrinsic mechanisms act behind the crack tip and reduce the load, for example by crack closure or other shielding mechanisms like crack branching [39].

D.4.2.1 Intrinsic FCG resistance

All experiments were started with short and open cracks from compression pre-cracking and thus it can be assumed that contributions from crack closure are minimized for the determination of the $\Delta K_{th,eff}$ values, i.e. prior to the first crack advance [33]. The results in Table D-2 show that grain refinement and the sample orientation have no significant effect on the $\Delta K_{th,eff}$ values, regardless of the mean stress. This is in good accordance to theory, which predicts that the effective threshold of ductile metals should only be dependent on the load amplitude necessary for the emission of dislocations from the crack tip and their return [40]. In the near-threshold regime at a ΔK of 1 MPa.m$^{0.5}$ the size of the cyclic plastic zone of AR NiTi and ECAPed NiTi can be estimated to be 50 nm and 30 nm, respectively (estimation of Irwin for plane strain conditions [41]). This is substantially smaller than the mean grain size of the two microstructures and hence grain boundaries, which are important for the strength of the material, play a minor role, as dislocation movement in general takes place within the grains. Therefore $\Delta K_{th,eff}$ values are not strongly influenced by the strength of the material, but by the elastic properties such as the Young's modulus, which can be assumed to stay constant during grain-refinement down to the UFG state.

FCG data from experiments at R=0.7 can be taken to assess the intrinsic FCG resistance during further crack propagation (filled symbols in Fig. D-8), since crack closure plays a minor at high mean stresses with resulting large crack tip opening displacements. It is obvious from the FCG diagrams in Fig. D-8 that ECAPed NiTi samples, regardless of their orientation, show lower FCG rates compared to AR NiTi (see dashed fit lines of AR NiTi). There is less difference for R-E samples (factor 2 to only slightly slower) than for R-R and E-R samples, which exhibit slower FCG by a factor of up to 3. In order to understand the effect of grain refinement on the FCG rate, the microscopic fracture mechanisms have to be investigated. From the fracture surface analysis it can be clearly seen, that grain refinement does no change the fracture mode and transgranular fracture is observed for the AR NiTi, as well as for the ECAPed NiTi. As both material states exhibit pronounced ductility, cycle by cycle FCG through a blunting and re-sharpening process can be expected, which is typical for ductile metals [42–44]. With that assumption the relation for the FCG rate da/dN, the cyclic crack tip opening displacement $\Delta CTOD$, the stress intensity factor range ΔK, σ_y the yield strength and E the Young's modulus can be expressed as follows:

$$\frac{da}{dN} \propto \Delta CTOD \propto \frac{\Delta K^2}{2\sigma_y E} \tag{6}$$

When the fracture mechanism and the Young's modulus are not changed by the grain refinement, the FCG rate is proportional to $1/\sigma_y$ (see Equ. 6). The FCG rate for the ECAPed NiTi can be estimated from the ratios of the yield strengths by the following relation:

$$\left(\frac{da}{dN}\right)_{ECAPed} \cong \frac{\sigma_y^{AR}}{\sigma_y^{ECAPed}} \left(\frac{da}{dN}\right)_{AR} \cong 0.38 \left(\frac{da}{dN}\right)_{AR} \tag{7}$$

Equ. 7 predicts 60% lower FCG rates in the Paris regime for the ECAPed NiTi compared to the AR NiTi, represented by the dotted lines in the FCG diagrams of ECAPed NiTi in Fig. D-8(b-d). This estimation seems appropriate for ECAPed NiTi samples with orientations E-R and R-R. For the orientation R-E, however, the FCG rates are higher than expected. It seems, that in R-E samples the crack can more easily follow the elongated grain structures, which therefore might reduce the intrinsic FCG resistance. Nevertheless, the tendency for a lower FCG of ECAPed NiTi compared to AR NiTi seems to be explicable by its higher strength and the reduced $\Delta CTOD$ in the blunting and re-sharpening process (see Equ. 6 and 7).

D.4.2.2 Extrinsic toughening mechanisms

The difference between the ΔK_{th} values, as well as the variation of the FCG rates in the Paris regime at R=0.1 and R=0.7 gives information about the contribution of crack closure and shielding mechanisms. In FCG tests at low mean stress (e.g. R=0.1) the crack tip opening displacement is small and often less or in the range of the size of asperities of the fracture surface, oxide debris or the plastic wedge, which builds up at the crack tip in ductile metals. These crack closure mechanisms, which are called roughness induced crack closure (RICC), oxide induced crack closure (OICC) and plasticity induced crack closure (PICC), respectively, are responsible for pre-mature contact of the crack faces upon unloading and reduce the load amplitude at the crack tip. Therefore, due to active crack closure a higher ΔK has to be applied globally in order to achieve the same loading conditions as without closure or in experiments at higher mean stresses. Thus, higher ΔK_{th} values are measured at R=0.1 than at R=0.7 and the difference can be ascribed to crack closure mechanisms. The same is true for the FCG rate in the Paris regime, where at the same ΔK slower crack propagation is observed for lower mean stress or lower R-ratios.

As can be seen in Fig. D-8 and Table D-2, at R=0.1 the ΔK_{th} of ECAPed NiTi samples was found to be close to the ΔK_{th} of AR NiTi, with 0.3 MPa.m$^{0.5}$ lower and 0.8 MPa.m$^{0.5}$ higher threshold values at a maximum, depending on the sample orientation. The FCG rates in the Paris regime are slightly higher for R-E and R-R oriented ECAPed NiTi samples or quite similar for E-R specimens, compared to the AR NiTi. This indicates that the reduction in grain size does not strongly influence the contribution of crack closure. From the fracture surface images in Fig. D-9 one could expect that the contribution of RICC is severely reduced for ECAPed NiTi, as the fracture surfaces are smoother and asperities are smaller than in AR NiTi. However, the crack tip opening displacement is still smaller or in the range of the asperities and hence RICC seems to have a similar contribution as in AR NiTi. PICC is expected to be the same for un-deformed and ECAP-deformed NiTi, as long as no grain growth and cyclic softening occurs ahead of the crack tip [31,45], which was indeed not observed. Also the contribution of shielding mechanisms, such as transformation toughening from phase transitions or geometric shielding from crack deflection or crack branching, cannot be significantly reduced, as the FCG curves of ECAPed NiTi are quite similar to those of AR NiTi.

D.4.2.3 Inhomogeneity and orientation dependence

Microstructure analyses of the ECAPed NiTi reveal that in general grains are smaller than 1 μm, however also areas with larger grains exist (see Fig. D-3). To investigate the impact of this microstructural variation on the FCG behavior, two R-E samples of ECAPed NiTi were tested with the same parameters. The results show a significant scatter in the FCG data, especially for the long crack threshold values ΔK_{th} and the FCG rates in the near-threshold regime, which are more strongly influenced by the microstructure (see Table D-2 and Fig. D-8(b)). Two R-E samples showed differences in their ΔK_{th} values of about 0.6 MPa.m$^{0.5}$ or about

25%. This magnitude of scatter is in the range of the variations of the FCG data of the differently oriented samples. Therefore, no significant anisotropic FCG behavior is noticable for the ECAPed NiTi.

D.4.2.4 Comparison to coarse-grained NiTi

In Fig. D-12 the FCG data of the as-received 50.2 Ni – 49.8 Ti (at. %) of the present study is shown together with data from literature for 50.0 Ni – 50.0 Ti (at. %) [20]. FCG experiments on 50.0 Ni – 50.0 Ti were performed at different temperatures, in order to test the material in its superelastic and its martensitic state. Although the composition varies slightly, the FCG data of the present AR NiTi is in good accordance with the data for superelastic NiTi from literature and clearly different from the data of the martensitic NiTi. This reveals that small variations of the composition do not strongly affect the FCG behavior of NiTi, as long as the same phase is present at the testing temperature.

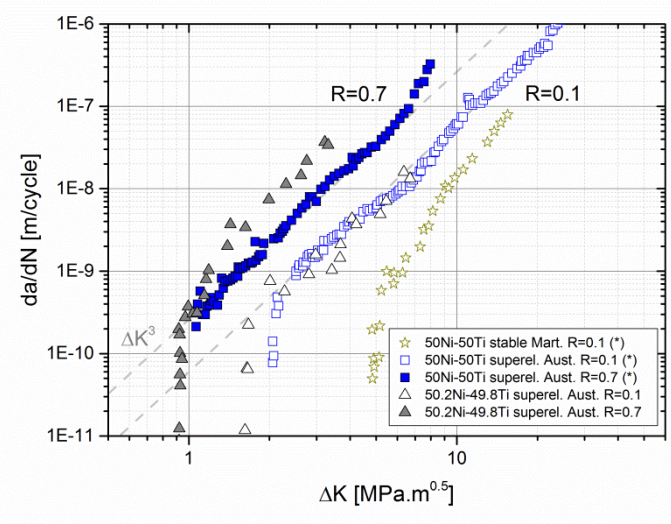

Fig. D-12: Comparison of FCG data of 50.2 Ni - 49.8 Ti (at. %) measured in the present study (triangles) with data for 50.0 Ni – 50.0 Ti (at. %) from [20], tested in its superelastic and martensitic state (squares and stars, marked by *).

D.4.3 Comparison to other UFG and NC materials

ECAP processing of the present nickel-titanium alloy leads to an increase in hardness and strength of about 25%, without significantly deteriorating the damage tolerance of the material. This is in contrast to findings of previous studies on severely plastically deformed UFG nickel and ARMCO iron, where a weak crack path with reduced FCG resistance was reported. However, it has to be noted that the introduced strain is significantly lower for the NiTi (8 passes of ECAP, von Mises strain ε_{vM} of about 6.5), compared to the HPT deformed Ni and Fe (15 revolutions HPT, von Mises strain ε_{vM} of 10 to 70). Therefore, less grain refinement is observed for NiTi, which seemingly preserves transgranular fracture. In contrast to that, the small grain size in UFG Ni and Fe promotes intergranular fracture, which seems to reduce the FCG resistance. Furthermore, the grains of the ECAPed NiTi are less elongated than in the cases of UFG Ni and Fe, which is likely due to the absence of orientation dependent behavior in ECAPed NiTi.

D.5 Conclusions

ECAP deformation at elevated temperatures of NiTi is a beneficial treatment to increase the strength of NiTi without significantly deteriorating its fracture and FCG behavior. Comprehensive fracture experiments

reveal that crack initiation starts at a J-integral value of about 1.1 kJ/m and a stress intensity factor of about 10 MPa.m$^{0.5}$. However, crack growth resistance increases during stable crack propagation, i.e. ECAPed NiTi exhibits a rising R-curve. A plateau of 35 MPa.m$^{0.5}$ was found for the K-R-curve, which is comparable to data for coarser-grained NiTi from literature. Applying the concept of elastic-plastic fracture mechanics, a J-integral value of about 20 kJ/m² was determined for a crack extension of 0.2 mm, which corresponds to a $K_{0.2}$ of about 40 MPa.m$^{0.5}$. FCG experiments show that ECAP deformation of NiTi can be beneficial for the FCG behavior, as it results in a higher intrinsic crack growth resistance under cyclic loading due to the increase in strength and the consequential reduction of the cyclic crack tip opening displacements. This results in slower crack propagation in the Paris regime for tests at high mean stresses for ECAPed NiTi, compared to the AR material. However, crack closure contributions seem to be somewhat reduced by the grain refinement and thus a tendency to faster crack advance was observed for FCG in ECAPed NiTi at low mean stresses. Effective threshold values $\Delta K_{th,eff}$ are not influenced by the ECAP process and show only little variation, regardless of the grain size of the microstructure and the sample orientation. The long crack threshold values ΔK_{th} of ECAPed NiTi show larger scatter, which seems to be an effect of the inhomogeneous microstructure. In total, ΔK_{th} values of ECAPed NiTi are close to the threshold value of AR NiTi or even higher and no clear orientation dependence of the fracture and FCG behavior was observable for ECAPed NiTi.

Further grain refinement and stronger elongation of the grains is expected to further improve the strength. However, care has to be taken as the damage tolerance of NiTi could get deteriorated, as more severely deformed UFG and NC materials are prone to intergranular fracture and to a strong reduction of the FCG resistance and the contribution of crack closure mechanisms.

D.6 Acknowledgments

Funding of this work has been provided by the European Research Council under ERC Grant Agreement No. 340185 USMS and by the Austrian Science Fund in the framework of research project P26729-N19. The authors would like to gratefully acknowledge Dr. Verena Maier-Kiener and Alexander Leitner for performing nanoindentation tests on the material.

D.7 References

[1] W.J. Buehler, F.E. Wang, A summary of recent research on the Nitinol alloys and their potential application in ocean engineering, Ocean Eng. 1 (1968) 105–120.

[2] C.M. Jackson, H.J. Wagner, R.J. Wasilewski, The alloy with a memory, 55-Nitinol: Its physical metallurgy, properties, and applications, Nasa Rep. SP 5110 (1972).

[3] K.. Melton, O. Mercier, Fatigue of NITI thermoelastic martensites, Acta Metall. 27 (1979) 137–144.

[4] G. Eggeler, E. Hornbogen, A. Yawny, A. Heckmann, M. Wagner, Structural and functional fatigue of NiTi shape memory alloys, Mater. Sci. Eng. A. 378 (2004) 24–33.

[5] S.A. Shabalovskaya, On the nature of the biocompatibility and on medical applications of NiTi shape memory and superelastic alloys, Biomed. Mater. Eng. 6 (1996) 267–289.

[6] T. Duerig, A. Pelton, D. Stöckel, An overview of nitinol medical applications, Mater. Sci. Eng. A. 273 (1999) 149–160.

[7] E. Schafer, Root canal instruments for manual use: a review, Dent. Traumatol. 13 (1997) 51–64.

[8] L.E. Eiselstein, R.A. Sire, B.A. James, Review of fatigue and fracture behavior in NiTi, in: Med. Device Mater. III - Proc. Mater. Process. Med. Devices Conf. 2005, 2006: pp. 135–147.

[9] S.W. Robertson, A.R. Pelton, R.O. Ritchie, Mechanical fatigue and fracture of Nitinol, Int. Mater. Rev. 57 (2012) 1–37.
[10] S. Gollerthan, D. Herberg, A. Baruj, G. Eggeler, Compact tension testing of martensitic/pseudoplastic NiTi shape memory alloys, Mater. Sci. Eng. A. 481–482 (2008) 156–159.
[11] S. Gollerthan, M.L. Young, A. Baruj, J. Frenzel, W.W. Schmahl, G. Eggeler, Fracture mechanics and microstructure in NiTi shape memory alloys, Acta Mater. 57 (2009) 1015–1025.
[12] S. Gollerthan, M.L. Young, K. Neuking, U. Ramamurty, G. Eggeler, Direct physical evidence for the back-transformation of stress-induced martensite in the vicinity of cracks in pseudoelastic NiTi shape memory alloys, Acta Mater. 57 (2009) 5892–5897.
[13] S.W. Robertson, R.O. Ritchie, In vitro fatigue-crack growth and fracture toughness behavior of thin-walled superelastic Nitinol tube for endovascular stents: A basis for defining the effect of crack-like defects., Biomaterials. 28 (2007) 700–9.
[14] R.L. Holtz, K. Sadananda, M.A. Imam, Fatigue thresholds of Ni-Ti alloy near the shape memory transition temperature, Int. J. Fatigue. 21 (1999).
[15] A. Ahadi, Q. Sun, Grain size dependence of fracture toughness and crack-growth resistance of superelastic NiTi, Scr. Mater. 113 (2016) 171–175.
[16] J. Luo, J. He, X. Wan, T. Dong, Y. Cui, X. Xiong, Fracture properties of polycrystalline NiTi shape memory alloy, Mater. Sci. Eng. A. 653 (2016) 122–128.
[17] ASTM-E1820-15a, ASTM E1820 - 15a, Standard Test Method for Measurement of Fracture Toughness, ASTM Int. (2015).
[18] ASTM-E647-15, ASTM E647-15, Standard Test Method for Measurement of Fatigue Crack Growth Rates, ASTM Int. (2015).
[19] C. Maletta, L. Bruno, P. Corigliano, V. Crupi, E. Guglielmino, Crack-tip thermal and mechanical hysteresis in Shape Memory Alloys under fatigue loading, Mater. Sci. Eng. A. 616 (2014) 281–287.
[20] A.L. McKelvey, R.O. Ritchie, Fatigue-crack growth behavior in the superelastic and shape-memory alloy nitinol, Metall. Mater. Trans. A. 32 (2001) 731–743.
[21] R. Valiev, Nanostructuring of metals by severe plastic deformation for advanced properties., Nat. Mater. 3 (2004) 511–6.
[22] B. Kockar, I. Karaman, J.I. Kim, Y.I. Chumlyakov, J. Sharp, C.-J. (Mike) Yu, Thermomechanical cyclic response of an ultrafine-grained NiTi shape memory alloy, Acta Mater. 56 (2008) 3630–3646.
[23] R. Valiev, D. Gunderov, E. Prokofiev, V. Pushin, Y. Zhu, Nanostructuring of TiNi Alloy by SPD Processing for Advanced Properties, Mater. Trans. 49 (2008) 97–101.
[24] D. Gunderov, A. Lukyanov, E. Prokofiev, A. Churakova, V. Pushin, S. Prokoshkin, et al., Microstructure and Mechanical Properties of the SPD-Processed TiNi Alloys, in: Mater. Sci. Forum, 2013: pp. 486–490.
[25] H. Shahmir, M. Nili-Ahmadabadi, Y. Huang, J. Myun Jung, H. Seop Kim, T.G. Langdon, Shape memory effect in nanocrystalline NiTi alloy processed by high-pressure torsion, Mater. Sci. Eng. A. 626 (2015) 203–206.
[26] Y.X. Tong, F. Chen, B. Guo, B. Tian, L. Li, Y.F. Zheng, et al., Superelasticity and its stability of an ultrafine-grained Ti49.2Ni50.8 shape memory alloy processed by equal channel angular pressing, Mater. Sci. Eng. A. 587 (2013) 61–64.
[27] ASTM-E399-12e3, ASTM E399-12e3, Standard Test Method for Linear-Elastic Plane-Strain Fracture Toughness KIc of Metallic Materials, ASTM Int. (2012).
[28] S. Suresh, Fatigue of Materials, Cambridge University Press, 1991.

[29] A. Hohenwarter, R. Pippan, A comprehensive study on the damage tolerance of ultrafine-grained copper, Mater. Sci. Eng. A. 540 (2012) 89–96.
[30] C.F. Shih, Relationships between the J-integral and the crack opening displacement for stationary and extending cracks, J. Mech. Phys. Solids. 29 (1981) 305–326.
[31] T. Leitner, A. Hohenwarter, R. Pippan, Revisiting fatigue crack growth in various grain size regimes of Ni, Mater. Sci. Eng. A. 646 (2015) 294–305.
[32] A. Hohenwarter, R. Pippan, Fracture toughness evaluation of ultrafine-grained nickel, Scr. Mater. 64 (2011) 982–985.
[33] R. Pippan, L. Plochl, F. Klanner, H.P. Stuwe, Use of fatigue specimens precracked in compression for measuring threshold values and crack growth, J. Test. Eval. 22 (1994) 98–103.
[34] W.C. Oliver, G.M. Pharr, J.B. Pethicai, R. Hutchings, W.C. Oliver, J.B. Pethica, et al., An improved technique for determining hardness and elastic modulus using load and displacement sensing indentation experiments, J. Mater. Res. 7 (1992) 1564–1583.
[35] A. Latapie, D. Farkas, Molecular dynamics investigation of the fracture behavior of nanocrystalline α -Fe, Phys. Rev. B. 69 (2004) 134110.
[36] D. Farkas, B. Hyde, Improving the ductility of nanocrystalline bcc metals, Nano Lett. 5 (2005) 2403–2407.
[37] A. Hohenwarter, R. Pippan, Anisotropic fracture behavior of ultrafine-grained iron, Mater. Sci. Eng. A. 527 (2010) 2649–2656.
[38] A. Hohenwarter, R. Pippan, Fracture of ECAP-deformed iron and the role of extrinsic toughening mechanisms., Acta Mater. 61 (2013) 2973–2983.
[39] R.O. Ritchie, Mechanisms of fatigue crack propagation in metals, ceramics and composites: Role of crack tip shielding, Mater. Sci. Eng. A. 103 (1988) 15–28.
[40] R. Pippan, Dislocation emission and fatigue crack growth threshold, Acta Metall. Mater. 39 (1991) 255–262.
[41] G.R. Irwin, Plastic zone near a crack and fracture toughness, Proc. Seventh Sagamore Ordnance Mater. Res. Conf. (1960) IV-63.
[42] C. Laird, G.C. Smith, Crack propagation in high stress fatigue, Philos. Mag. 7 (1962) 847–857.
[43] C. Laird, The Influence of Metallurgical Structure on the Mechanisms of Fatigue Crack Propagation, Fatigue Crack Propagation, ASTM STP 415. (1967) 131.
[44] P. Neumann, Coarse slip model of fatigue, Acta Metall. 17 (1969) 1219–1225.
[45] F.O. Riemelmoser, R. Pippan, Mechanical reasons for plasticity-induced crack closure under plane strain conditions, Fatigue Fract. Eng. Mater. Struct. 21 (1998) 1425–1433.